Reduced-Order Electro-Thermal Models for Computationally Efficient Thermal Analysis of Power Electronics Modules

By

Xiaojun Dong

A thesis submitted in partial fulfilment of the requirements of the degree of Doctor of Philosophy
The University of Sheffield
Faculty of Engineering
Department of Electronic & Electrical Engineering
August 2020

Acknowledgements

First of all, I would like to express my sincere gratitude to my supervisor, Dr. Antonio Griffo, for his guidance, patience, knowledge and continuous support during my Ph.D research. I am extremely grateful for his guidance in the writing of my papers and thesis. I am honoured to be his Ph.D student.

I want to thank Prof. Jiabin Wang and Dr. Guang-Jin Li for their knowledge and comments. My sincere thanks also goes to Dr. David Hewitt for his help in my experiments.

Last but not least, I want to thank my mother, my father and my wife. Without their support and help, I can never pursue my dream.

Contents

Abstract

Silicon and Silicon Carbide-based power module are common in power electronic systems used in a wide range of applications, including renewable energy, industrial drives and transportation. Reliability of power electronics converters is very important in many applications.

It is well known that reliability and ultimately the lifetime of power modules is affected by the running temperature during power cycles. Although accurate thermal models of power electronics assemblies are widely available, based e.g. on computational fluid dynamics (CFD) solvers, their computational complexity hinders the application in real-time temperature monitoring applications.

In the thesis, geometry-based numerical thermal models and compact thermal models will be developed to address the fast thermal simulation in the electronic design process and real-time temperature monitoring, respectively.

Accurate geometry-based mathematical models for dynamic thermal analyses can be established with the help of finite difference methods (FDM). However, the computational complexity result from the fine mesh and large dimension of ordinary differential equations (ODE) system matrix makes a drawback on the analysis in parametric studies. In this thesis, a novel multi-parameter order reduction technique is proposed, which can significantly improve the simulation efficiency without having a significant impact on the prediction accuracy. Based on the block Arnoldi method, this method is illustrated by referring to the multi-chip power module connected with air-force cooling system including plate-fin heatsink.

In real-time temperature monitoring, more compact tools might be preferable, especially if operating and boundary conditions such as losses and cooling are now known accurately, as it’s often the case in practical applications. Compared with geometry-based model which is more suitable in the design of power modules, lumped parameter thermal compact model is simpler and can be applied in real-time temperature prediction during the power cycles of power modules. This thesis proposes a reduced order state space observer to minimize the error caused by air temperature and air flow rate. Additionally, a novel feedback mechanism for disturbance estimation is introduced to compensate the effect result from the error of input power loss, air flow and changes of other nonlinearities.

Nomenclatures

N_f	The possible number of power cycles $[R]$
ΔT_j	The increase of the cycling temperature amplitude [°C]
q	The local heat flux density $[W/m^2]$
k	The thermal conductivity $[W/(m\cdot K)]$
∇T	The temperature gradient $[K/m]$
q_x	The heat transferred in the solid $[W]$
$\partial T/\partial x$	The temperature gradient in x-direction $[K/m]$
A	The area of heat conduction $[m^2]$
$\dot{q}$	The internal heat energy per unit volume $[W/m^3]$
c_p	Specific heat capacity $[J/(K\cdot kg)]$
ρ	Density $[kg/m^3]$
q_{x+dx}	The heat transferred out the solid $[W]$
u_m	The mean flow velocity $[m/s]$
d	The diameter of flow $[m]$
v	Kinematic viscosity $[m^2/s]$
μ	The dynamic viscosity $[kg/(m\cdot s)]$
q_{flow}	Transferred heat of the flow $[W]$
h	Convective heat transfer coefficient $[W/(m^2K)]$
A_h	Heat transfer surface area $[m^2]$
T_w	Temperature of the solid surface [°C]
T_∞	Temperature of the fluid sufficiently far from the surface [°C]
P_{loss}	The power losses of power modules [W]
T_{chip}	Semiconductor temperature [°C]
$T_{heatsink}$	Heatsink temperature [°C]
ΔT	Temperature difference [°C].
Z_{th}	Thermal impedance $[k/W]$
R_{th}	Thermal resistance $[k/W]$
l	Material thickness $[m]$
k_{th}	Heat conductivity $[W/(m\cdot K)]$
A_{th}	Heat flow area $[m^2]$
C_{th}	Thermal impedance $[J/K]$

V	Volume [m^3]
$T(\vec{x},t)$	The temperature of the coordinate $\vec{x}(t)$ at the time t [°C]
$\dot{q}(\vec{x},t)$	The internal heat energy per unit volume [W/m^3]
$q_{loss}(\vec{x},t)$	The power loss of the coordinate $\vec{x}(t)$ at the time t [W]
L	Heat sink length [m]
L_{fin}	Height of fins [m]
L_{base}	Baseplate thickness [m]
b	Heat sink channel spacing [m]
t	Heat sink fin thickness [m]
A_{hs}	Heat sink base plate area [m^2]
$\dot{m}$	Mass flow rate of air [kg/s]
T_{in}	Inlet air temperature [°C]
T_{base}	Baseplate temperature [°C]
n	Number of channels [R]
$R_{th,d}$	Thermal resistance of base plate [K/W]
$R_{th,fin}$	Thermal resistance of fin [K/W]
$R_{th,A}$	Thermal resistance of fin to air [K/W]
$R_{th,a}$	Thermal resistance of base plate to air [K/W]
T_{air}	Temperature of air in the heat sink channel [°C]
k_{hs}	The thermal conductivity of heat sink material [$W/(m \cdot K)$].
$T_{air,in}$	Inlet air temperature of heatsink [°C].
$T_{air,ave}$	Average air temperature in the middle of heatsink [°C].
$T_{air,out}$	Output air temperature of heatsink [°C].
R_h	The convective thermal resistance [K/W]
R_{fluid}	The fluid resistance [K/W]
$T_{air,in}$	Inlet air temperature of heatsink [°C]
$T_{air,ave}$	Average air temperature in the middle of heatsink [°C]
$T_{air,out}$	Output air temperature of heatsink [°C]
A_{eff}	Effective heat transfer surface area [m^2]
$\dot{m}$	Mass flow rate [kg/s]
c_{air}	Specific heat capacity of air 1.01e^3 [$J/(kg \cdot K)$]
η	Fin efficiency [R]

$N_{u\mathcal{L}}$	Nusselt number $[R]$
k_{fluid}	The thermal conductivity of the fluid $[W/(m \cdot K)]$
$\mathcal{L}$	The characteristic length $[m]$
A	The area of air flow $[m^2]$
P_{flow}	The perimeter of air flow $[m]$
L	Duct length of heatsinks $[m]$
L^+	Dimensionless duct length $[R]$
z	Axial coordinate of heatsink ducts $[m]$.
z^*	Dimensionless axial coordinate of heatsink ducts $[R]$
$Re_{\sqrt{A}}$	Reynolds number based on $\mathcal{L} = \sqrt{A}$ $[R]$
μ	The dynamic viscosity of air $[kg/(m \cdot s)]$
L^*	Dimensionless thermal length $[R]$
z^*	Dimensionless position for thermally developing flow of heatsink ducts $[R]$
$Pe_{\sqrt{A}}$	Peclet number based on $\mathcal{L} = \sqrt{A}$ $[R]$
w_{ave}	Average velocity of air flow $[m/s]$
α	Thermal diffusivity $[m^2/s]$.
Pr	Prandtl number (air $\approx$ 0.71) $[R]$
ϵ	The nominal aspect ratio of heatsink $[R]$
v	Kinematic viscosity ($2 \times 10^{-5} m^2/s$ for air).
c_{air}	Thermal capacitance of air $1.01e^3$ $[J/(kg\ \cdot\ K)]$
k_{air}	The thermal conductivity of the air 0.03 $[W/(m \cdot K)]$
d_h	Hydraulic diameter of the heat sink channel $[m]$.
A_{eff}	Effective heat transfer surface area $[m^2]$
b_{hs}	The width of heatsink base plate $[m]$
A_{base}	The area of heatsink base plate $[m^2]$.
b_{hs}	The width of heatsink base plate $[m]$.
h_{equ}	Equivalent heat transfer coefficient $[W/(m^2K)]$

Chapter 1 Introduction

1.1 Motivation

Advances in modern power electronics have resulted in fast paced expansion in the areas of generation, transmission, distribution, and end-user consumption of electrical power [1]. In these new systems, the reliability of the power electronics is a challenge [2-4], especially in applications with strong safety requirements (e.g. aerospace and automotive) or where continuous operation is required to avoid costly maintenance (e.g. renewable energy). These applications provide specific challenges concerning reliability due to the requirement that they operate continuously for long periods of time in harsh environment without user intervention [5].

Health management and reliability constitute a fundamental part of the design and development cycle of electronic products [6] [7]. To ensure reliability, the failure mechanism of power electronic modules has become an essential part of the electronic design process. The failure mechanism of power electronics is complicated, which is generally affected by several factors. Among the failure mechanisms shown in [8-10], thermal cycling (i.e., temperature fluctuations inside or outside the component) is one of the most critical causes of failure in power electronic systems [11-14].

The thermal cycle amplitude is the most important factor affecting the aging rate of power modules [15], and thermo-mechanical failure modes in the equipment and package is accelerated by the temperature cycle. Models of the fatigue phenomena were obtained via power cycling experiments, e.g., in [16-20]. It has been demonstrated in many studies that the module lifetime, measured by the number of possible temperature cycles N_f, is reduced exponentially with an increase of the cycling amplitude ΔT_j. This effect can be observed in Figure 1.1 [21].

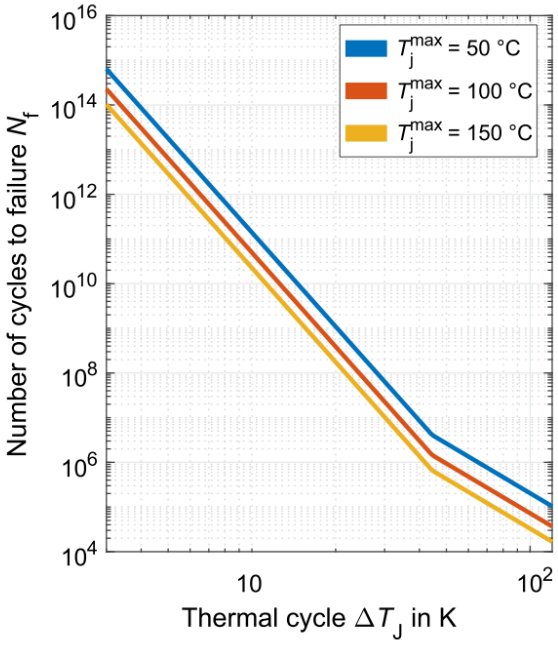

Figure 1.1. Empirical power cycling data of the Hybridpack2 (HP2) [21].

Consequently, thermal management of power converters has become an essential part of the converter design process [22-26]. This interest in thermal management has been further driven by the strong desire for higher power density [27] [28], increased efficiency power electronics systems. Accurate knowledge of power device die temperature is critical to the implementation of control and health management algorithms which have been proposed to monitor and extend the lifetime of power modules under in-service conditions [29].

1.2 Aims and Objectives

In the thesis, geometry-based numerical thermal models and compact thermal models will be developed to address the fast thermal simulation in the electronic design process and real-time temperature monitoring, respectively. To perform the analysis of thermal model, a range of design variables and operating conditions, such as inlet air temperature, velocity of the air flow, material composition of the power modules, and the geometry of the assembly, must be considered.

The research challenges and questions in relation to the thermal analysis of integrated power electronics system design to be addressed are as follows:

For optimised thermal design of power devices:

1. How to deal with challenges for the thermal analysis of complex and large-scale systems?
2. How should the thermal model be applied for accurate system-level integrated power electronic design?
3. How to reduce the computational complexity caused by the simulation of complex distributed dynamic systems?
4. How to avoid repeating the simulation process for each variation in design parameters, especially the design parameters of the cooling system, e.g., the coolant mass flow rate?

For real-time temperature monitoring of power devices:

1. How to obtain computationally efficient thermal models suitable for running in a real-time environment for online thermal monitoring?
2. How to take into account the nonlinearities in the thermal model for real-time temperature monitoring?

The goal of this research is thus to support optimised thermal design and real-time thermal monitoring of power devices. The following work will be demonstrated.

Plan of work

- Analysis to support optimised thermal design of power devices

1. Develop numerical methods for power electric system with complicated geometry structure and air-force cooling system based on finite-difference methods (FDM).

2. Develop a numerical model for forced-air cooling system.
3. Validation of numerical model for the designed forced-air cooling system against computational fluid dynamics (CFD) model.
4. Develop a novel method for parametric model order reduction (MOR) that preserves design parameters representing different cooling systems and boundary conditions, e.g. convection heat transfer coefficients.
5. Validation of developed multi-parametric model order reduction against simulation of CFD models.
6. Experimental validation of novel multi-parametric model order reduction methods using parameters generated from the numerical model for the designed cooling system.

- Analysis to support real-time temperature monitoring of power devices

1. Develop methods for the extraction of parameters for lumped parameter heat transfer analysis.
2. Develop a state-space thermal model based on the estimated parameters and validate against CFD results.
3. Develop a reduced-order thermal observer.
4. Develop novel methods for the disturbance estimations of input power loss, air flow and changes of other non-linear components.
5. Validations of developed reduced-order observer model with disturbance estimations against experiment including a relatively complex three-phase converter setup which is fully representative of real industrial applications.

1.3 Contributions

All the objects listed in Section 1.2 have been met and described in the thesis. Novel aspects and contribution to knowledge in this work are outlined below:

1. Novel algorithm for multi-parametric model order reduction algorithm for the system-level design of power devices

The developed model order reduction techniques provide a valuable methodology for the analysis of complex and large-scale systems. The methodology illustrated in the thesis can be easily generalised to more complex and/or larger systems. Typically, the dimension of a thermal problem discretized with finite difference can be extremely large, therefore rendering it intractable for large scale system if a fine discretization is required. In this case, MOR techniques and in particular the proposed MOR will provide a tool for parametric analyses to support optimised design.

Optimization of layout in power electronics modules and converters design might require many iterations using different values of parameters e.g. of materials or cooling conditions. With the proposed parametric MOR such applications can be greatly simplified as the reduced order model conserves dependency on parameters which can be simply modified at each iteration without requiring additional computations.

2. Wide-range applications of developed numerical thermal model with multi-parametric model order reduction

The method can have applications at both the design stage and during operation of power conversion systems. Thanks to its low computational complexity, the resulting reduced order model can also be used in real-time applications as an observer for temperature estimation of power devices during converter operation.

The laboratory scale demonstration presented in the thesis is not a particularly large system, nevertheless it presents all the feature and modelling complexities of typical air cooled three-phase converters systems and therefore provides an industrially relevant example of application.

3. Novel reduced-order observer model with disturbance estimation

In general, thermal modelling of a physical system, is not unique. Many variants of thermal networks can be used to approximate the thermal response of the system, using e.g. the well-known Cauer or Foster networks. In this work, third and first order networks are used to represent the vertical heat transfer between the power devices and the ambient, respectively. The order of the networks is a compromise between the ability to model multiple time constants (the higher the order of the network, the more time constants can be modelled) and simplicity of implementation in a real-time monitoring system.

The modelling using lumped parameter RC networks in the derivation of the reduced-order thermal observer. It should be highlighted here that the main contribution is not the use of a reduced-order observer, which is well known in literature, but the inclusion of an additional feedback mechanism in the observer, the disturbance estimation, which provides a method to compensate for uncertainties in parameters and/or boundary conditions.

4. Novel feedback mechanism to compensate the errors of the dynamic thermal system in the real-time application

The modelling dynamic performances might be affected by both errors in the input values (e.g. estimation of power loss and/or air-cooling boundary conditions) and uncertainties in the parameters of the state-space system. Uncertainties due to unknown coolant flow rate, parameters and power losses might also be difficult to address. Novel feedback mechanism of the disturbance observer provides a feedback mechanism to compensate the effects of all the errors combined instead of an accurate separation of the multiple sources of errors.

This additional feedback mechanism, implemented in a reduced-order observer, uses the temperature measurement of the inlet air and of a thermistor mounted on the power module substrate. It is also worth noting that the air temperature is a much simpler value to measure than the power dissipation, making it a more suitable input for the disturbance observer.

1.4 Structure of the Thesis

Chapter 1 presents the introduction and motivation of the thesis, where a detailed background, motivation, objectives and contributions of the thesis are also included.

Chapter 2 presents an overview of thermal analysis methods for power electronics. The literature review starts from the introduction of integrated power electronics system, including material composition of the power modules, and the geometry of the assembly. After the review of the design variables in integrated power electronics system, a vast literature thermal analysis is introduced for the accurate temperature estimations of power modules. Geometry-based numerical thermal tools and compact thermal models will be presented the review. Finally, model order reduction techniques and closed-loop estimation methods are reviewed for improving the computational efficiency and accuracy of geometry-based numerical thermal tools and compact thermal models respectively.

Chapter 3 includes three main contributions. Geometry-based numerical conductive thermal modelling, numerical modelling of convective heat transfer and lumped parameter compact thermal model with parameter estimation, are developed. With the help of geometry-based numerical conductive thermal modelling, 3D dynamic finite difference thermal model of power modules can be obtained. Due to the fact that power modules are generally mounted on heatsink for cooling, convective heat transfer analysis will be developed to compensate 3D conductive thermal model for a complete power electronic systems, including power modules and cooling system. To achieve this, a review of the cooling system behaviour must be available and a range of design variables, such as fluid temperature, fluid velocity and pressure drop, will be considered.

These results do not constitute the main novelty of the thesis but are essential in the derivation of the multi-parametric model order reduction and compact thermal modelling with reduced-order observer and disturbance estimation. The computational complexity of the obtained 3D dynamic finite difference thermal model will be reduced using model order reduction techniques in Chapter 4. Additionally, the design parameters conserved in multi-parametric order reduction technique are the convective heat transfer coefficients obtained from numerical modelling of convective heat transfer. Finally, the RC parameters estimated by the developed compact thermal model will be used in the observer design in Chapter 5.

A number of different geometries are used in the derivation of the models, starting from a simplified rectangular N-layer geometry with an arbitrary numbers of heat sources. The topology of power modules can be closely approximated by this type of structure. Validations of different model order reduction techniques against detailed simulation in ANSYS will be demonstrated in Chapter 4 based on this topology. The detailed topology of Silicon Carbide (SiC) MOSFET-based half-bridge designed and manufactured by Siemens AG will be used in numerical modelling of convective heat transfer analysis and lumped parameter compact thermal model with parameter estimation.

In Chapter 4, a novel multi-parametric order reduction technique is derived and applied to power modules. Conventional methods for order reduction are also summarised to help the derivation of multi-parametric order reduction algorithm. The works in this chapter is demonstrated against two case studies:

Initially, the simplified geometry of power module of Chapter 3 for the geometry-based numerical conductive thermal modelling is applied. Validations of multi-parametric model order reduction against full-order numerical thermal modelling, conventional model order reduction and commercial software ANSYS Mechanical are established, confirming the efficiency and accuracy of the novel type multi-parametric order reduction technique. A further application is provided to a forced-air cooling system and Silicon Carbide (SiC) MOSFET-based half-bridge with DC power supply, which is representative of real industrial applications. In this validation, DC currents are used as source of power losses. These can be easily measured, reducing the uncertainties. Validation with time-varying losses and transient air flow rate is also presented, demonstrating good data agreement, transient accuracy and robustness.

In Chapter 5, a novel reduced-order observer model with disturbance estimation is derived. Compared with 3-D model, lumped parameter compact thermal modelling is simpler and can be applied in temperature prediction during real-time operation of a power converter. This chapter proposes a reduced order state space observer to minimize the error caused by air temperature and air flow rate. Additionally, disturbance estimation is introduced to compensate the effect result from the error of the power loss estimation. The experimental validations include applications to the forced-air cooling of the SiC module in DC and AC conditions, fully representative of real industrial applications.

In Chapter 6, the conclusions and contributions of the thesis as well as potential suggestions for future work are provided.

1.5 List of Publications

Journal:

X. Dong, A. Griffo and J. Wang, "Fast simulation of transient temperature distributions in power modules using multi-parameter model reduction," in *The Journal of Engineering*, vol. 2019, no. 17, pp. 3603-3608, 2019.

X. Dong, A. Griffo, D. A. Hewitt and J. B. Wang, "Reduced-Order Thermal Observer for Power Modules Temperature Estimation," in *IEEE Transactions on Industrial Electronics*, 1–1. doi:10.1109/tie.2019.2959483, 2019.

X. Dong, A. Griffo and J. Wang, "Multi-Parameter Model Order Reduction for Thermal Modelling of Power Electronics," in *IEEE Transactions on Power Electronics*, 1–1. doi:10.1109/tpel.2020.2965248, 2020.

Chapter 2 Literature Review

2.1 Introduction

It is well known that the ability to dissipate the heat generated in a power converter is often the most crucial constraint in the design of a power converter. Due to the increased demands for power density, thermal issues are becoming ever more prominent, resulting in a reduction to the effectiveness of heat dissipation paths and an increase in cross-coupling (mutual heating) between neighbouring devices. Therefore, efficient computational methodologies for accurate thermal modelling, are required to tackle these problems in the initial design process.

This chapter introduces some of the issues related to the thermal performance and thermal modelling of power electronic systems. Thermal modelling can not only support optimised design of power electronics systems, but also be applied in real-time applications of power devices, where continuous estimation of the internal temperature of electronic devices is often needed to improve systems reliability. More accurate estimation of the temperature swing of junction temperature will lead to a more accurate determination of power electronic module lifetime and ultimate reliability of the power semiconductor modules [30].

An overview of the common methodologies for thermal modelling applied to power electronics converter is presented. The computational complexity of detailed modelling is illustrated and the literature on methodologies for model order reduction is presented and reviewed. Methodologies for real-time observation of temperature in power electronics systems are also reviewed.

2.2 Power Electronics System

Power electronics systems have found widespread applications in all areas where there is a need for conversion of electrical energy from one voltage and/or frequency level to another. Power semiconductor devices are at the core of each power electronics system. The power semiconductor switches are usually mounted in appropriate packaging and/or assembled into power modules. The basic components and the technical challenge of power electronic systems will be introduced in this section.

2.2.1 Power Semiconductors

Power semiconductor devices are used in power converters to provide a practical approximation of an ideal switch. The most common power semiconductor devices are power diodes, thyristors, power IGBTs as well as MOSFETs [31] [32].

IGBTs and MOSFETs have many advantages, in term of switching speed, efficiency and cost in low/medium voltage applications and therefore are the most commonly used in low-medium power applications, e.g. sub 1MW [33]. The vast majority of power semiconductor switches (IGBTs, MOSFETs) in use to date are based on Si substrates thanks to availability, optimization of manufacturing processes, high volume productions, low cost and reliability.

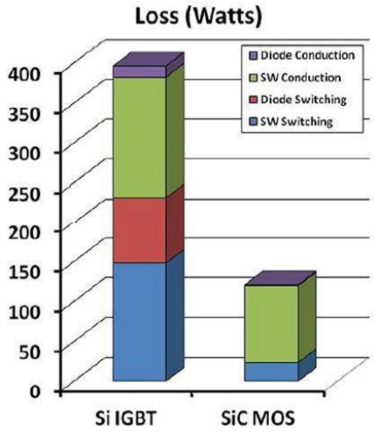

Figure 2.1 Loss comparison between traditional silicon IGBT and SiC-based power MOSFET [31]

However, more recently, SiC-based devices are gradually being introduced in more demanding applications where high efficiency is needed, thanks to superior characteristics usually in terms of increased switching speed and reduced switching losses. A comparison is given in Figure 2.1 between a traditional silicon IGBT and SiC-based power MOSFET with similar rating, proving the reduction in power losses [31]. It is evident that SiC-based power MOSFET has lower power consumption compared with IGBT.

2.2.2 Power Electronics System Packaging and Power Modules

Power electronics packing is an important issue in power electronics systems. Packaging is essential to provide mechanical support and electrical access to the semiconductor devices. The packaging technology has significant implications in terms of system reliability and thermal performance.

Typically, power modules consist of a multi-layer structure with heterogeneous materials including semiconductor chips, power electronic substrate, copper baseplates and solders, etc. The structure of a classical power module can be seen in Figure 2.2 [34].

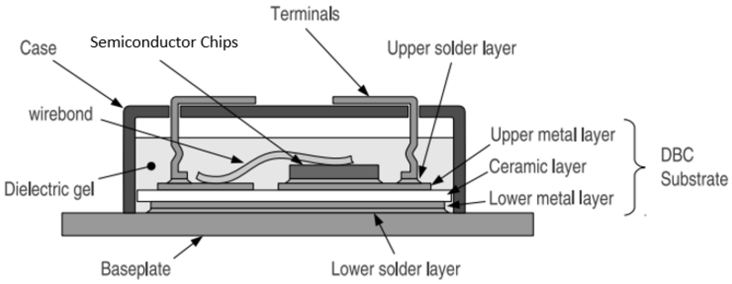

Figure 2.2 Structure (cross-section) of a classical power module [34].

The semiconductor chips are usually connected with the power electronic substrates via solder materials, carrying the power semiconductors, providing thermal and electrical contact as well as electrical insulation when needed. The main power electronic substrate is the direct bonded copper (DBC) substrate. DBC substrates have been widely used in power electronic modules because of their excellent thermal conductivity. The copper plates of DBC substrates are bonded to one or both sides through an oxidation process with high temperature.

Semiconductor devices terminal are typically metallized and their connection to the package is usually obtained by soldering or diffusion sintering technology. Soldering is the connection of two (metal) materials by liquid metal or a liquid alloy. Diffusion sintering is a process which does not use a solder material but typically requires heat and/or pressure. In terms of the long-term reliability, diffusion sintering technology may be considered as being far superior to soldering. Compared with solder, sintered layers display better thermal, mechanical and electrical properties [35].

Wire bonding is often used to connect a power semiconductor chip terminals with other chips or connecting elements.

High power modules are typically mounted on baseplates to provide mechanical robustness during transport and assembly. Baseplate can also contribute to a larger thermal mass and lower thermal impedance.

The materials used in power electronic packaging are listed as follows:

- Semiconductor chips: Most of the devices are Si-based, although other semiconductor chips have also been used like SiC, GaN, etc [36].
- Substrate: General ceramic substrates material used in DBC are alumina, aluminium nitride and beryllium oxide [37]. Alumina is widely applied due to its low cost.
- Baseplate: Common baseplates are made in copper.
- Die-attached: Die-attaching materials fall into many categories, spanning both high and low temperature use. Two of the most commonly used die-attach materials today are solder alloys and conductive epoxy [38].
- Wire bond: The widely used materials are aluminium and copper.
- Case: Silicone gels are widely retained for encapsulating high voltage and high temperature (lower than 250 °C) [39] multi-chip power assemblies, due to their high softness and high insulating electrical properties.

2.2.3 Challenges in Reliability of Power Electronics System

In many industrial applications, there is an increased demand for higher reliability requirements of power electronics system. However, many challenges to reliability are present due to the following factors [40]:

- More demanding mission profiles.
- Harsh environments.
- The complexity of electronic systems is increased in terms of functionality, number of components, and control algorithms.
- Resource limitations (e.g. time, cost) for reliability testing and robustness validation due to time-to-market pressures and financial stress.
- More stringent cost constraints, reliability requirements and security compliance of power systems.
- Higher power densities are continually required in more advanced integration of power converters and power electronics systems, which can lead to new failure mechanisms and thermal issues.
- Uncertain reliability of new materials and packaging technologies (e.g. SiC and GaN devices).

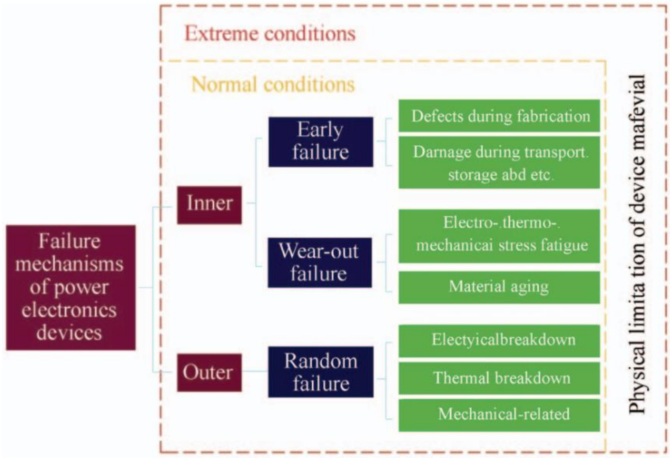

Figure 2.3 Failure mechanisms of power electronics devices [41].

The failure mechanisms of power electronics are complicated and are affected by many factors. These factors can be classified into inner factors and outer factors [41] as shown in Figure 2.3. Inner factors of power electronic devices failures consists of early and wear-our failures [41]. Defects are mainly caused by the fabrication process and packing process.

Fatigue and aging is mainly caused by device material characteristics under certain stresses. According to the failure sources, the fatigue and aging mechanisms of power devices can be divided into chip-related and package-related failures [41]. The chip-related failures mainly comes from the interface fatigue based on the physical structure of the device and the Si fatigue as shown in Figure 2.4 [42]. The package-related failures comes from the solder fatigue and the bonding wire fatigue as shown in Figure 2.5 [42].

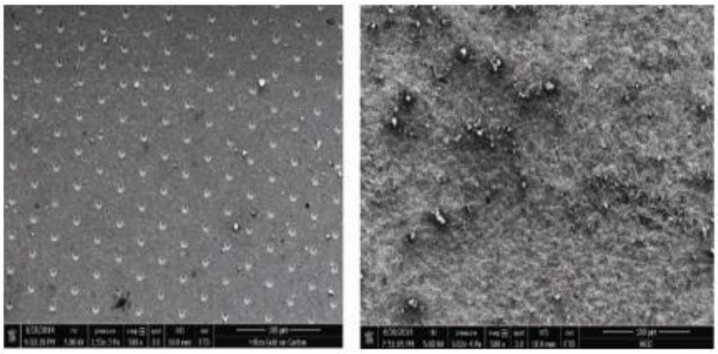

Figure 2.4 Photo of device surface before and after fatigue [42].

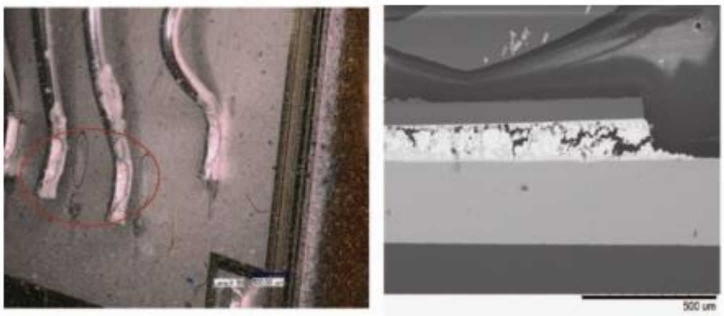

Figure 2.5 Bonding wire lift-off and solder fracture after fatigue [42].

Outer factors of power devices failure can be classified into electrical breakdown, mechanical-related failure and thermal breakdown [41]. M. Ishiko [42] found that the electrical breakdown is mainly caused by avalanche breakdown. Mechanical-related failure is an important factor especially for press pack modules because it induces unequal thermal resistance distribution to the module package, leading to high local temperature and finally causing device burnout of operation current is large. Thermal breakdown result from the large energy by large current, will contributes to the local or partial burnouts [43]. It results in failure mechanisms at material interfaces within the power module, e.g., at solder, chip and bond wire, as shown in Figure 2.6 to 2.8 [43].

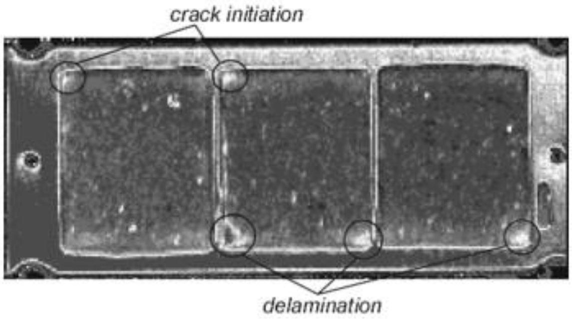

Figure 2.6 Solder degradation after power cycling [43].

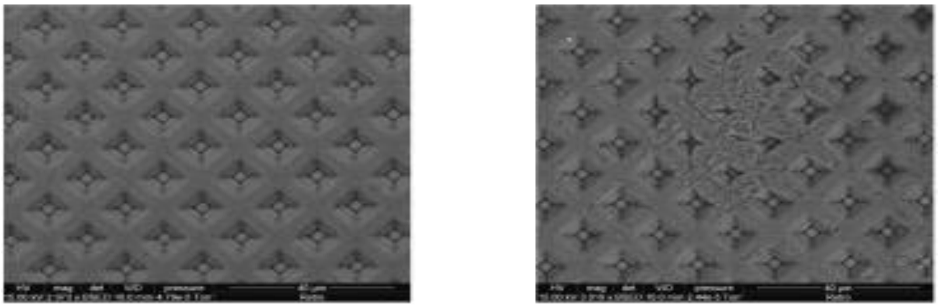

(a) Before power cycling (b) After power cycling

Figure 2.7 Chip metallization degradation before and after power cycling [43]

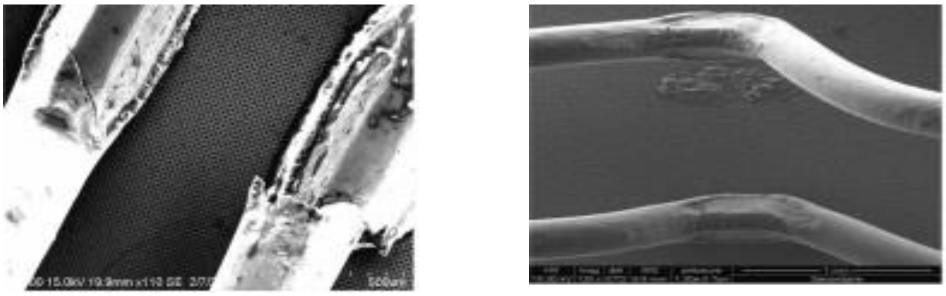

(a) Fracture of bond wire (b) Liftoff of bond wire

Figure 2.8 Examples of bonding damages after power cycling [43]

Among the failure mechanisms listed above, it has been revealed that thermal breakdown caused by the thermal cycling (i.e., temperature swings inside or outside the components) is one of the most critical failure causes in power electronics system [44]. The temperature fluctuation of different materials with mismatched coefficients of thermal expansion may cause a disconnection in the contacting areas after a certain number of cycles, thus leading to the wear-out of the devices.

2.2.4 Thermal Monitoring of Power Electronics System

Temperature sensors are widely used in power modules for thermal measurement of power electronic systems. The most common temperature sensors used in power modules are negative temperature coefficient (NTC) thermistor with resistance that decreases while temperature increases [45].

As is shown in Figure 2.9, the NTC thermistor is typically located close to the power semiconductor chips, on the same ceramic substrate.

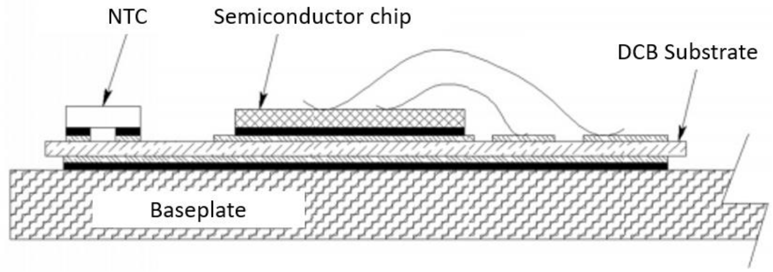

Figure 2.9 Location of on the substrate [45].

The NTC thermistor is helpful in the protection of a power electronics system from overheating or cooling system failures. Compared with thermocouples, NTC thermistors have more sensitive response. However, a NTC thermistor is often associated with a long time constant to detect a change in temperature in a module. Due to its slow response, the NTC thermistor is not suited to detect rapid changes in temperature [45]. Additionally, the thermistor only measure the substrate temperature and not the device junction temperature.

2.3 Heat Transfer Analysis

Since temperature plays a significant role in the reliability of power modules, mathematical models for heat transfer analysis in power modules have been extensively studied. In this section, an overview of the heat transfer mechanisms and the main methods for numerical analyses of heat transfer problems are briefly presented.

Heat caused by power losses inside a power module need to be dissipated to the ambient through a cooling medium, typically air or a liquid. It is well known that the mechanisms for heat transfer are: conduction in solids, convection of fluids (liquids or gases), and radiation through any medium transparent to electromagnetic radiation. Radiation can often be ignored as heat transfer will be dominated by conduction in the solid body of the module and by convection at the interface with the cooling fluid [46].

2.3.1 Conductive Heat Transfer

Thermal conduction occurs in the solids due to temperature difference between the parts of the solid [47]. Conduction is a form of heat transfer that exists due to direct contact between materials without movement. A temperature gradient within a substance causes a flow of energy from a hotter to colder region [48].

Conduction is governed by Fourier’s Law, which states that the energy flux is proportional to the temperature gradient as follows

$$q = -k\nabla T \tag{2.3.1}$$

Where

- q : The local heat flux density $[W/m^2]$.
- k : The thermal conductivity $[W/(m \cdot K)]$.
- ∇T: The temperature gradient $[K/m]$.

For many simple applications, Fourier's law is used in its one-dimensional form, as shown in Figure 2.10.

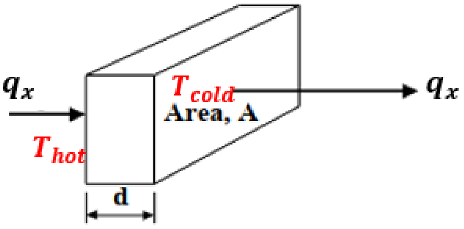

Figure 2.10 One-dimensional conductive heat transfer [47].

Figure 2.10 has shown that there is a heat transfer from the region with higher-temperature to the lower-temperature region. By Fourier's law for an isotropic medium, the heat transfer rate per unit area is proportional to the negative temperature gradient across it. In the x-direction

$$\frac{q_x}{A} = -k\nabla T = -k\frac{\partial T}{\partial x} \tag{2.3.2}$$

Where

- q_x: The heat transferred in the solid $[W]$.
- $\partial T/\partial x$: The temperature gradient in x-direction $[K/m]$.
- A: The area of heat conduction $[m^2]$.

If the temperature of the solid is time-varied, or if there is inner heat generation within the solid as shown in Figure 2.11, the situation of heat conduction is more complex.

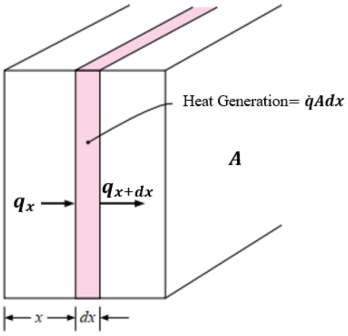

Figure 2.11 One-dimensional time-varied heat conduction analysis [47].

Assuming the temperature is changing with time and heat source is present with in the solid, the sum value of transferred heat q_x and inner heat generation should be equal to the sum of change in internal energy and conducted energy, as expressed in the follows.

$$q_x + \dot{q}Adx = c_p\rho A\frac{\partial T}{\partial t}dx + q_{x+dx} \tag{2.3.3}$$

Where

- $\dot{q}$: The internal heat energy per unit volume $[W/m^3]$.
- c_p: Specific heat capacity $[J/(K \cdot kg)]$.
- ρ: Density $[kg/m^3]$.
- $\dot{q}Adx$: The inner heat generation of the solid $[W]$.
- $c_p \rho A \frac{\partial T}{\partial t} dx$: The change in internal energy of the solid $[W]$.
- q_{x+dx}: The heat transferred out the solid $[W]$.

In equation (2.3.3), the q_{x+dx} can be expressed as

$$q_{x+dx} = -kA \frac{\partial T}{\partial x}\bigg]_{x+dx} = -A\left[k\frac{\partial T}{\partial x} + \frac{\partial}{\partial x}\left(k\frac{\partial T}{\partial x}\right)dx\right] \tag{2.3.4}$$

Combing Equation (2.3.2) to (2.3.4), the heat transfer equation can be given with $\alpha = k/(c_p\rho)$ as

$$\frac{\dot{q}}{k} + \frac{\partial^2 T}{\partial x^2} = \frac{1}{\alpha}\frac{\partial T}{\partial t} \tag{2.3.5}$$

2.3.2 Convective Heat Transfer

The process of heat transfer between a surface and a fluid flowing in contact with it is called convective heat transfer. Conduction and convection are similar, as both mechanisms require the presence of material media. The difference between the two heat transfer mechanisms is that convection requires the presence of fluid motion over a moving continuous solid surface [47].

Convection can be classified into natural convection and forced convection, according to how the fluid motion is initiated [47]. Natural convection occurs naturally and natural convection is due to density changes caused by concentration difference or temperature difference. The temperature gradient in the fluid will cause the change of density gradient. If the low density fluid is located lower side while the high density fluid is located upper side, then the natural convection will be formed under the action of gravity. Forced convection is convection caused by the push of external forces. Increasing the flow speed of liquids or gases can speed up the spread of heat [47].

Generally, when a fluid flows on a flat plate, the fluid contacting the surface stays closer to the wall due to shear stress. The region where the flow is adjusted from the zero velocity at the wall to the maximum in the main flow is called the boundary layer [49].

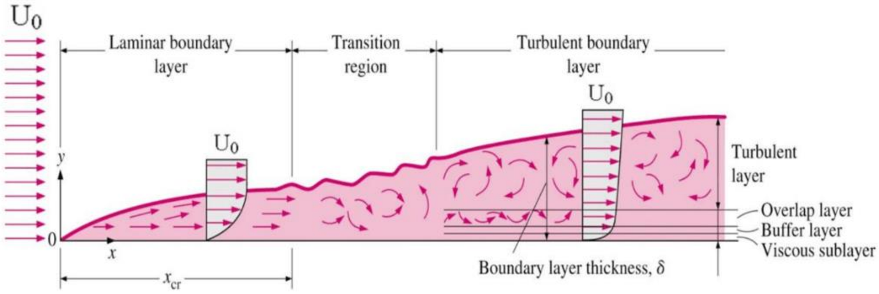

Figure 2.12 Dynamic flow on flat plate [49].

As shown in Figure 2.12 [49], boundary layers may be either laminar, or turbulent depending on the value of the Reynolds number, which can be expressed as follows

$$Re_d = \frac{u_m d}{v} \tag{2.3.6}$$

Where

- u_m: The mean flow velocity $[m/s]$.
- d: The diameter of flow $[m]$.
- $v = \mu/\rho$: Kinematic viscosity $[m^2/s]$.
- ρ: Density $[kg/m^3]$.
- μ: The dynamic viscosity $[kg/(m \cdot s)]$.

For lower Reynolds numbers, the boundary layer is laminar and the flow velocity changes uniformly, as shown on the left side of the figure. As the Reynolds number increases (as x increases), the flow becomes unstable. Eventually for higher Reynolds numbers, the boundary layer is turbulent, and the velocity is characterized by unstable (time-varying) swirling flows inside the boundary layer.

Heat transfer at the boundary between a solid surface and a fluid is very complex, however a simplified expression can be given as:

$$q_{flow} = hA_h(T_w - T_\infty) \tag{2.3.7}$$

Where

- h = Convective heat transfer coefficient $[W/(m^2K)]$.
- q_{flow}: Transferred heat of the flow $[W]$.
- A_h = Heat transfer surface area $[m^2]$.
- T_w = Temperature of the solid surface [°C].
- T_{∞} = Temperature of the fluid sufficiently far from the surface [°C].

Typically, the convective heat transfer coefficient for laminar flow is relatively low compared to the convective heat transfer coefficient for turbulent flow. This is due to turbulent flow having a thinner fluid film layer on the heat transfer surface [49].

2.4 Overview of Thermal Modelling Methods

Accurate thermal analysis modelling tools can assist both the design optimization and real-time operation of power electronics systems. Simple compact thermal models based on lumped parameter networks are commonly used in power electronics design.

Despite their computational efficiency, lumped parameter models (LPM) are of limited use at the design stage as they typically rely on empirical calibration, with values that cannot be directly correlated with design parameters such as topology of the layout, environmental and operating conditions.

Accurate physical representation of the converter topology and environment conditions can be obtained with numerical tools that produce a discretized version of the distributed partial differential equations (PDEs) that model the heat-transfer.

Consequently, compact lumped parameter thermal modelling methods and geometry-based numerical thermal models, will be review to describe heat transfer phenomena. Before attempting to analyse the heat transfer problem, some terminologies such as power losses and thermal impedance, need be introduced with physical representation of the converter topology.

2.4.1 Compact Lumped Parameter Thermal Modelling

Power losses of semiconductors can be calculated using standard methods for the estimation of conduction and switching losses in PWM inverters [50] via temperature-dependent device characteristics [51]. Power losses within a power module need to be transferred and dissipated from the semiconductor chip to the ambient through the connection layers and the heat sink [52], as is shown in Figure 2.13.

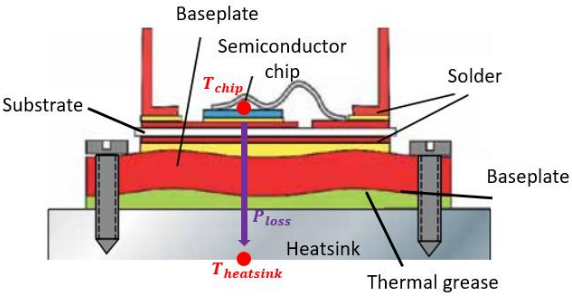

Figure 2.13 Simplified hear transfer in a power module with heatsink [52] .

The effect of power losses P_{loss} on static and dynamic states can be expressed by the temperature difference as follows

$$\Delta T = T_{chip} - T_{heatsink} \tag{2.4.1}$$

Where

- T_{chip} : Semiconductor temperature [°C].
- $T_{heatsink}$: Heatsink temperature [°C].

The thermal impedance Z_{th} can be expressed based on (2.4.1) as follows

$$Z_{th} = \frac{T_{chip} - T_{heatsink}}{P_{loss}} \tag{2.4.2}$$

Thermal impedances which describe the dynamic heat dissipation behaviour are indicated numerically as thermal resistance (R_{th}) and thermal capacitance (C_{th}) of a thermal RC network.

The thermal resistance for a cuboid of solid material is given by:

$$R_{th} = \frac{l}{k_{th} \cdot A_{th}} \tag{2.4.3}$$

Where

- l: Material thickness $[m]$.
- k_{th}: Heat conductivity $[W/(m \cdot K)]$.
- A_{th}: Heat flow area $[m^2]$.

The equation for thermal capacitance is:

$$C_{th} = c_p \cdot \rho V \tag{2.4.4}$$

Where

- c_p: Specific heat capacity $[J/(K \cdot kg)]$.
- ρ: Density $[kg/m^3]$.
- V: Volume $[m^3]$.

Based on the thermal resistance R_{th} and thermal capacitance C_{th}, thermal equivalent circuits can be applied in one dimensional (1D) heat transfer analysis [53] [54]. The temperature of power modules can be expressed using a function of time as $T(t)$. Utilizing this idealized heat transfer analysis based on a lumped parameters model, provides great simplification in 1D heat transfer problems without sacrificing accuracy. Simple compact thermal models based on lumped parameter networks such as those based on Cauer or Foster networks are commonly used in power electronics design.

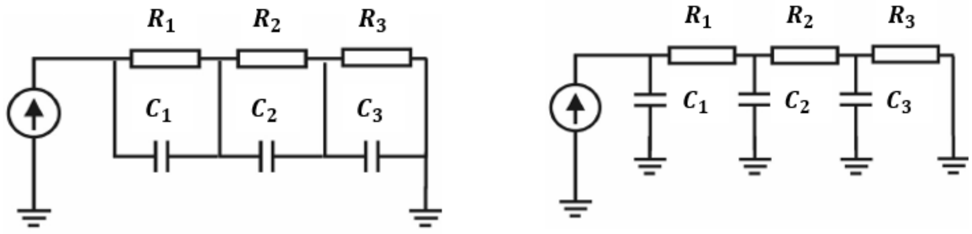

(a) Foster network.

(b) Cauer network.

Figure 2.14 Foster network and Cauer network [53]

Cauer network and Foster network are shown in Figure 2.14. For one-dimensional heat conductive issue, if the thermal element is subdivided into a lot of small states with a thickness closed to zero, Cauer ladder network can be established. The transformation from Cauer network to Foster network [55] [56] can be established based on standard circuit analysis. Compared with Foster network, the Cauer network is closer to the physical state of the thermal circuit due to the fact that each node's temperature represents the temperature of a physical node at a specific location in the 1D representation. On the contrary, the internal nodes of the Foster network do not represent physical nodes inside the material, and only the first node temperature represents the actual temperature of the surface.

Employing the Cauer network, the thermal behaviour of power modules with heatsinks can be modelled as a 1D heat transfer problem. Figure 2.15 shows the Cauer network of the model illustrated in Figure 2.13. The Cauer network can supply a compact thermal model and its implementation is relatively easy, but they cannot model 3D temperature distribution of the complete power module [57].

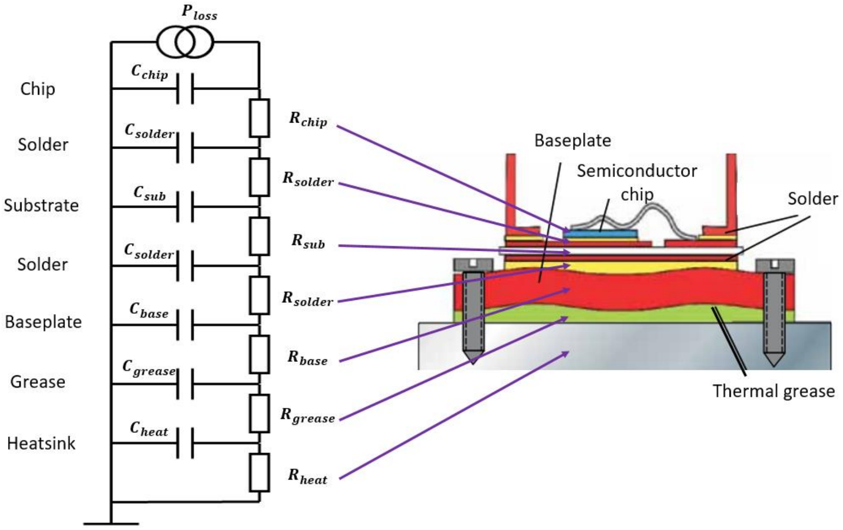

Figure 2.15 Cauer network.

Consequently, in order to model the thermal transfer in a complete power converter including different elements, packaging, and cooling systems, a more accurate and physically representative method is needed. The geometry-based thermal impedance model provides 3D spatial temperature information [57], offering the advantage of providing a tool to support the module design process as it depends directly on the topology.

2.4.2 Geometry-based Thermal Modelling

Geometry-based heat transfer analysis relies on numerical methods that discretize the distributed partial differential equations (PDE) [58] [59] on a grid of small elements. The temperature field within each element is then approximated as a simple function, such as a linear or quadratic polynomial, with a finite number of degrees of freedom (DOFs).

The two most common discretization methods are the finite element method (FEM) [60] and finite differences method (FDM) [61] [62] methods. While these methods are quite similar in their aim i.e. providing a numerical method for solving PDEs on a discrete grid, their mathematical formulation is quite different. A very brief introduction is given in the following.

2.4.2.1 Finite Element Method

FEM is a computational method that subdivides the problem geometry into very small but finite-sized elements of geometrically simple shapes, typically triangles or squares. The process of FE analysis is shown in Figure 2.16.

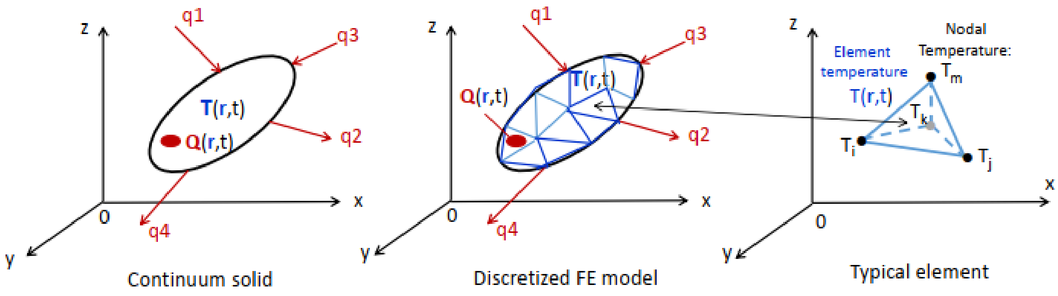

Figure 2.16 FE thermal analysis [63].

The collection of all these simple shapes constitutes the so-called finite-element mesh. The next step is to discretize the equations for the temperature field, mathematically represented by the heat equation PDEs and formulate these equations for each element, approximating the temperature solution with a low order, e.g. linear, variation over each element [63].

The FE discretization of the PDE is then obtained with the Galerkin method [64]. This gives an approximate local description of the physics by a set of simple linear (but sometimes nonlinear) equations.

The approach of the FEM can be summarised as follows

- Create geometry and define material properties.
- Discretization of the geometry.
- Choose initial and boundary conditions.
- Element formulation and development of equations for elements.
- Obtain equations for the entire system from the equations for one element.
- Solving the equations.

Many commercial software packages are available that implement the FEM for a number of physics problems including thermal modelling. One of these, Ansys, will be used for validation in subsequent chapters.

2.4.2.2 Finite Differences Method

FDM is the most direct approach to discretizing partial differential equations. The method is not usually used for irregular CAD geometries as FEM but more often for rectangular or cuboid-shaped models. In Figure 2.17, the basic principle of FD analysis is shown for a 1D problem where the space is discretized in the x-direction with discretized nodes x and time t is discretized in the vertical direction.

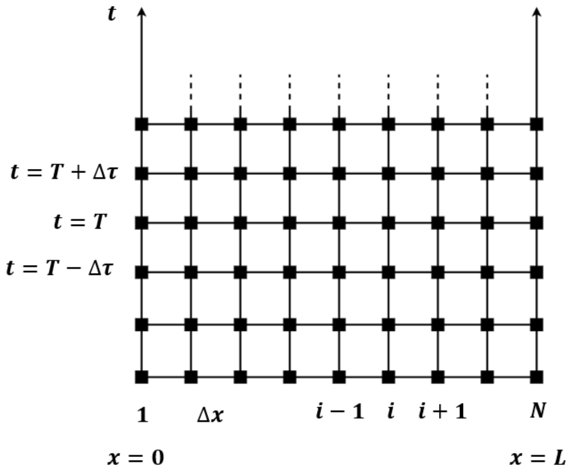

Figure 2.17 One dimensional FD thermal analysis.

In the x-direction, the heat equation can be written as

$$\frac{1}{\alpha}\frac{\partial T}{\partial t} = \frac{\partial^2 T}{\partial x^2} \qquad (2.4.5)$$

Then, the second partial derivatives of equation (2.4.5) may be approximated by

$$\frac{\partial^2 T}{\partial x^2} \approx \frac{1}{(\Delta x)^2}(T_{i+1} + T_{i-1} - 2T_i) \qquad (2.4.6)$$

And the time derivative of equation (2.4.5) can be approximated by:

$$\frac{\partial T}{\partial t} \approx \frac{1}{\Delta\tau}\left(T_i^{T+\Delta\tau} - T_i^T\right) \tag{2.4.7}$$

A finite-difference scheme can thus be devised to take heat generation into account with the term $\dot{q}/k$ into the general equation and obtain

$$\frac{1}{\alpha}\frac{T_i^{T+\Delta\tau} - T_i^T}{\Delta\tau} = \frac{T_{i+1}^T + T_{i-1}^T - 2T_i^T}{(\Delta x)^2} + \frac{\dot{q}}{k} \tag{2.4.8}$$

The FDM can also be extended to three-dimensional (3D) problems. In a 3D cube can be expressed in the similar way with Figure 2.18.

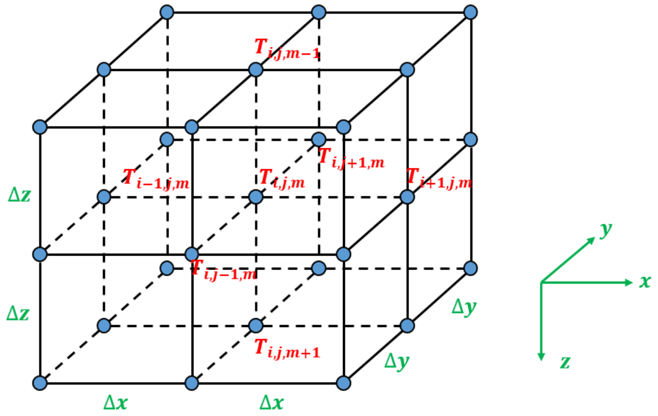

Figure 2.18 Three dimensional FD thermal analysis.

Given a node (i, j, m) in a space defined by a coordinate system (x, y, z, t) as follows

$$\frac{1}{\alpha}\frac{T_{i,j,m}^{T+\Delta\tau} - T_{i,j,m}^T}{\Delta\tau} = \frac{\dot{q}}{k} + \frac{T_{i+1,j,m}^T + T_{i-1,j,m}^T - 2T_{i,j,m}^T}{(\Delta x)^2} + \frac{T_{i,j+1,m}^T + T_{i,j-1,m}^T - 2T_{i,j,m}^T}{(\Delta y)^2} + \frac{T_{i,j,m+1}^T + T_{i,j,m-1}^T - 2T_{i,j,m}^T}{(\Delta z)^2} \tag{2.4.9}$$

By combination of the differential equations of all cubes together, a multi-input-multi-output (MIMO) system of ordinary differential equations (ODE) can be obtained as

$$C\dot{T}(t) + KT(t) = FQ(t)$$

$$y = E^T T(t) \tag{2.4.10}$$

Where

- $K(x, y, z)$: The thermal conductivity matrix.

- $C(x, y, z)$: The heat capacity matrix.
- $Q(x, y, z, t)$: The heat source generated from $q(x, y, z, t)$.
- T : The temperature distribution vectors.
- y : The chosen output temperature distribution vectors.
- $F \in R^{n\times m}$: The input matrix.
- $E \in R^{n\times p}$: The output matrix.
- n: The dimension of state space.
- m: The number of inputs.
- p: The number of outputs.

2.4.2.3 Summary

One important difference among FEM and FDM is the ease of implementation. A common opinion is that FDM is easier to be implemented and FEM is more difficult. One reason for this is that FEM requires quite sophisticated mathematics for its formulation. FDM are thus one of the most efficient approaches of modelling dynamic thermal systems [65].

It is worth noting that the size of ODE systems generated from FDM equations is directly related to the size of the discretization steps. For a 1D problem, the number of ODE is inversely proportional to Δx and therefore the smaller the discretization, the larger the number of equations. For a 3D problem, the number of ODEs will be inversely proportional to $\Delta z \cdot \Delta y \cdot \Delta z$ and therefore resulting in a much larger system of equations. A fine discretization, produces better spatial resolution at the price of an increased computational complexity.

The ODE system resulting from the application of the FDM to a power electronic converter can easily have millions of equations. The resulting computational complexity justify the need to research methods for model order reduction. This will be one of the main topic of the thesis and the literature on the topic is briefly summarized in the following section.

2.5 Overview of Model Order Reduction Methods

Most of the power electronics system thermal design processes still rely on the geometry-based empirical methods based on FDM with model order reduction (MOR) [66]. For example, Yang [67] presented a model order reduction technique for microelectromechanical systems (MEMS) heat-transfer system-level modelling. The numerical models generated by the FDM solver can be reduced into low-order models with the help of MOR techniques. Except for heat-transfer thermal modelling, FDM with MOR can also be applied in vast fields for power electronics industry. As an example, Cangellaris [68] proposed reduced order models based on FDM for the development of the discrete approximation to the transmission line equations on the interconnections.

Model order reduction is not only used for the reduction of the electro-thermal system generated by the FDM, but also for power electronics systems modelling directly. As an example for physics-based modelling of power electronics systems, Davoudi [69] introduced a reduced-order high-fidelity magnetic equivalent circuits (HFMEC) modelling approach for single-winding systems. Indeed model order reduction has found widespread use in the electronics industry [70]. The underlying idea of MOR is relatively simple, approximating the moments of the transfer function of the original ODE system [71].

The ODE system obtained after the application of the FDM shown in (2.4.10) can be written in the standard state-space model as:

$$\dot{T}(t) = AT(t) + BQ(t)$$

$$y(t) = E^T \cdot \dot{T}(t) \tag{2.5.1}$$

Where the vector of temperatures in each node T becomes the state variable. The output of the system y is the vector of temperature in a selected subset of nodes of interest.

- $A = -C^{-1}K \in R^{n\times n}$
- $B = C^{-1}F \in R^{n\times m}$
- $E \in R^{n\times p}$: The output matrix.
- n: The dimension of state space.
- m: The number of inputs.
- p: The number of outputs.

Generally, it is assumed that m and p are much smaller than n. The size of ODE systems generated from FDM equations is directly related to the spatial resolution of the discretization. The complex structure of power modules results in an extremely large size of ODE system, and usually containing millions of FDM equations. Even if modern computers can solve engineering problems of large size, system-level simulation will be extremely expensive computationally with the direct use of the full order model. To overcome these limitations, the 3D dynamic FD models can be combined with model order reduction (MOR) techniques.

MOR methods can be more easily described using the system transfer functions [71]. The transfer function of state-space system shown in (2.5.1) is defined as:

$$G(s) = \frac{y(s)}{Q(s)} = E^T(sI - A)^{-1}B \tag{2.5.2}$$

Where

- s: The Laplace variable
- I: The unity matrix $\in R^{n\times n}$.

It is evident that there is an inverse calculation of matrix A, which has a large dimension. To reduce the number of state vectors, state vector T can be transformed via a reduction matrix $V_n \in R^{n\times n}$ as follows

$$T = V_n \cdot z \tag{2.5.3}$$

Where z is the new state vectors expressed by the matrix V_n. It should be noted that T has physical meaning while z does not. Each column of the matrix V_n can be seen as a linear combination of transfer function $G(s)$. A number of methods have been proposed to truncate parts of the generalized states and consequently, reduce the dimension of the system (2.5.1) while keeping accuracy [72].

Equation (2.5.1) can be written using (2.5.3) as

$$\begin{gathered} \dot{z}(t) = W_n^T A V_n \cdot z(t) + W_n^T B Q(t) \\ y(t) = E^T V_n \cdot z(t) \end{gathered} \tag{2.5.4}$$

Where

- $W_n, V_n \in R^{n\times n}$
- $W_n^T \cdot V_n = I$

W_n and V_n are biorthogonal and $W_n^T \cdot V_n = I$. It can be proved that the transfer function $G(s) = y(s)/Q(s)$ of system (2.5.4) is the same with (2.5.2) after the transformation.

Model reduction methodologies to find such a transformation representing the state vectors with less generalized coordinates [72], which means a transformation can be made to approximate state vector T when most of the coordinates are removed (truncated) as follows

$$T = [V_r \quad V_{n-r}] \cdot \begin{bmatrix} z_1 \\ z_2 \end{bmatrix} \tag{2.5.5}$$

Through

$$T = V_r \cdot z_1 + \varepsilon \tag{2.5.6}$$

With a small error vector ε. Therefore, system (2.5.4) can be changed to a low dimensional system as follows

$$\begin{aligned} \dot{z}_1(t) &= A_r \cdot z_1(t) + B_r Q(t) \\ y(t) &= E_r^T \cdot z_1(t) \end{aligned} \tag{2.5.7}$$

Where

- $A_r = W_r^T A V_r$
- $B_r = W_r^T B$
- $E_r = V_r E$
- $W_r^T \cdot V_r = I$

The transfer function of the reduced-order system can be defined as:

$$G_r(s) = {E_r}^T (sI - A_r)^{-1} B_r \tag{2.5.8}$$

System (2.5.7) has the same input number and output number with system (2.5.1), while the number of equations is smaller. This transformation from full-order to reduced-order state-space system is shown in Figure 2.19.

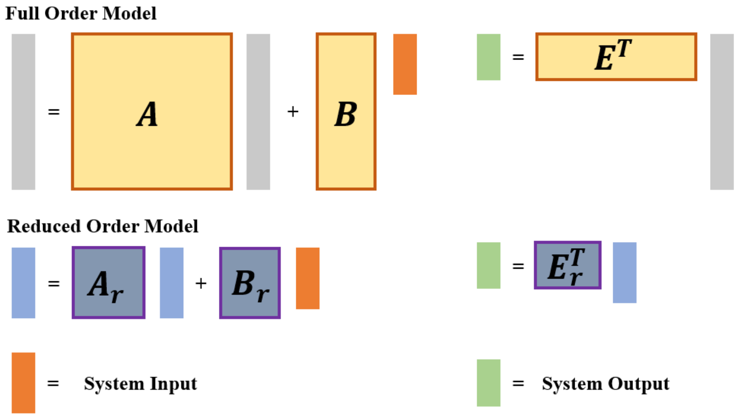

Figure 2.19 Transformation from full-order to reduced-order state-space system

The aim of model order reduction techniques is to minimize the error ε in time domain $min\|y(t) - y_r(t)\|$ or Laplace domain $min\|G(s) - G_r(s)\|$. For linear ODE system, vast model order reduction techniques can be applied to minimize these errors ε, such as truncation methods, Padé-type approximants via Krylov subspace, Guyan-based methods, etc. These order reduction methods will be introduced and compared in this section.

2.5.1 Model Order Reduction Methods Based on Balanced Truncation

Passivity is a fundamental property of many physical systems which may be roughly defined as the characteristic of a system that dissipates rather than producing energy. It is an inherent input-output property in the sense that it quantifies and qualifies the energy balance of a system. Non-passive reduced models may cause nonphysical behaviour in circuit simulators, such as by generating energy at high frequencies that causes erratic or unstable time-domain behaviour. Consequently, the passivity should also be guaranteed in the reduction.

Before going into the details of passive reduction methods, two important characteristics of the system (A, B, E) in equation (2.5.1), controllability and observability, need to be introduced. A system is controllable if for any initial state $T(t_0) = T_0$ and any final state T_l , there is an input $Q(t)$ that can transfer T_0 to T_l in a finite time [73]. A system is observable if it is possible to calculate any unknown initial state $T(t_0) = T_0$ uniquely from the given input $Q(t)$ and the measured output $y(t)$ over a finite time interval [73].

Controllability and observability can be quantified according to control theory, through the controllability and observability matrices P and O, respectively [74], defined as:

$$P = \int_0^\infty e^{At} B B^T e^{A^T t} dt$$

$$O = \int_0^\infty e^{A^T t} E^T E e^{At} dt \tag{2.5.9}$$

The matrices P and O are the unique solutions of two Lyapunov equations [74]. It can be found in [75] that the criteria of the balanced system (A, B, E) for controllability and observability are that both P and O should be regular.

After finding the two matrices P and O, a state space transformation can be obtained to balance the system. The transformation proposed by B. C. Moore [76] can balance the system based on equal and diagonal P and O as follows

$$P = O = diag(\sigma_1, \dots, \sigma_n) \tag{2.5.10}$$

The parameters $\sigma_1, \sigma_2 \dots \sigma_n$ are called Hankel singular values (HSV), which can be computed as the square roots of eigenvalues of the product of P and O. HSVs are property of the system and depend only on input-output behaviour [77]. HSVs reflect the contributions of different entries of the state vector to system responses [77]. Consequently, to reduce the order of the original system (A, B, E), it is sufficient to truncate those state variables related to the minimum HSV [77]. Balanced truncation can be done at the same time by applying the projection to the original unbalanced system using a square root algorithm [78-80]. A provably passive balanced truncation method is presented in [81] [82]. The balanced truncation reduction method is to find the reduced-order model by finding and deleting those states with the lowest controllability and observability at the same time.

An important characteristic of balanced truncation is that it can calculate a global error range between the transfer functions of the original full-order and the reduced-order systems [77] as follows

$$\|G(s) - G_r(s)\|_\infty \leq 2(\sigma_{r+1} + \cdots + \sigma_n) \tag{2.5.11}$$

Where the infinity norm $\|G(s) - G_r(s)\|_\infty$ denotes the largest magnitude of the difference of transfer functions $G(s)$ and $G_r(s)$. The proof of (2.5.11) is given in [77] and discussion of different error norms can be found in [83].

Thanks to the simplicity and the computational efficiency, balanced truncation reduction methods are frequently used [77]. It can be proved that the balanced truncation reduction techniques maintain the stability and passivity of the full-order system within a reduced-order system [84] while a disadvantage is that it does not guarantee zero error in steady state, which is an important requirement in many practical applications such as the temperature estimation of power electronics system.

Nevertheless, balanced truncation reduction methods are mathematically optimal, offering a global error estimate for the difference between the transfer function of the original high-dimensional and reduced low-dimensional system. They show that model reduction of a linear dynamic systems is solved in principle, but require a large computational complexity. For this reason, balanced truncation reduction methods are only applicable to small linear systems [73].

2.5.2 Model Order Reduction Methods Based on Krylov Subspace

Similar to balanced truncation reduction methods, the reduction techniques based on Krylov subspace require a single matrix representation of a first order ODE system [73]. Equation (2.4.10) can be rewritten as

$$A_K\dot{T}(t) = T(t) + B_K \cdot Q(t)$$

$$y = E^T \cdot T(t) \tag{2.5.12}$$

Where

- $A_K = -K^{-1}C$
- $B_K = -K^{-1}F$

To make the derivation clear, reduction algorithm based on Krylov subspace is described here with reference to a single-input-single-output (SISO) case, i.e. $m = p = 1$ (for SISO the lower case letters b and e are used for the input and output values) as equation (2.5.12). Krylov subspace reduction in multi-input-multi-output (MIMO) can be obtained using the similar methods.

$$A_K\dot{T}(t) = T(t) + b \cdot Q(t)$$
$$y = e^T \cdot T(t) \tag{2.5.13}$$

The SISO transfer function can be defined as:

$$G(s) = -e^T(I - sA_K)^{-1}b \tag{2.5.14}$$

The Taylor series expansion of $G(s)$ about $s_0 = 0$ is given by:

$$G(s) = -e^T(I + sA_K + s^2A_K^2 + \cdots)b_K = \sum_{i=0}^{\infty} m_i s^i \tag{2.5.15}$$

Where $m_i = -e^T A_K^i b_K$ are called moments about s_0.

Model order reduction methods based on Krylov subspace correspond to the selection of $G_r(s)$ as a Padé approximant of $G(s)$. The r-th Padé approximant of $G(s)$ about the expansion point s_0 can be expressed as follows [73]:

$$G_r(s) = \frac{P_{r-1}(s)}{O_r(s)} = \frac{a_{r-1}s^{r-1} + \cdots + a_1 s^1 + a_0}{b_r s^r + b_{r-1}s^{r-1} + \cdots + b_1 s^1 + b_0} \tag{2.5.16}$$

Where the coefficients $a_0, a_1, \dots, a_{r-1}$ will be derived in the following. This rational function consists of Taylor series around s_0 agrees with the Taylor series of $G(s)$ in the first $2r$ terms (moments) [73], i.e. for $s_0 = 0$:

$$G(s) = G_r(s) + O(s^{2r}) \tag{2.5.17}$$

Where

$$\lim_{s \to s_0} O(s^{2r}) = 0 \tag{2.5.18}$$

And $G_r(s)$ is called a Padé-type approximant. Detailed overview of Padé-type approximant can be found in [85].

Explicit moment computations can be used to calculate Padé approximants, which is similar to the process using Asymptotic Waveform Evaluation algorithm [86]. However, the computation is numerically unstable [87]. It has been demonstrated that the Krylov subspaces are numerically stable. They are defined as follows:

For $r = 1,2, \dots$, the r-th right Krylov subspace $K_r^R\{A_K, b\}$ can be given as

$$K_r^R\{A_K, b\} = span\{b, A_K b, \dots, A_K^{r-1} b\} \tag{2.5.19}$$

And the r-th left Krylov subspace $K_r^L\{A_K, b\}$ can be given as

$$K_r^L\{A_K, b\} = span\{e, A_K^T e, \dots, (A_K^T)^{r-1} e\} \tag{2.5.20}$$

It should be noted that moments can be computed from (2.5.19) and (2.5.20) by calculating the inner products [73] as follows:

$$m_{2i} = -\left((A^T)^i e\right)^T \cdot \left(A^i b\right) \ and \ m_{2i+1} = -\left((A^T)^i e\right)^T \cdot \left(A^{i+1} b\right) \tag{2.5.21}$$

for $i = 0,1, \dots, r-1$.

The vectors from (2.5.19) and (2.5.20) quickly become almost linearly dependant [87]. The solution is to construct more stable basis vectors $v_1, v_2, \dots, v_r$ and $w_1, w_2, \dots, w_r$ saved in columns of matrices W and V, such that $K_r^R\{A_K, b\} = span\{v_1, v_2, \dots, v_r\}$ and $K_r^L\{A_K, e\} = span\{w_1, w_2, \dots, w_r\}$.

There are two main methods, the Lanczos algorithm and the Arnoldi process, can be used to construct basis matrices W_r and V_r for Krylov subspace. The main advantage of the Lanczos algorithm is that it can be uniquely specified, because it matches a maximal number $(2r)$ of moments. Research in [88] proposed an algorithm for the basic Lanczos process.

However, it is worth noting that the basic Lanczos algorithm stops prematurely, result from the fact that $w_i^T v_i \approx 0$ occurs in actual implementations [73]. It is suggested in [89] that this problem can be solved by introducing a more complex Lanczos process. Another disadvantage of the Lanczos algorithm is that the resulting reduced-order model may not be passive and stable generally [90].

Different from Lanczos algorithm, the Arnoldi process produces only a sequence of vectors $v_1, v_2, \dots, v_r$ spanning the right Krylov subspace $K_r^R\{A_K, b\}$ as shown in (2.5.19) [73]. Algorithm derived by Freund [91] statement of the Arnoldi method.

The disadvantage of the Arnoldi process is that the Arnoldi method needs large calculation load. Each new Arnoldi vector should be orthogonal to all previously generated vectors [73], which means that the computational workload increases in proportion to the size of the subspace. However, Freund also found that the reduced order model will also be stable and passive if the Arnoldi-based projection is applied in stable and passive ODE system [92]. Consequently, the Arnoldi process has some optimizations to obtain guaranteed stability and passiveness.

Another disadvantage of the Arnoldi method is the half number of matched moments compared with compared with Lanczos algorithm, resulting in that fact that the reduced-order model generated by the Arnoldi process is more different from the original model. It is possible to increase the number of matched moments by considering the account the output vector, as the methods derived in [93] [94]. However, the shortage if this solution is making the algorithm becomes more complex and loses the stability and passivity.

As a conclusion, the Arnoldi process is less complicated and can preserve the stability and passiveness of the original system. The important properties of Arnoldi process and Lanczos algorithm are summarized in Table 2.2 [73].

Table 2.1 Comparison of Arnoldi and Lanczos.

	Arnoldi	Lanczos
Accuracy of approximation	r moments match	$2r$ moments match
Invariance properties	No	Yes
Numerical stability	Yes	No
Preservation of stability and passivity	Yes	No
Complete output approximation	Yes	No

2.5.3 Model Order Reduction Methods Based on Guyan Algorithm

The Guyan algorithm [95] [96] is one of the model order reduction techniques projecting an ODE system of a high dimension to a lower-dimensional one. For the ODE system expressed in equation (2.4.10), the steady-state equation can be written as

$$K \cdot T(t) = F \cdot Q(t) \tag{2.5.22}$$

Guyan-based MOR can preserves the terminal nodes physically, as shown in Figure 2.20.

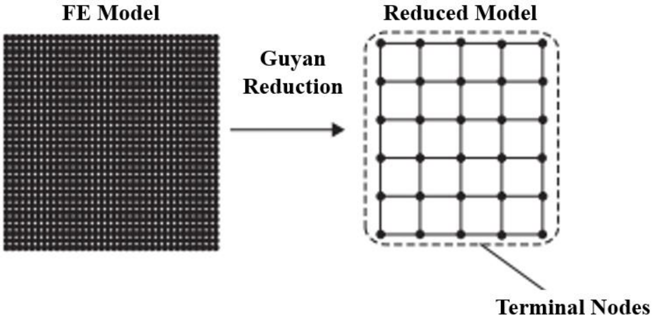

Figure 2.20 Schematics of Guyan-based model order reduction [73].

The linear system (2.5.22) can thus be decomposed into terminal and internal equations by as follows [95]:

$$\begin{bmatrix} K_{ee} & K_{ei} \\ K_{ie} & K_{ii} \end{bmatrix} \begin{bmatrix} T_e(t) \\ T_i(t) \end{bmatrix} = \begin{bmatrix} F_e \\ F_i \end{bmatrix} \tag{2.5.23}$$

Where

- e: Index sets to range external nodes.
- i: Index sets to range internal nodes.
- F_e, F_i: Simplified input vectors considering the input term $Q(t)$.

Equation (2.5.23) can be written as follows

$$F_e = K_{ee}T_e(t) + K_{ei}T_i(t) \tag{2.5.24}$$

$$F_i = K_{ie}T_e(t) + K_{ii}T_i(t) \tag{2.5.25}$$

$T_i(t)$ can be expressed by write equation (2.5.25) as

$$T_i(t) = K_{ii}^{-1} \cdot (F_i - K_{ie}T_e(t)) \tag{2.5.26}$$

And insert (2.5.26) in (2.5.24) then obtain:

$$F_e - K_{ei}K_{ii}^{-1}F_i = \left(K_{ee} - K_{ei}K_{ii}^{-1}K_{ie}\right)T_e(t) \tag{2.5.27}$$

The number of chosen terminal nodes determines the dimension of the reduced order system expressed in equation (2.5.27). Then the reduced heat conductivity matrix and input vectors can be defined as follows

$$K_r = K_{ee} - K_{ei}K_{ii}^{-1}K_{ie} \tag{2.5.28}$$

$$F_r = F_e - K_{ei} K_{ii}^{-1} F_i \tag{2.5.29}$$

Guyan assumed that no input vectors were applied on the internal nodes ($F_i = 0$). In this case, the equation (2.5.26) changes into:

$$T_i(t) = -K_{ii}^{-1} K_{ie} T_e(t) \tag{2.5.30}$$

In linear algebra operations, the Schur complement amounts to a coordinate transformation of the form $T(t) = V_G \cdot T_e(t)$ can with V_G as follows [95]

$$V_G = \begin{bmatrix} I \\ -K_{ii}^{-1} K_{ie} \end{bmatrix} \tag{2.5.31}$$

Assuming K is a symmetric matrix and therefore $K_{ie}^T = K_{ei}$ and $\left(K_{ii}^{-1}\right)^T = K_{ii}^{-1}$. The reduced heat conductivity matrix expressed in equation (2.5.28) and input vectors expressed in equation (2.5.29) thus can be written as follows

$$K_r = V_G^T \cdot K \cdot V_G \tag{2.5.32}$$

$$F_r = V_G^T \cdot F \tag{2.5.33}$$

Moreover, the heat capacity matrix C in dynamic ODE system (2.4.10) can be given through via the similar transformation as

$$C_r = V_G^T \cdot C \cdot V_G \tag{2.5.34}$$

The obtained K_r, C_r and F_r can be introduced to form the reduced thermal system as follows [95]

$$C_r \dot{T}_e(t) + K_r T_e(t) = F_r \tag{2.5.35}$$

Where

- $K_r = V_G^T \cdot K \cdot V_G$
- $C_r = V_G^T \cdot C \cdot V_G$
- $F_r = V_G^T \cdot F$

The main advantage of Guyan-based MOR is that it physically retains the terminal nodes. However, Guyan-based MOR methods cannot supply strict guidelines about choosing the terminal nodes [73]. Moreover, only when the number of selected terminal nodes is large enough, the improved Guyan method can provide sufficient accuracy for reducing the thermal system, which may lead to unnecessary large-scale model after reduction. Consequently, Guyan reduction methods are not suitable to large linear systems.

2.5.4 Summary

So far, most of the practical work of model reduction of large-scale linear dynamic system has been bound to the Padé approximation of the transfer function base on the Krylov subspace [73]. These methods lack the estimation of global error, but can be used in extremely high-dimensional order linear systems. SISO case is introduced in this section, which just contained one starting vector v. Arnoldi process and Lanczos algorithm in MIMO model can be obtained using the similar method, called block Arnoldi process and block Lanczos algorithm respectively [93]. Compared with block Lanczos algorithm, block Arnoldi process has better mathematical simplicity and numerical stability. Consequently, Arnoldi process or block Arnoldi process will be developed in the thesis for model order reduction of thermal analysis.

The properties of those model order reduction methods are listed in Table 2.2 [73].

Table 2.2 Methods for model order reduction of linear dynamic systems.

	Advantages	Disadvantages
Balanced truncation reduction methods	Can estimate global error. Fully automatic reduction.	Lack the approximation of steady state error.
Padé approximants via Krylov subspaces	Can be used in extremely high-dimensional order linear systems.	Lack a global error estimation. The order of reduced systems need be selected manually.
Guyan algorithm	Can maintain the physical nodes	Unnecessary large reduced models.

Generally, the factors affected the efficiency of MOR techniques can be classified into algorithm-related factor and algorithm-independent factor. The algorithm-related factor is the rank of matrix approximation. Hankel Singular Values (HSVs) supply the property of the system, reflecting the contributions of different entries of the state vector to system responses [77]. Due to some specific MOR techniques, e.g. the low rank Gramian approximation algorithm expressed by Floros [97], less HSVs are computed until the convergence of the algorithm. The less number of calculated HSVs results in low memory requirements for the system matrix storage [97], contributing the high efficiency of reduction process. The algorithm-independent factor is the number of external terminals. The efficiency of model order reduction degrades with the increased number of external terminals to the full-order model [98]. The reason for the degradation is fundamental and independent on the particular reduction algorithm [98].

Except for the efficiency, the accuracy of MOR techniques should also be considered. The accuracy of MOR techniques can be evaluated by the information disturbance between the original system and reduced system. Since the goal of MOR techniques is approximating well circuit behaviour at the needed external terminals but sacrifice the information at internal nodes, the information loss caused by internal node elimination should be considered.

In this thesis, the concerned case is thermal equivalent circuit matrices, which are sparse matrices due to limited heat conduction paths within the single solid medium. Most of the element are zero and this kind of sparse matrices can be reduced into smaller-scale matrices with limited information loss. It is also practical for the application of MOR techniques in systems with large-scale dense matrices. However, the behaviour especially the transient behaviour of the low-order system reduced from large-scale dense matrix systems cannot be guaranteed due to the increased information loss. For example, the transient response of the reduced thermal modelling matrices might be unreasonably fast with decreasing reduced order, due to the loss of mass information contained in the eliminated internal nodes. Unlike the MOR techniques relying on the selection of terminal nodes e.g. Guyan reduction, Arnoldi process or block Arnoldi process expressed in this thesis can avoid the unnecessary information loss cause by the selection of external and internal nodes. Consequently, how to choose a proper reduced order is critical to maintain the accuracy of reduced system via MOR process in this thesis.

2.6 Overview of State Observers for Real-Time Temperature Estimation

In the Section 2.3 and 2.4, thermal modelling methods have been reviewed, including dynamic compact thermal modelling and geometry-based thermal modelling, for the targets to support real-time applications and optimised design of power devices respectively. Compared with numerical methods for geometry-based heat transfer analysis reviewed in Section 2.4, compact thermal model has smaller system dimension and less calculation load, reducing the computational complexity of a model.

In real-time applications where a thermal model can be used to estimate the devices temperature, the computational complexity is an important consideration, for example when a thermal model needs to be computed online in an embedded platform based e.g. on a microcontroller with limited computational capabilities. In these cases, very compact models are required. Additionally, the numerical models described in the previous sections can be considered as “open-loop” estimators since there is no feedback mechanism that can correct errors due to e.g. unknown parameters or unknown or imprecisely defined boundary conditions, e.g. ambient conditions. In order to provide a more robust temperature estimation in practical applications, observer-based temperature estimation methods have been proposed. These typically provide a closed-loop feedback mechanism that uses one or more measurements to provide a correction mechanism and therefore reduce estimation errors.

State observers and their applications to temperature estimation are briefly reviewed in the following.

A state observer is a simulation system that models the dynamics of a real system in order to provide an estimate of the internal states of the real system. State estimation algorithms applicable to a wide range of thermal analysis and temperature monitoring. Examples of thermal observers which have been developed and analysed can be found in [99-101]. The simplest methods rely on open-loop estimations which predict the devices temperature based on loss and thermal models [102]. However, the accuracy of these models and the sensitivity to uncertainties in operating conditions, e.g. cooling and ambient temperature, or device parameters, might affect the accuracy of estimation. Closed-loop estimation methods using observers can been proposed to address some of these drawbacks.

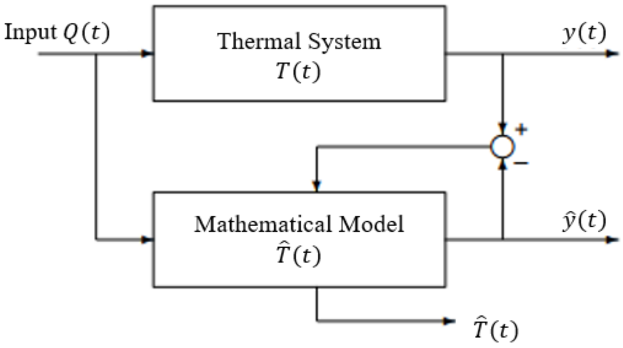

Figure 2.21 Block diagram of a closed-loop state observer.

The block diagram of the closed-loop state observer is shown in Figure 2.21. The top block represents a physical thermal system of power electronics devices and its measurements are represented by $y(t)$. The bottom block is a mathematical model fed by the same input vectors $Q(t)$ with the physical thermal system, and provides the estimation of the internal temperature states $\hat{T}(t)$. Then the model output $\hat{y}(t)$ can be compared with real measured output $y(t)$. The error between these two signals can be injected into the mathematical model to correct the errors of estimated internal temperature states $\hat{T}(t)$.

Some typical closed-loop observers, including Luenberger observer, unknown input observer and reduced-order observer will be reviewed in this section.

2.6.1 Luenberger Thermal Observer

Motivated by the need for measured feedback and armed with the observability concept, a simple observer design is necessary [103]. This design is based on eigenvalue assignment and is known as the Luenberger observer.

Luenberger thermal observer can be designed as follows [104].

$$\frac{d\hat{T}(t)}{dt} = A\hat{T}(t) + BQ(t) + L[y(t) - \hat{y}(t)]$$

$$\hat{y}(t) = E^T \cdot \hat{T}(t) \tag{2.6.1}$$

Where

- $\hat{T}(t)$: The estimated states of the thermal system.
- $\hat{y}(t)$: The observer output.
- L : The gain of observer.
- A, B and E^T: $n \times n, n \times p, q \times m$ constant matrices respectively.
- n: The dimension of state space.
- m: The number of inputs.
- p: The number of outputs.

The block diagram of Luenberger observer can be seen in Figure 2.22.

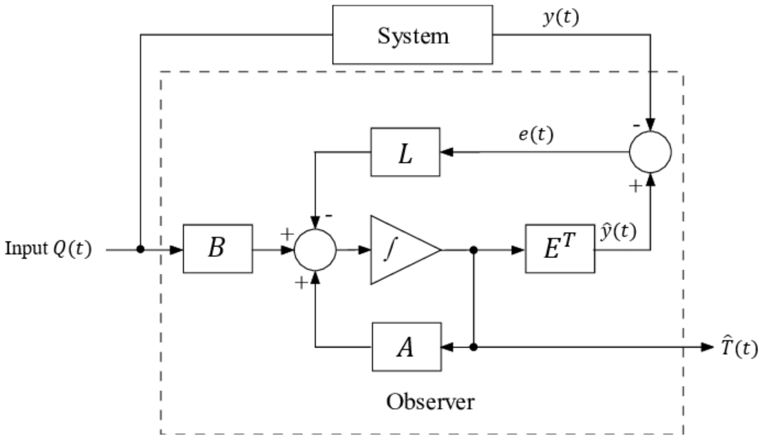

Figure 2.22 Block diagram of Luenberger observer [104].

Observer state error can be defined as

$$e(t) = T(t) - \hat{T}(t) \tag{2.6.2}$$

Differentiating equation (2.6.2) as follows

$$\frac{de(t)}{dt} = \frac{dT(t)}{dt} - \frac{d\hat{T}(t)}{dt} \tag{2.6.3}$$

Substituting equation (2.5.1) and (2.6.1) into (2.6.3) as

$$\frac{de(t)}{dt} = AT(t) + BQ(t) - A\hat{T}(t) - BQ(t) - L[y(t) - \hat{y}(t)]$$

$$\frac{de(t)}{dt} = (A - LE^T)e(t) \tag{2.6.3}$$

Solution of equation (2.6.3) can be given by

$$e(t) = e^{A-LE^T}e(0) \tag{2.6.4}$$

The eigenvalues of the matrix $A - LE^T$ can be made arbitrary by appropriate choice of the observer gain L, when the pair $[A, E^T]$ is observable [104]. The observability and stability of the system need be discussed. The observability of the $[A, E^T]$ can be defined as

$$O = \begin{bmatrix} E^T \\ E^T A \\ E^T A^2 \\ \vdots \\ E^T A^n \end{bmatrix} \tag{2.6.5}$$

$[A, E^T]$ is observable if and only if O is a full-rank matrix [103] [104]. The observer system is stable if the observer gain matrix L is designed to make the eigenvalues of $(A - LE^T)$ have negative real parts.

2.6.2 Unknown Input Thermal Observer

Inputs to a physical systems might often be uncertain or unknown for example when an input is considered as a disturbance. Subject to appropriate observability conditions, observers can be used to estimate the unknown input components or to provide a state estimation that is insensitive to unknown disturbances. System (2.5.1) can be considered as a continuous linear time invariant steady space model with an input disturbance as follows

$$\dot{T}(t) = AT(t) + BQ(t) + B_d d(t)$$
$$y(t) = E^T \cdot T(t) \tag{2.6.6}$$

Where

- $T(t)$: The state vectors of the thermal system.
- $y(t)$: The observer output.

- B_d: The unknown input distribution matrix.
- A, B, B_d and E^T: $n \times n, n \times p, n \times p, q \times m$ constant matrices respectively.
- n: The dimension of state space.
- m: The number of inputs.
- p: The number of outputs.

Based on system (2.6.6), the structure of unknown input observer (UIO) can be expressed as [105-107]

$$\dot{z}(t) = Mz(t) + PBQ(t) + Ky(t)$$

$$\hat{T}(t) = z(t) + Hy(t) \tag{2.6.7}$$

Where

- $\hat{T}(t)$: The estimated states of the thermal system.
- P, K, H, M: The matrices to be designed for achieving unknown input decoupling.

The block diagram of unknown input observer is shown in Figure 2.23.

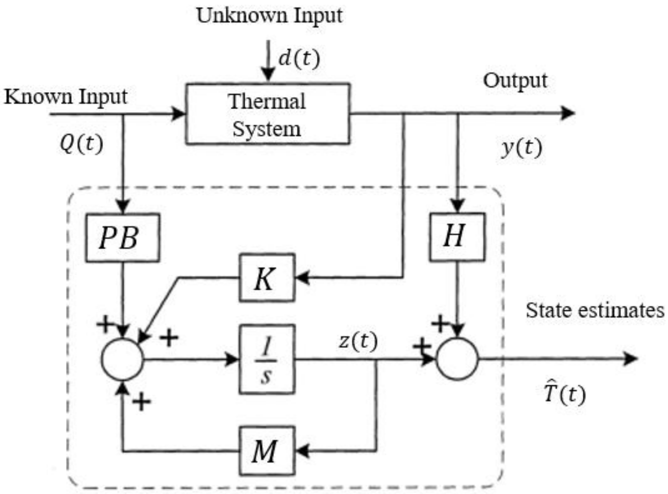

Figure 2.23 Block diagram of unknown input observer [105].

Observer state error can be defined as:

$$e(t) = T(t) - \hat{T}(t) \tag{2.6.8}$$

It is easy to obtain the derivative of state estimation error from equation (2.6.6) and (2.6.7) that [105] [108] [109]

$$\begin{aligned}\dot{e}(t) = {} & [(I - HE^T)A - K_1E^T]e(t) \\ & +[(I - HE^T)A - M - K_1E^T]z(t) \\ & +(I - P - HE^T)BQ(t) \\ & +\{[(I - HE^T)A - K_1E^T]H - K_2\}y(t) \\ & +(I - HE^T)B_d d(t)\end{aligned} \tag{2.6.9}$$

Where

- $K_1 + K_2 = K$
- I: The $n \times n$ identity matrix

In terms of strong disturbance decoupling principle, the traditional UIO theory requires that

- $(I - HE^T)A - M - K_1E^T = 0$
- $I - P - HE^T = 0$
- $[(I - HE^T)A - K_1E^T]H - K_2 = 0$
- $(I - HE^T)B_d = 0$

Then equation (2.6.10) can be written as

$$\dot{e}(t) = Me(t) \tag{2.6.10}$$

If all the eigenvalues in M are stable, then $e(t)$ will approach zero asymptotically [98]. The key step in solving UIO parameters lies in (2.6.11) [102].

$$(I - HE^T)B_d = 0 \tag{2.6.11}$$

It has been revealed that there exists a solution for H in (2.6.11) if and only if $rank(E^TB_d) = rank(B_d)$ [109].

2.6.3 Reduced-Order Thermal Observer

If one or more state variables can be measured or observed directly, the system only requires an observer that has a lower order than the plant. This approach results in the so-called reduced-order observer. In the real application of thermal state observers, some of the system states are not measurable. In this case, the estimation of the unmeasurable system states is often needed [110]. In addition to having lower dimension, the reduced order observer may exhibit performance superior to that of a full-order observer, particular in a closed-loop control system [111].

The block diagram of reduced-order observer is given in Figure 2.24.

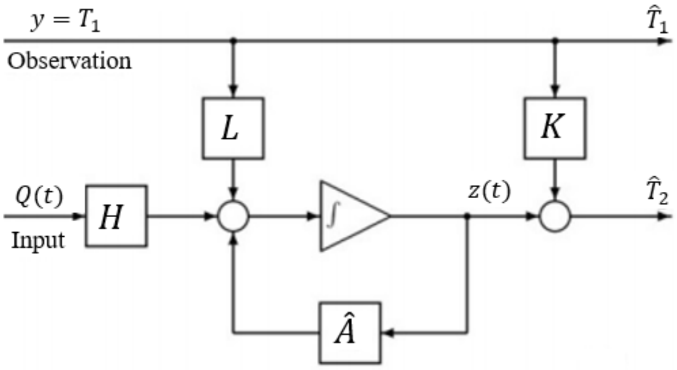

Figure 2.24 Block diagram of reduced-order observer [110].

Where

- $\hat{T}(t)$: The estimated states of the thermal system.
- $\hat{A}, L, H, K$: The matrices to be designed for reduced-order observation.

The theory of reduced-order observers is simplified by partitioning the state vector into two substates as follows

$$\begin{bmatrix} \dot{T}_1(t) \\ \dot{T}_2(t) \end{bmatrix} = \begin{bmatrix} A_{11} & A_{12} \\ A_{21} & A_{22} \end{bmatrix} \begin{bmatrix} T_1(t) \\ T_2(t) \end{bmatrix} + \begin{bmatrix} B_1 \\ B_2 \end{bmatrix} Q(t)$$

$$y(t) = [I \quad 0] \cdot \dot{T}_1(t) \tag{2.6.12}$$

Where

- $T_1(t)$: The state vectors can be measured directly (of dimension w).
- $T_2(t)$: The state vectors need be estimated (of dimension $n - w$).
- A_{11}, A_{12}, A_{21} and A_{22}: $w \times w$, $w \times (n - w)$, $(n - w) \times n$, $(n - w) \times (n - w)$ constant matrices respectively.
- I: Identification matrix of dimension w.

It can be seen in Figure 2.24 that the system output $y(t)$ is assumed as measured state vectors $T_1(t)$. This assumption is not necessary but it can make the derivation of reduced-order observer clear [111].

In terms of $T_1(t)$ and $T_2(t)$ can be obtained from equation (2.6.12) as follows

$$\dot{T}_1(t) = A_{11}T_1(t) + A_{12}T_2(t) + B_1Q(t)$$
$$\dot{T}_2(t) = A_{21}T_1(t) + A_{22}T_2(t) + B_2Q(t) \tag{2.6.13}$$

Since $T_1(t)$ is directed measured, no observer is required for $T_1(t)$, i.e.

$$\hat{T}_1(t) = T_1(t) = y \tag{2.6.14}$$

For the estimated state vectors $T_2(t)$, the reduced-order observer can be defined as

$$\hat{T}_2(t) = Ky(t) + z(t) \tag{2.6.15}$$

Where z is the defined state of order $(n - w)$ as follows

$$\dot{z}(t) = \hat{A}z(t) + Ly(t) + HQ(t) \tag{2.6.16}$$

Reduced order observer need to ensure that the error of state estimation is zero, while independent of $T_1(t)$, $T_2(t)$, $Q(t)$ and $y(t)$ [111].

Since there is no error in estimation of $T_1(t)$ because $T_1(t)$ can be measured directly. The state error only exists in the estimate state vector $T_2(t)$ as follows

$$e(t) = T_2(t) - \hat{T}_2(t) \tag{2.6.17}$$

The derivative of state estimation error can be obtained from equation (2.6.13) to (2.6.16) that

$$\begin{aligned}\dot{e}(t) = \hat{A}e(t)&\\ &+\left(A_{21} - KA_{11} + \hat{A}K - L\right)T_1(t)\\ &+\left(A_{22} - KA_{12} - \hat{A}\right)T_2(t)\\ &+(B_2 - KB_1 - H)Q(t)\end{aligned} \tag{2.6.18}$$

Where the reduced-order observer requires that [111]

- $\hat{A} = A_{22} - KA_{12}$
- $L = A_{21} - KA_{11} + \hat{A}K$

- $H = B_2 - KB_1$

The gain matrix K need be chosen to satisfy that the eigenvalues of $\hat{A}$ lie in the left-half plane. Once K is chosen, there is no further freedom in the choice of L and H.

2.6.4 Summary

In general, Luenberger observer have relatively simple design methods that makes them attractive in practical applications [112]. Reduced order observers can be used to reduce the dimensionality of the observer when only a subset of the state variables are of interest for monitoring purposes [113]

UIO techniques can be embedded in the reduced order observer to minimize the effects caused by unknown input vectors [114]. These concepts will be applied to the problem of real-time thermal estimation for online temperature monitoring applied to a power converter in the following chapters.

Chapter 3 Thermal Modelling

3.1 Introduction

In this chapter, thermal modelling methods reviewed in Chapter 2, will be further developed. The developed modelling methods are geometry-based and will use FDM to describe the conductive thermal problem, and the convective heat transfer.

A 3D finite difference thermal model of power modules will be obtained in this chapter. Additionally, a numerical modelling of convective heat transfer based on an equivalent local heat transfer coefficient will be derived.

The geometry-based numerical thermal modelling and numerical modelling of convective heat transfer are based on a fine-mesh spatial discretization, resulting in a large computational load. While in the following chapters methods for model order reduction will be presented, in this chapter, simplified lumped parameters models, which can be used in online observers, will be introduced, together with method for parameters extraction.

3.2 Numerical Modelling of thermal conduction for Power Modules

The numerical model of thermal conduction will be introduced with reference to a typical power module assembly as illustrated in Figure 3.1. A rectangular N-layer (N=7) geometry with an arbitrary numbers of heat sources is considered.

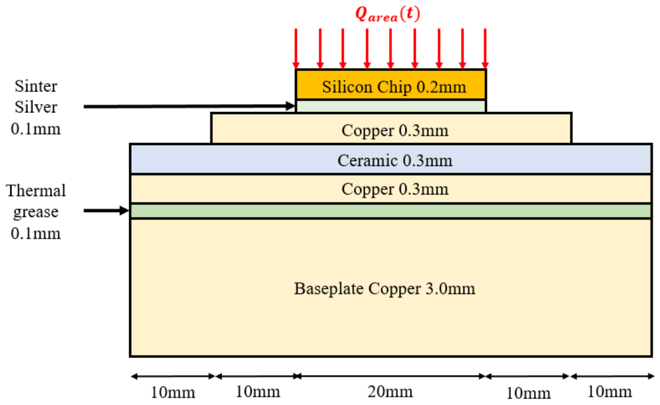

Figure 3.1 Cut view of the simplified model.

The thermal properties of the materials used in the analysed device are given in Table 3.1

Table 3.1 Properties of module materials

	Thermal conductivity $[W/(m \cdot K)]$	Density $[kg/m^3]$	Specific heat $[J/(kg \cdot K)]$
Silicon Carbide	120	3210	750
Sinter Silver	429	10500	235
Copper	400	8933	385
Ceramic	16	2400	691
Thermal Grease	6.5	2350	167

The heat flux $Q(t)$ is assumed to be distributed in the first layer uniformly. The heat flux $Q_{area}(t) = 2 \times 10^6 W/m^2$ changes instantaneously from zero for $t < 0$ and $2 \times 10^6 W/m^2$ for $t \geq 0$.

Thermal analysis and heat equations via FDM can be summarized in the following steps:

- Simplified the completed module in physical level, i.e. neglecting thermal insulating materials such as the silicone gel typically used for passivation on the top surface of power modules.
- Divide the simplified model in cubes with the 3D coordinates (m, n, p), as shown in Figure 3.2.
- Model the heat transfer in each discretized cube with a thermal capacitance $C_{th}(m, n, p)$ representing how much heat can be stored in the cube, thermal resistances $R_{th}(m, n, p)$ that represent the thermal resistances between the cube and its neighbours, and a heat source $q_{loss}\ (m, n, p, t)$ representing power loss dissipation within the single solid medium.

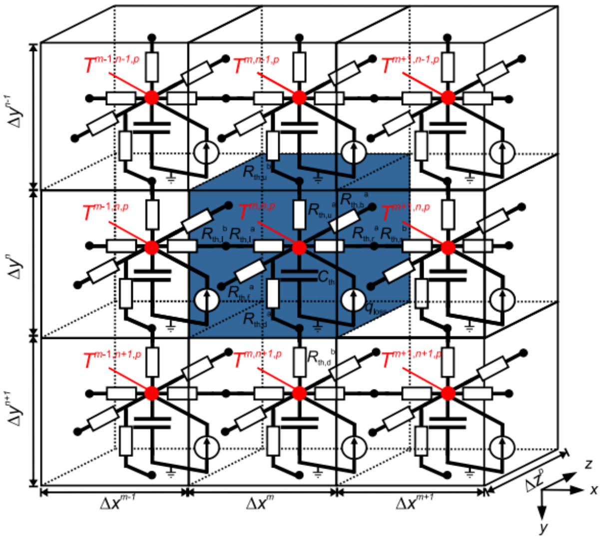

Figure 3.2 3-D Thermal model via FDM [57].

The model is discretized in x-, y- and z-axis. By way of example, for the module under investigation, the discretization used in the full-order model results in a system with 5879 nodes, and the number of input is 9, corresponding to 9 nodes representing the input power source on the silicon chip.

Heat transfer equations can be used to characterize the heat conduction paths as follows

$$\frac{\partial}{\partial t}T(\vec{x}, t) - \frac{k_{th}}{c_p\rho}\Delta T(\vec{x}, t) = \frac{\dot{q}(\vec{x}, t)}{c_p\rho} \tag{3.2.1}$$

Where

- $T(\vec{x}, t)$: The temperature of the coordinate $\vec{x}(t)$ at the time t [°C].

- $\dot{q}(\vec{x},t) = q_{loss}(\vec{x},t)/V$: The internal heat energy per unit volume $[W/m^3]$.
- $q_{loss}(\vec{x},t)$: The power loss of the coordinate $\vec{x}(t)$ at the time t $[W]$.
- V: Volume the cubes $[m^3]$.
- c_p: Specific heat capacity $[J/(K \cdot kg)]$.
- ρ: Density $[kg/m^3]$.
- k_{th}: The thermal conductivity $[W/(m \cdot K)]$.

This PDE can be numerically solved on the discretized geometry resulting in:

$$\begin{aligned} C_{th}^{m,n,p}\frac{dT(m,n,p)}{dt} &= -\sum_{i=1}^{b}\frac{T(m,n,p)}{R_{th,i}^{m,n,p}} + \frac{T(m-1,n,p)}{R_{th,l}^{m,n,p}} \\ &+ \frac{T(m+1,n,p)}{R_{th,r}^{m,n,p}} + \frac{T(m,n-1,p)}{R_{th,u}^{m,n,p}} + \frac{T(m,n+1,p)}{R_{th,d}^{m,n,p}} \\ &+ \frac{T(m,n,p-1)}{R_{th,f}^{m,n,p}} + \frac{T(m,n,p+1)}{R_{th,b}^{m,n,p}} + q_{loss}^{m,n,p} \end{aligned} \tag{3.2.2}$$

The left-hand expression in (3.2.2) represents the changing rate of the temperature in each cube $T(m,n,p)$, and the right-hand expression describes the difference between the losses generated inside the cubes $q_{loss}^{m,n,p}$ and the heat fluxes towards the neighbouring cubes [57]. The parameters of the equation (3.2.2) are the thermal capacitances $C_{th}^{m,n,p}$, which can be calculated using the equation (3.2.3) and the thermal resistances connecting one cube to its neighbours $R_{th,x}^{m,n,p}$. Note that the index x of $R_{th,x}^{m,n,p}$ refers to the directions of the heat conduction paths summarized in the nomenclature [57].

$$C_{th}^{m,n,p} = \Delta x^m \Delta y^n \Delta z^p c_\rho^{m,n,p} \rho^{m,n,p} \tag{3.2.3}$$

$$R_{th,r}^{m,n,p} = \frac{\Delta x^m}{2 \cdot k_{th}^{m,n,p} \Delta y^n \Delta z^p} + \frac{\Delta x^{m+1}}{2 \cdot k_{th}^{m+1,n,p} \Delta y^n \Delta z^p} \tag{3.2.4}$$

The definition of the resistance of one node to its right neighbour is given as an example in (3.2.4) [57]. It takes into account the thermal resistance of the cube itself and of the neighbour node to its right [57]. The resistance in all other directions is calculated analogously. An excerpt of the equivalent circuit, which represents the full-finite-difference conduction model of one node and its neighbours, is depicted in Figure 3.2.

To solve the heat equations for the module considered in this section, boundary conditions are required on the top layer, between layers of different materials and at bottom of modules, will be analysed respectively in the following sections.

3.2.1 Heat Equations on Top Layer

The top layer of the module corresponds to the heat flux $Q_{area}(t)$ generated from the power dissipation. Cut view of the simplified model on the top of silicon chip can be seen in Figure 3.3.

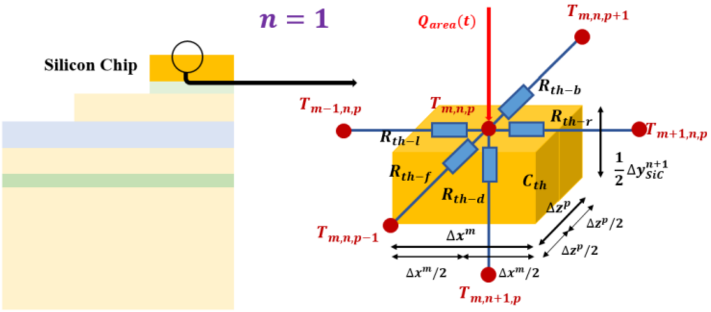

Figure 3.3 Cut view of the simplified model on the top of silicon chip

In Figure 3.3, $n = 1$ for the top of silicon chip where a heat flux Q_{area} is presented. There is no heat exchange on the top of the nodes $T(m, n, p)$ due to the fact that the silicone of silicon chip can be considered as an insulator.

Equation (3.2.2) can thus be written as

$$\begin{aligned} C_{th}^{m,n,p}\frac{dT(m,n,p)}{dt} \quad &= Q_{area}\Delta x^m \Delta z^p - \sum_{i=1}^{b}\frac{T(m,n,p)}{R_{th,i}^{m,n,p}} \\ &+ \frac{T(m-1,n,p)}{R_{th,l}^{m,n,p}} + \frac{T(m+1,n,p)}{R_{th,r}^{m,n,p}} \\ &+ \frac{T(m,n,p-1)}{R_{th,f}^{m,n,p}} + \frac{T(m,n,p+1)}{R_{th,b}^{m,n,p}} \\ &+ \frac{T(m,n+1,p)}{R_{th,d}^{m,n,p}} \end{aligned} \tag{3.2.5}$$

The thermal parameters of equation (3.2.5) can be calculated as

$$\begin{aligned}
C_{th}^{m,n,p} &= \frac{1}{2}\Delta x^m \Delta y_{SiC}^{n+1} \Delta z^p c_\rho^{SiC} \rho^{SiC} \\
R_{th,l}^{m,n,p} &= \frac{\Delta x^m}{2k_{th}^{SiC} A_l} & R_{th,r}^{m,n,p} &= \frac{\Delta x^m}{2k_{th}^{SiC} A_r} \\
R_{th,f}^{m,n,p} &= \frac{\Delta z^p}{2k_{th}^{SiC} A_f} & R_{th,b}^{m,n,p} &= \frac{\Delta z^p}{2k_{th}^{SiC} A_b} \\
R_{th,d}^{m,n,p} &= \frac{\Delta y_{Cu}^{n+1}}{2k_{th}^{SiC} A_d}
\end{aligned} \tag{3.2.6}$$

Where

- $A_l = A_r = \frac{1}{2}\Delta y_{SiC}^{n+1}\Delta z^p$
- $A_f = A_b = \frac{1}{2}\Delta x^m \Delta y_{SiC}^{n+1}$
- $A_d = \Delta x^m \Delta z^p$

3.2.2 Heat Equations on Bottom Layer

In this simplified case, the copper base plate has a convective boundary condition on the bottom layer, which is modelled by a constant heat transfer coefficient $h = 1.2 \times 10^4 W/(m^2K)$ and the inlet air temperature $T_{air} = 0°C$.

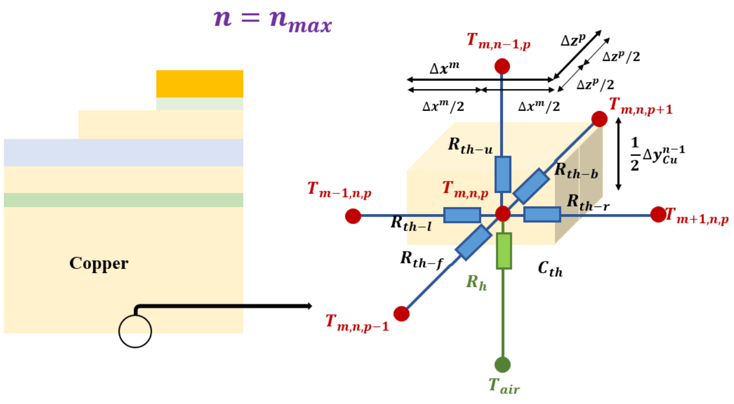

Figure 3.4 Cut view of the simplified model on the bottom of copper baseplate

Figure 3.4 shows the cut view of the simplified model on the bottom of copper baseplate. In Figure 3.4, $n = n_{max}$ for the bottom of copper baseplate where convective boundary condition is presented. There is no conductive thermal resistance below the nodes $T(m, n, p)$ and it is replaced with convective thermal resistance $R_h^{m,n,p}$ to the cooling air.

Without input power, equation (3.2.2) can thus be written as follows

$$\begin{aligned} C_{th}^{m,n,p}\frac{dT(m,n,p)}{dt} &= \sum_{i=1}^{b}\frac{T(m,n,p)}{R_{th,i}^{m,n,p}} + \frac{T_{air}}{R_h^{m,n,p}} \\ &+ \frac{T(m-1,n,p)}{R_{th,l}^{m,n,p}} + \frac{T(m+1,n,p)}{R_{th,r}^{m,n,p}} \\ &+ \frac{T(m,n,p-1)}{R_{th,f}^{m,n,p}} + \frac{T(m,n,p+1)}{R_{th,b}^{m,n,p}} \end{aligned} \tag{3.2.7}$$

The thermal parameters of equation (3.2.7) can be calculated as

$$\begin{aligned} &C_{th}^{m,n,p} = \frac{1}{2}\Delta x^m \Delta y_{Cu}^{n-1} \Delta z^p c_\rho^{SiC} \rho^{SiC} \\ &R_{th,l}^{m,n,p} = \frac{\Delta x^m}{2k_{th}^{Cu} A_l} \qquad && R_{th,r}^{m,n,p} = \frac{\Delta x^m}{2k_{th}^{Cu} A_r} \\ &R_{th,f}^{m,n,p} = \frac{\Delta z^p}{2k_{th}^{Cu} A_f} && R_{th,b}^{m,n,p} = \frac{\Delta z^p}{2k_{th}^{Cu} A_b} \\ &R_{th,u}^{m,n,p} = \frac{\Delta y_{Ag}^{n-1}}{2k_{th}^{Cu} A_u} && R_h^{m,n,p} = \frac{1}{h^{m,p} A_d} \end{aligned} \tag{3.2.8}$$

Where

- $A_l = A_r = \frac{1}{2}\Delta y_{Cu}^{n-1}\Delta z^p$
- $A_f = A_b = \frac{1}{2}\Delta x^m \Delta y_{Cu}^{n-1}$
- $A_u = A_d = \Delta x^m \Delta z^p$
- $h^{m,p}$: Local heat transfer coefficients on the bottom baseplate.

3.2.3 Heat Equations through Different Layers

The completed module in physical level is simplified and divided in small cubes with the 3D coordinates. However, due to the different thicknesses and materials of layers, e.g. the temperature nodes located at the interface between sinter silver and copper shown in Figure 3.1, simplified cubes are not always accurate to address the mesh unit. The geometry shown in Figure 3.5 supplies as an example.

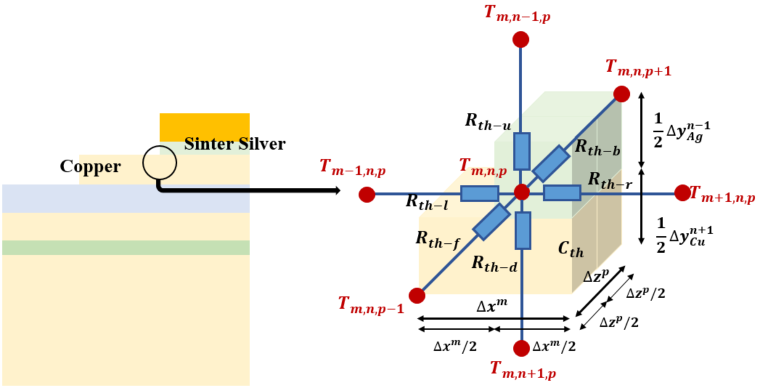

Figure 3.5 Cut view of the simplified model through sinter silver and copper

Without input power, equation (3.2.2) can be written as follows

$$C_{th}^{m,n,p}\frac{dT(m,n,p)}{dt} = -\sum_{i=1}^{b}\frac{T(m,n,p)}{R_{th,i}^{m,n,p}} + \frac{T(m-1,n,p)}{R_{th,l}^{m,n,p}} + \frac{T(m+1,n,p)}{R_{th,r}^{m,n,p}} + \frac{T(m,n-1,p)}{R_{th,u}^{m,n,p}} + \frac{T(m,n+1,p)}{R_{th,d}^{m,n,p}} + \frac{T(m,n,p-1)}{R_{th,f}^{m,n,p}} + \frac{T(m,n,p+1)}{R_{th,b}^{m,n,p}} \tag{3.2.9}$$

Where

$$C_{th}^{m,n,p} = c_\rho^{Ag}\rho^{Ag}A_u + c_\rho^{Cu}\rho^{Cu}A_d$$

$$R_{th,l}^{m,n,p} = \frac{\Delta x^m}{2k_{th}^{l}A_l} \qquad R_{th,r}^{m,n,p} = \frac{\Delta x^m}{2k_{th}^{r}A_r}$$

$$R_{th,u}^{m,n,p} = \frac{\Delta y_{Ag}^{n-1}}{2k_{th}^{u}A_u} \qquad R_{th,d}^{m,n,p} = \frac{\Delta y_{Cu}^{n+1}}{2k_{th}^{d}A_d}$$

$$R_{th,f}^{m,n,p}=\frac{\Delta z^{p}}{2k_{th}^{f}A_{f}} \qquad R_{th,b}^{m,n,p}=\frac{\Delta z^{p}}{2k_{th}^{b}A_{b}} \tag{3.2.10}$$

The interface thermal conductivities and cross area for the calculation of thermal resistances can be expressed in Table 3.2.

Table 3.2. Thermal parameters of sinter silver and copper interface

Conductivity		Cross-Section Area	
k_{th}^{l}	k_{Cu}	A_l	$\frac{1}{2}\Delta y_{Ag}^{n-1}\Delta z^{p}$
k_{th}^{r}	$\frac{(k_{Ag}\Delta y_{Ag}^{n-1}+k_{Cu}\Delta y_{Ag}^{n-1})}{(\Delta y_{Ag}^{n-1}+\Delta y_{Cu}^{n+1})}$	A_r	$\frac{1}{2}(\Delta y_{Ag}^{n-1}+\Delta y_{Cu}^{n+1})\Delta z^{p}$
k_{th}^{u}	k_{Ag}	A_u	$\frac{1}{2}\Delta x^{m}\Delta z^{p}$
k_{th}^{d}	k_{Cu}	A_d	$\Delta x^{m}\Delta z^{p}$
k_{th}^{f}	$\frac{(k_{Ag}\Delta y_{Ag}^{n-1}+2k_{Cu}\Delta y_{Ag}^{n-1})}{(\Delta y_{Ag}^{n-1}+2\Delta y_{Ag}^{n-1})}$	A_f	$\frac{1}{4}\Delta x^{m}\Delta y_{Ag}^{n-1}+\frac{1}{2}\Delta x^{m}\Delta y_{Cu}^{n+1}$
k_{th}^{b}	$\frac{(k_{Ag}\Delta y_{Ag}^{n-1}+2k_{Cu}\Delta y_{Ag}^{n-1})}{(\Delta y_{Ag}^{n-1}+2\Delta y_{Ag}^{n-1})}$	A_b	$\frac{1}{4}\Delta x^{m}\Delta y_{Ag}^{n-1}+\frac{1}{2}\Delta x^{m}\Delta y_{Cu}^{n+1}$

It is worth noting that other mesh units with non-cube geometry, including the non-cube mesh units on the top and bottom boundary conditions, can be analysed using similar methods.

3.2.4 Validation of Numerical Conductive Thermal Modelling

In this section, the developed numerical convective thermal modelling method via FDM is validated against commercial software ANSYS mechanical.

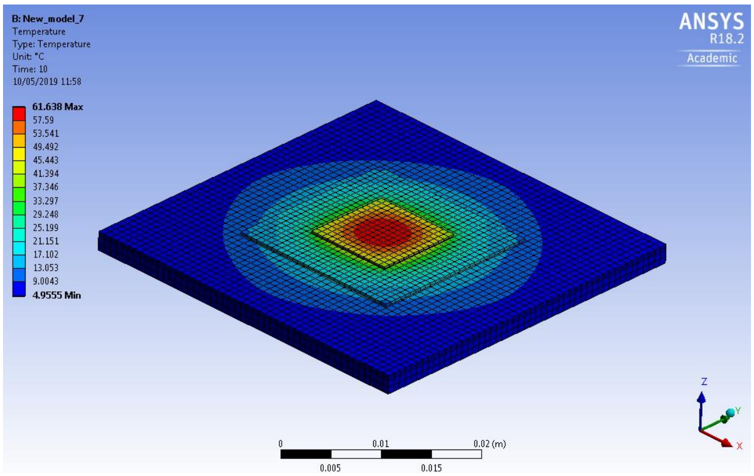

Figure 3.6 Steady-state temperature distribution from ANSYS Mechanical

The 3D geometry structure is designed following Figure 3.1. The 3D geometry structure and steady-state temperature distribution from ANSYS mechanical can be seen in Figure 3.6.

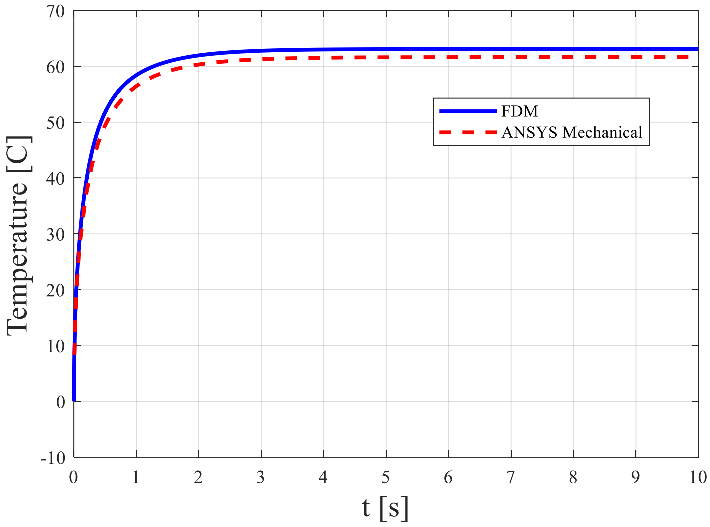

Figure 3.7 Comparison of transient temperature distribution from FDM and ANSYS

Figure 3.7 shows the transient response of the MOSFET temperature from FDM numerical model and ANSYS Mechanical model.

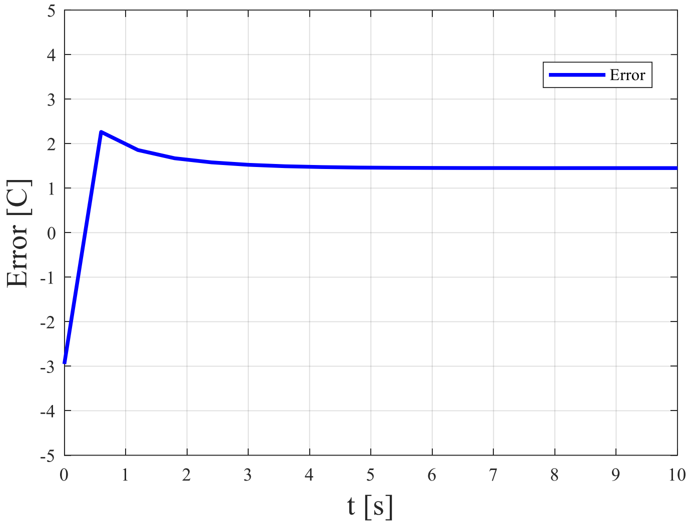

Figure 3.8 Error of transient temperature distribution between FDM and ANSYS

Figure 3.8 illustrates the transient temperature error between FDM and ANSYS, which is less than 3.5%. It can be seen that the transient thermal response of the FDM numerical method can match the transient data from commercial software ANSYS mechanical.

3.3 Numerical Convective Thermal Modelling for Cooling System

In section 3.2.2, local heat transfer coefficient $h^{m,p}$ is introduced in the conductive thermal modelling. $h^{m,p}$ is a function of the location (m, p) on the baseplate. Unfortunately, the calculation of heat transfer coefficients is not straightforward when heatsinks are considered.

The goal of this section is thus to develop a numerical convective thermal model of a parallel-plate heatsink taking into account its geometry and the air mass flow rate. The model will result in an equivalent heat transfer coefficient $h^{m,p}$ that is variable with the axial position along the bottom baseplate of power modules.

3.3.1 Thermal Modelling of Heatsink-Fan Cooling System

Many cooling systems can be used to handle power losses in power converters [115]. The most common cooling system is typically based on the parallel-plate fin design. This might be preferred when the additional complexity associated with liquid cooling solutions due to pipes, pumps, coolants and coolant-air heat exchangers) is undesirable due to cost, efficiency, reliability or overall system weight [116].

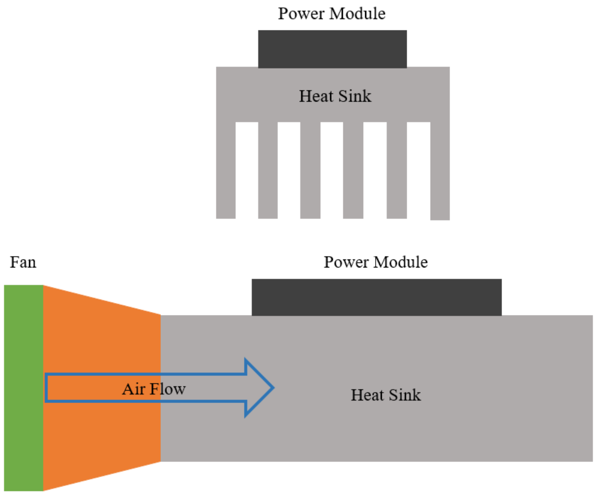

Figure 3.9 Geometric configuration of heatsink, fan and duct.

The geometry configuration of fan-cooled heat sink cooling system is shown in Figure 3.9, and the details of plate-fin heatsink is shown in Figure 3.10.

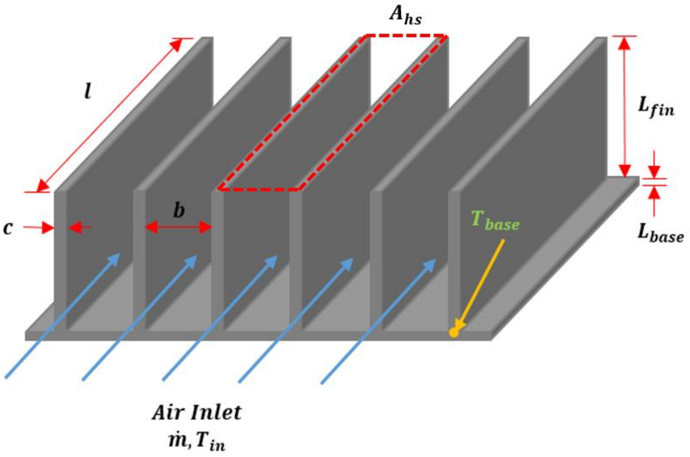

Figure 3.10 Air-forced plate-fin heatsink

Where

- L : Heat sink length $[m]$.
- L_{fin} : Height of fins $[m]$.
- L_{base} : Baseplate thickness $[m]$.
- b : Heat sink channel spacing $[m]$.
- c : Heat sink fin thickness $[m]$.
- A_{hs} : Heat sink base plate area $[m^2]$.
- $\dot{m}$: Mass flow rate of air $[kg/s]$.
- T_{in} : Inlet air temperature [°C].
- T_{base} : Baseplate temperature [°C].
- n : Number of channels $[R]$.

The thermal modelling of a fan-cooled heat sink is a multi-physics problem, including heat conduction in solids, convective heat and mass transfer, and fluid dynamics [117].

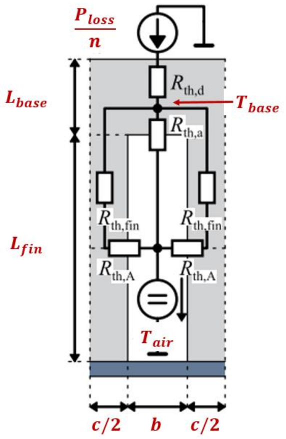

Figure 3.11 Thermal equivalent circuit of heat sink

In Figure 3.11, the equivalent circuit of thermal resistance given with

- $R_{th,d}$: Thermal resistance of base plate $[K/W]$.
- $R_{th,fin}$: Thermal resistance of fin $[K/W]$.
- $R_{th,A}$: Thermal resistance of fin to air $[K/W]$.
- $R_{th,a}$: Thermal resistance of base plate to air $[K/W]$.
- T_{air} : Temperature of air in the heat sink channel [℃].

The overall thermal resistance of the total finned surface from the fundamental heat transfer [118] is written as

$$\begin{aligned} R_{total} &= R_{th,d} + \frac{1}{n}\frac{\left(R_{th,fin} + R_{th,A}\right)R_{th,a}}{R_{th,fin} + R_{th,A} + 2R_{th,a}} \\ &= R_{th,d} + R_{th,conv} \end{aligned} \tag{3.3.1}$$

$R_{th,d}$ can be expressed as the following function of the heat sink geometry and the heat sink material's thermal conductivity

$$R_{th,d} = \frac{L_{base}}{k_{hs}A_{hs}} \tag{3.3.2}$$

Where

- L_{base} : Baseplate thickness $[m]$.
- A_{hs} : Heat sink base plate area $[m^2]$.
- k_{hs} : The thermal conductivity of heat sink material $[W/(m \cdot K)]$.

$R_{th,conv}$ is the overall resistance due to the convective process, which depends on the volume flow, the geometry, and the position along the longitudinal axis of the channel [117]. As is shown in equation (3.3.1), $R_{th,conv}$ can be obtained by the sum of $R_{th,fin}$, $R_{th,A}$, and $R_{th,a}$. Unfortunately, the evaluation of $R_{th,conv}$ is not simple. Here a model based on the single fluid heat exchanger model [119], as shown in Figure 3.12, will be developed.

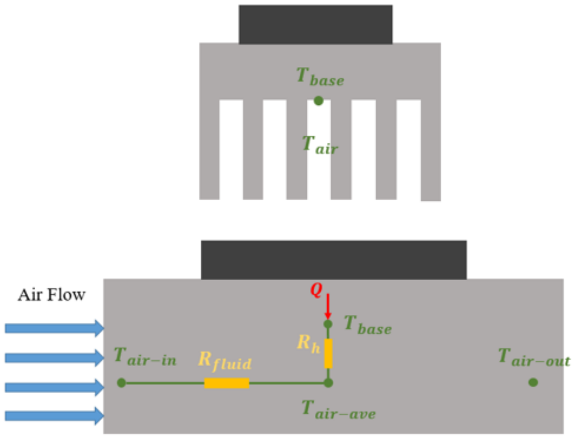

Figure 3.12 The single fluid heat exchanger model

Where

- R_h : The convective thermal resistance $[K/W]$.
- R_{fluid} : The fluid resistance $[K/W]$.
- $T_{air,in}$: Inlet air temperature of heatsink [°C].
- $T_{air,ave}$: Average air temperature in the middle of heatsink [°C].
- $T_{air,out}$: Output air temperature of heatsink [°C].

The convective thermal resistance R_h can be calculated from convection heat transfer and heat transfer coefficient h is used to model the convection heat transfer as following

$$Q = hA_{eff}(T_{base} - T_{air,ave}) \tag{3.3.3}$$

Where

- h: Convection heat transfer coefficient $[W/(m^2K)]$.
- A_{eff}: Effective heat transfer surface area $[m^2]$.
- T_{base}: Temperature of the base plate surface [°C].
- $T_{air,ave}$: Average air temperature in the middle of heatsink [°C].

The convective thermal resistance R_h is thus obtained as

$$R_h = \frac{T_{base} - T_{air,ave}}{Q} = \frac{1}{hA_{eff}} \tag{3.3.4}$$

The fluid resistance R_{fluid} can be derived in terms of the change in air temperature within the heat sink as follows

$$\frac{Q}{2\dot{m}c_{air}} = (T_{air,ave} - T_{air,in}) \tag{3.3.5}$$

Where

- $\dot{m}$: Mass flow rate $[kg/s]$.
- c_{air} : Specific heat capacity of air $1.01e^3$ $[J/(kg \cdot K)]$.

The convective thermal resistance R_h is thus obtained as

$$R_{fluid} = \frac{T_{air,ave} - T_{air,in}}{Q} = \frac{1}{2\dot{m}c_{air}} \tag{3.3.6}$$

The overall resistance due to the convective process can be thus expressed as follows [120] [121]:

$$R_{th,conv} = \frac{2 \cdot R_{fluid}}{1 - e^{-2 \cdot \frac{R_{fluid}}{R_h}}} \tag{3.3.7}$$

It should be noted that the heated surface has been treated as isothermal and the model presented in (3.3.7) is only true for an isoflux surface. The overall resistance due to the convective process $R_{th,conv}$ can thus be obtained as follows

$$R_{th,conv} = \frac{2 \cdot R_{fluid}}{1 - e^{-2 \cdot \frac{R_{fluid}}{R_h}}} = \left[\dot{m}c_{air}\left(1 - e^{-\frac{hA_{eff}}{\dot{m}c_{air}}}\right)\right]^{-1} \tag{3.3.8}$$

Effective heat transfer surface area A_{eff} and fin efficiency η can be expressed as follows

$$A_{eff} = n\left(2L_{fin}\eta + b\right)L \tag{3.3.9}$$

$$\eta = \frac{tanh\left(\sqrt{\frac{2h(c+L)}{k_{hs}tL}} \cdot L_{fin}\right)}{\sqrt{\frac{2h(c+L)}{k_{hs}cL}} \cdot L_{fin}} \tag{3.3.10}$$

It can be seen that the convective thermal modelling of heatsink-fan thermal modelling relies on the heat transfer coefficient h, which is a function of Nusselt number [122]. The Nusselt number is the ratio of convection to conduction across the convective boundary, including dimensionless local Nusselt number and non-dimensionalized Nusselt number. The non-dimensionalized Nusselt number can be expressed as follows:

$$N_{u\mathcal{L}} = \frac{h}{k_{fluid}/\mathcal{L}} \tag{3.3.11}$$

Where

- h: The convective heat transfer coefficient of the flow $[W/(m^2K)]$.
- $\mathcal{L}$: The characteristic length $[m]$
- k_{fluid}: The thermal conductivity of the fluid $[W/(m \cdot K)]$.

The derivation of Nusselt number will be shown in the Section 3.3.2 and 3.3.3.

3.3.2 Channel Geometry and Length of Heatsink-Fan Cooling System

Before going into details of the Nusselt number, the characteristic length $\mathcal{L}$ of the heatsink in equation (3.3.11), should be adequately discussed. The characteristic length in [123] [124] has been chosen as follows

$$\mathcal{L} = 4A/P_{flow} \tag{3.3.12}$$

Where

- A: The area of air flow $[m^2]$.
- P_{flow}: The perimeter of air flow $[m]$.

The main flow type in the air duct of heatsink is laminar flow. Laminar fluid friction and heat transfer in non-circular pipes often occur in low Reynolds number flow heat exchangers, such as automotive coolers, cold plates and microchannel radiators [125]. However, in some references, the use of equation (3.3.12) in laminar flow is questioned [126]. It has been shown by Muzychka and Yovanovich [127] [128] that $\mathcal{L} = \sqrt{A}$ succeeds in considering the problems of laminar flow in mathematical physics.

In the case of the length or axial position of dimensionless duct length, dimensionless duct length L^+ and dimensionless axial coordinate z^+ can be introduced using a length scale $\mathcal{L} = \sqrt{A}$ to give [129-133]

$$L^+ = \frac{\frac{L}{\sqrt{A}}}{Re_{\sqrt{A}}} = \frac{\mu \cdot L}{\dot{m}} \tag{3.3.13}$$

$$z^+ = \frac{z/\sqrt{A}}{Re_{\sqrt{A}}} = \frac{\mu \cdot z}{\dot{m}} \tag{3.3.14}$$

Where

- L: Duct length of heatsinks $[m]$.
- L^+: Dimensionless duct length $[R]$.
- z: Axial coordinate of heatsink ducts $[m]$.
- z^*: Dimensionless axial coordinate of heatsink ducts $[R]$.
- $Re_{\sqrt{A}}$: Reynolds number based on $\mathcal{L} = \sqrt{A}$ $[R]$.
- μ: The dynamic viscosity of air $[kg/(m \cdot s)]$.

Similarly, dimensionless thermal length L^* and dimensionless position z^* can be calculated as follows

$$L^* = \frac{\frac{L}{\sqrt{A}}}{Pe_{\sqrt{A}}} = \frac{\mu \cdot L}{\dot{m}Pr} \tag{3.3.15}$$

$$z^* = \frac{z/\sqrt{A}}{Pe_{\sqrt{A}}} = \frac{\mu \cdot z}{\dot{m}Pr} \tag{3.3.16}$$

Where

- L^*: Dimensionless thermal length $[R]$.
- z^*: Dimensionless position for thermally developing flow of heatsink ducts $[R]$.
- $Pe_{\sqrt{A}} = w_{ave}\mathcal{L}/\alpha$: Peclet number based on $\mathcal{L} = \sqrt{A}$ $[R]$.
- w_{ave}: Average velocity of air flow $[m/s]$.
- α: Thermal diffusivity $[m^2/s]$.
- Pr: Prandtl number (0.71 for air) [R].

3.3.3 Pressure Drop Models and Heat Transfer Models of Heatsink-Fan Cooling System

The pressure loss through heatsink ducts is determined by the friction between the fluid and the ducts [134]. A simple model as a function of L^+ is thus necessary for the calculation of friction factor. The model takes the following form [127] [135]:

$$fRe_{\sqrt{A}} = \left[\left(\frac{3.44}{\sqrt{L^+}}\right)^n + \left(fRe_{fd}\right)^n\right]^{1/n} \qquad (3.3.17)$$

Where n is a superposition parameter determined by comparison with experimental data over the full range of L^+. Using the results provided in [127] and the general expression of equation (3.3.17), the following model can be developed:

$$fRe_{\sqrt{A}} = \left[\left(\frac{3.44}{\sqrt{L^+}}\right)^n + \left(\frac{12}{\sqrt{\epsilon}(1+\epsilon)\left[1 - \frac{192\epsilon}{\pi^5}\tanh(\frac{\pi}{2\epsilon})\right]}\right)^n\right]^{1/n} \qquad (3.3.18)$$

Where ϵ is the nominal aspect ratio of heatsink and can be calculated as

$$\epsilon = \frac{fin\ thickness}{channel\ space} = \frac{c}{b} \qquad (3.3.19)$$

Using the available data from [127] and [136], it is found that the value of n lies in the range $1.5 < n < 3.6$ with a mean value $n \approx 2$. Based on the proposed pressure drop model, a heat transfer model for developing flow, which is valid over the entire range of dimensionless duct lengths, has been developed by Muzychka and Yovanovich in [137]. The general form of the proposed model for an arbitrary characteristic length scale is follows.

$$Nu_{\sqrt{A}}(L^*) = \left[\left\{C_2 C_3 \left(\frac{fRe_{\sqrt{A}}}{L^*}\right)^{\frac{1}{3}}\right\}^n + \left\{C_1 \left(\frac{fRe_{\sqrt{A}}}{8\sqrt{\pi}\epsilon^{\gamma}}\right)\right\}^n\right]^{1/n} \qquad (3.3.20)$$

With $n \approx 5$, the model becomes:

$$Nu_{\sqrt{A}}(L^*) = \left[\left\{C_2 C_3 \left(\frac{fRe_{\sqrt{A}}}{L^*}\right)^{\frac{1}{3}}\right\}^5 + \left\{C_1 \left(\frac{fRe_{\sqrt{A}}}{8\sqrt{\pi}\epsilon^{\gamma}}\right)\right\}^5\right]^{1/5} \qquad (3.3.21)$$

Where the constants C_1, C_2, C_3 and γ are given in Table 3.3. These constants define the various cases for local or average Nusselt number and isothermal or isoflux boundary conditions.

Table 3.3 Coefficients C_1, C_2, C_3 and γ

Isothermal	$C_1 = 3.01$	$C_3 = 0.409$
Isoflux	$C_1 = 3.66,$	$C_3 = 0.501$
Local	$C_2 = 3.01$	
Average	$C_2 = 3/2$	
Upper bound	$\gamma = 1/10$	
Lower bound	$\gamma = -3/10$	

The analyses of combined entrance region are related to Prandtl number (P_r). The Prandtl number (P_r) is a dimensionless number, defined as the ratio of momentum diffusivity to thermal diffusivity. The Prandtl number is expressed as

$$P_r = \frac{v}{\alpha} = \frac{\mu/\rho}{k_{th}/(c_{air}\rho)} = \frac{c_{air}\mu}{k_{th}} \tag{3.3.22}$$

Where

- $v = \mu/\rho$: Kinematic viscosity ($2 \times 10^{-5} m^2/s$ for air).
- α: Thermal diffusivity $[m^2/s]$.
- μ: The dynamic viscosity of air $[kg/(m \cdot s)]$.
- ρ: Density ($1.225\ kg/m^3$ for air).
- k_{th}: Thermal conductivity $[W/(m \cdot K)]$.
- c_{air} : Thermal capacitance of air $1.01e^3$ $[J/(kg \cdot K)]$.

With Prandtl number, the characteristics of combined entrance regions can be expressed using the average Nusselt number [137]. The average Nusselt number for both isothermal or isoflux boundary conditions can be compactly written as:

$$Nu_{\mathcal{L}} = \frac{C_4 f(Pr)}{\sqrt{L^*}} \tag{3.3.23}$$

Where C_4 and $f(Pr)$ are given in Table 3.4.

Table 3.4 Coefficients C_4 and $f(Pr)$

Isothermal	$f(Pr) = \frac{0.564}{[1 + (1.664Pr^{1/6})^{9/2}]^{2/9}}$
Isoflux	$f(Pr) = \frac{0.886}{[1 + (1.909Pr^{1/6})^{9/2}]^{2/9}}$
Local	$C_4 = 1$
Average	$C_4 = 2$

A model for the combined entrance region was developed by Muzychka and Yovanovich [137], by combining the solutions for a flat plate, Equation (3.3.21), with the proposed model for the Graetz flow problem, Equation (3.3.23). This model took the form:

$$Nu_{\sqrt{A}}(L^*, Pr) = \left[\left(\left\{C_2 C_3 \left(\frac{fRe_{\sqrt{A}}}{L^*}\right)^{\frac{1}{3}}\right\}^5 + \left\{C_1 \left(\frac{fRe_{\sqrt{A}}}{8\sqrt{\pi}\epsilon^{\gamma}}\right)\right\}^5\right)^{m/5} + \left(\frac{C_4 f(Pr)}{\sqrt{L^*}}\right)^m\right]^{1/m} \tag{3.3.24}$$

The blending parameter m was determined to vary between 2 and 7 for all of the data examined [137]. To provide a better accuracy, the blending parameter can are expressed as

$$m = 2.27 + 1.65Pr^{1/3} \tag{3.3.25}$$

3.3.4 Numerical Forced Convection Modelling of Heat Sinks

After introducing $z^* = L^*$ and constant Pr for air flow, the equation (3.3.24) which represents local Nusselt number, can be written as:

$$Nu_{\sqrt{A}}(z^*) = \left[\left(\left\{C_2 C_3 \left(\frac{fRe_{\sqrt{A}}}{z^*}\right)^{\frac{1}{3}}\right\}^5 + \left\{C_1 \left(\frac{fRe_{\sqrt{A}}}{8\sqrt{\pi}\epsilon^{\gamma}}\right)\right\}^5\right)^{m/5} + \left(\frac{C_4 f(Pr)}{\sqrt{z^*}}\right)^m\right]^{1/m} \tag{3.3.26}$$

With local Nusselt number, the local heat transfer coefficient versus channel length can be expressed as

$$h(z^*) = \frac{Nu_{\sqrt{A}}(z^*)k_{air}}{d_h} \tag{3.3.27}$$

Where

- k_{air}: The thermal conductivity of the air 0.03 $[W/(m \cdot K)]$.
- $d_h = \frac{2bL_{fin}}{b+L_{fin}}$: Hydraulic diameter of the heat sink channel $[m]$.

The convective thermal resistance can be calculated as

$$R_h = \frac{1}{hA_{eff}} \tag{3.3.28}$$

Where

- $A_{eff} = n\left(2L_{fin}\eta + b\right)L$: Effective heat transfer surface area $[m^2]$
- η: The fin efficiency of heatsink $[R]$

It can been seen that the convective thermal resistance R_h is related to the geometry of the heatsink. However, 3D FDM thermal modelling is not suitable to describe such a complex geometry structure like heatsink. Consequently, fins of heat sink cannot be simulated in FDM model can only the baseplate of heatsink with simple cuboid structure can be remained. Then the equivalent heat transfer coefficient h_{equ} need to be estimated as follows

$$\frac{1}{hA_{eff}} = \frac{1}{h_{equ}A_{baseplate}} \tag{3.3.29}$$

Where

- $A_{base} = L \cdot b_{hs}$: The area of heatsink base plate $[m^2]$.
- b_{hs}: The width of heatsink base plate $[m]$.

In the simplified case discussed in Section 3.2.2, the base plate has a convective boundary condition on the bottom layer with constant inlet air temperature T_{air}. It is assumed that the air flows into heatsink channel uniformly in the z-axis direction, as is shown in Figure 3.13.

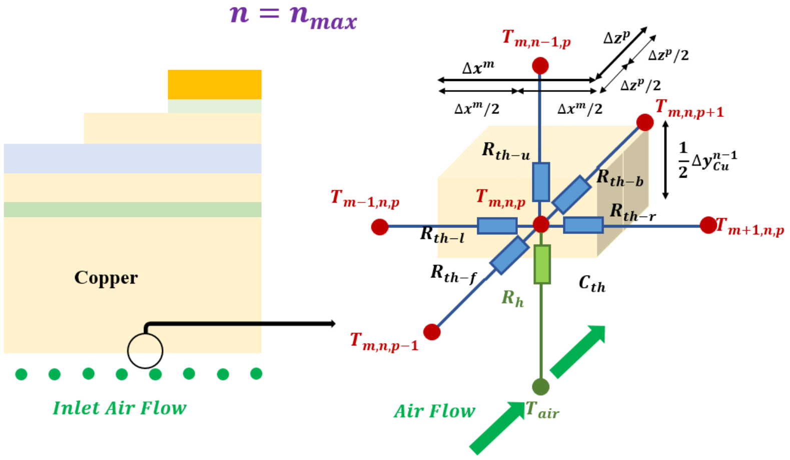

Figure 3.13 Cut view of the simplified model on the bottom of copper baseplate

In Section 3.2.2, the local heat transfer coefficient $h^{m,p}$ is a function of the location $(m, n = n_{max}, p)$ on the baseplate. With uniform inlet air flow, the local heat transfer coefficient is a one-dimensional parameters related to axial position of baseplate along the air flow, which can be represented by $h^{m,p} = h_{equ}(\mathrm{z})$. The $h_{equ}(\mathrm{z})$ can be calculated as follows

$$h_{equ}(z) = \frac{A_{eff}}{A_{baseplate}} h(z) = \frac{A_{eff}}{A_{baseplate}} \frac{Nu_{\sqrt{A}}(z) k_{air}}{d_h} \tag{3.3.30}$$

3.3.5 Validation of Numerical Forced Convection Modelling

The numerical thermal model of local heat transfer coefficient is validated by comparing the junction temperatures of MOSFETs modified from ANSYS Mechanical which rely on the numerical results from numerical heat transfer coefficient model with commercial CFD software. A simplified test model representing system containing a twelve-chip power module and a plate-fin heatsink is shown in Figure 3.14.

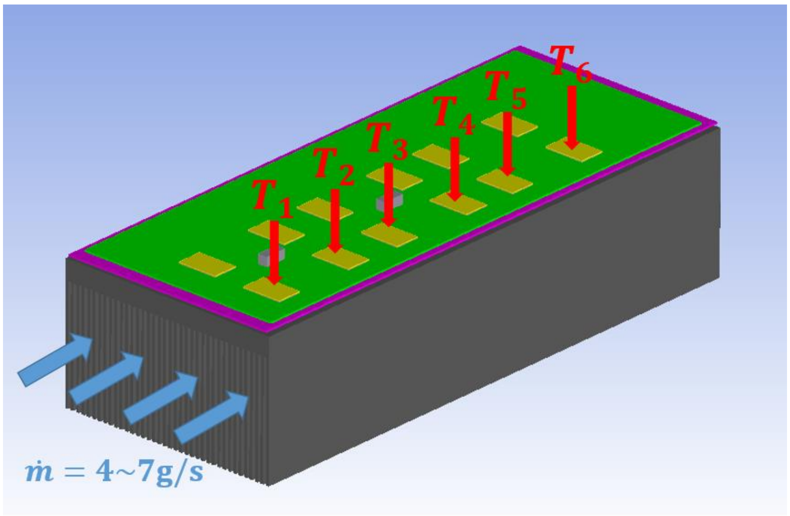

Figure 3.14 Geometry structure of simplified power module with heatsink

The mass flow rate varies from 4g/s to 7g/s and six temperature probes $T_{1\sim6}$ are settled at six MOSFET chips with different axial locations. Both the ANSYS Mechanical model and CFD model used the same power injection ($12.5W \times 12$). The properties of the heatsink is shown in Table 3.5.

Table 3.5 The properties of the heatsink

Parameters		Values
L	Heat sink length $[m]$	0.084
b_{hs}	Heat sink width $[m]$	0.034
L_{fin}	Height of fins $[m]$.	0.02
L_{base}	Baseplate thickness $[m]$.	0.003
n	Number of fins $[R]$.	38
b	Heat sink fin spacing $[m]$.	0.0004
t	Heat sink fin thickness $[m]$.	0.0005
$\dot{m}$	Mass flow rate of air $[g/s]$.	4; 5; 7
T_{in}	Inlet air temperature [℃].	40

The obtained local Nusselt number ($Nu_{\sqrt{A}}$), heat transfer coefficient (h), heatsink efficiency (η) and equivalent heat transfer coefficient (h_{equ}) versus axial duct length can be seen in Figure 3.15.

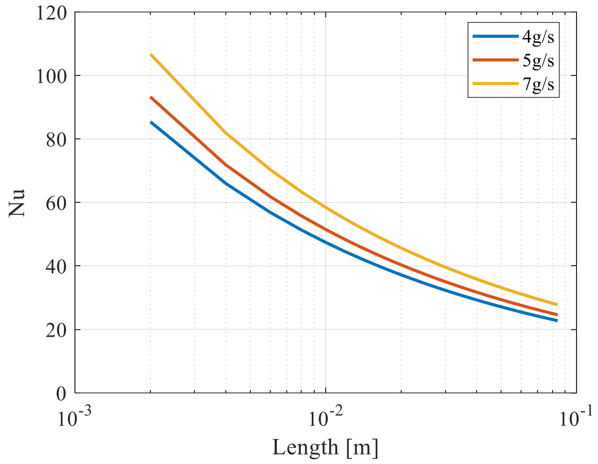

(a) Nusselt number $Nu_{\sqrt{A}}(z)$

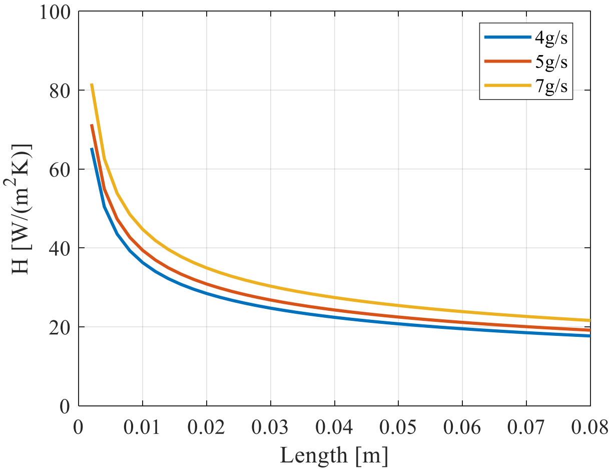

(b) Local heat transfer coefficient $h(z)$

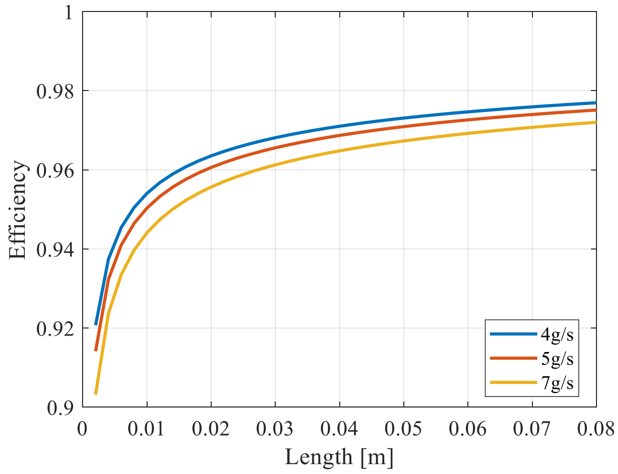

(c) Efficiency of convection $\eta(z)$

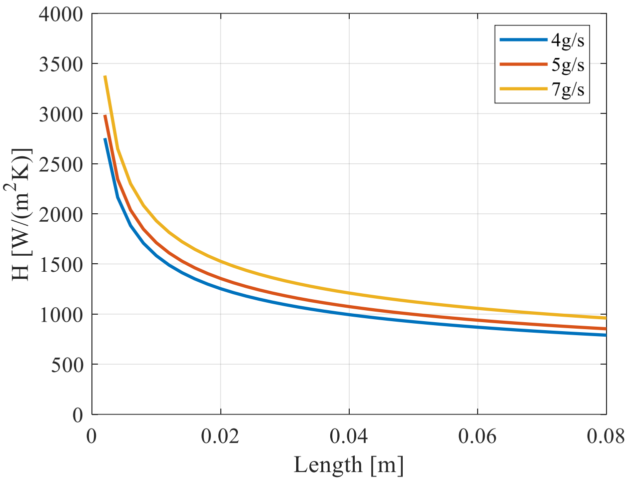

(d) Equivalent heat transfer coefficient $h_{equ}(z)$

Figure 3.15 Local heat transfer coefficients virus z-axial length

The numerical model has been validated against detailed simulation using CFD software ANSYS ICEPAK. The calculated local heat transfer coefficients from numerical convective thermal modelling are used in ANSYS Mechanical model, which keeps the module and heatsink baseplate while removes the fins of heatsink.

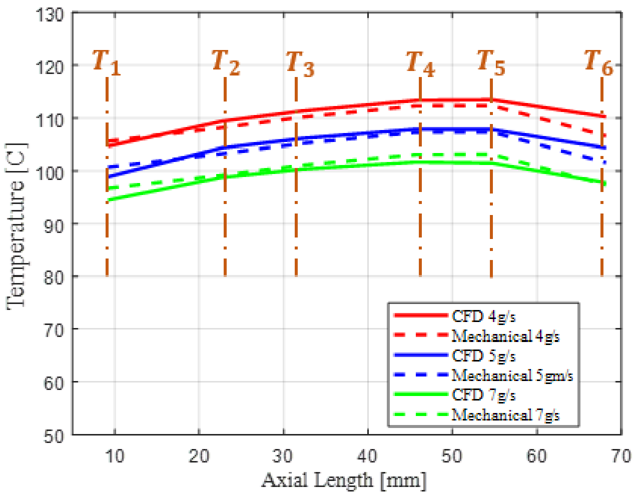

Figure 3.16 Comparison of temperature along the axial direction with the numerical model and detailed CFD analysis

The steady-state results are shown in Figure 3.16. Excellent data agreement can be found between this two methods. The error between CFD and ANSYS Icepak is less than 3%, confirming the accuracy of the numerical convective thermal modelling.

3.4 Lumped Compact Thermal Modelling for Power Electronics System

Although the developed models are capable of accurately modelling the temperature distribution in complex geometries, they still result in computationally complex systems of equations due to the large number of nodes in the discretization. While a detailed model could be suitable at the design stage of a power converter, a compact model might be preferable for online monitoring of temperature during converter operation. This section will develop a simple lumped parameter model which will be used in subsequent chapter for the purpose of temperature monitoring.

3.4.1 Power Module

All the derivations presented here will be developed with reference to a Silicon Carbide (SiC) MOSFET-based half-bridge. Based on innovative wire-bond free planar interconnect technology [138] [139], the module has been designed and manufactured by Siemens AG, within the Horizon2020 European Project - Integrated, Intelligent Modular Power Electronic Converter (I2MPECT) [140], to provide a power electronic building block (PEBB) for a 99% efficient 3-phase power converter with a power-to-weight ratio of 10 kW/kg. This means that for output power of 45 kW, maximum three-phase power loss of 450 W (150 W per phase/leg) is the allowable limit.

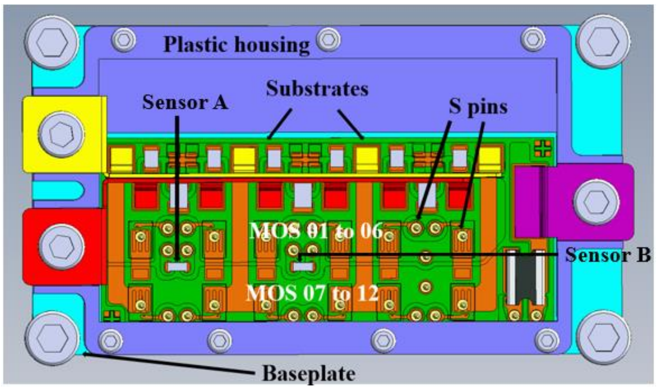

(a) Top view

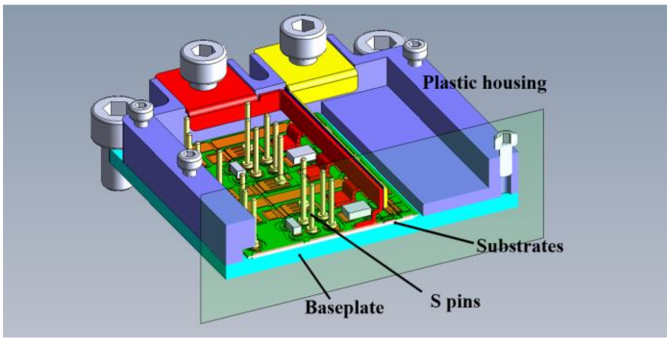

(b) cut iso view

Figure 3.17 Single I2MPECT power module.

Figure 3.17 shows CAD drawings of the half-bridge wirebond-less power module. Twelve MOSFETs are sintered using a silver sintering paste onto the direct copper bonded (DBC) substrate. Two thermistors (PT1000), indicated as Sensors A, B in Figure 3.17, are mounted on the DBC for temperature feedback. The module is primarily cooled via the baseplate, which is designed to be mounted to an air cooled heatsink via a thermal interface material (TIM). This configuration can be shown in a cross-section picture as Figure 3.18.

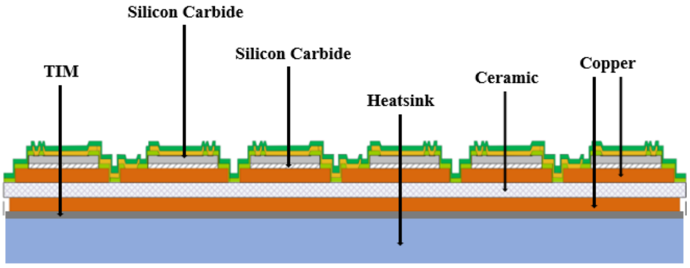

Figure 3.18 Cross-section view (including TIM and heatsink baseplate)

The material properties are listed in Table 3.6.

Table 3.6 The material properties of MOSFET-based half-bridge

	$k\ [W/(m\cdot K)]$	$\rho\ [kg/m^3]$	$c_p\ [J/(kg\cdot K)]$
Silicon Carbide	120	3210	750
Solder	5	10500	235
Copper	400	8933	385
Ceramic	16	2400	691
TIM	6.5	2350	167
Hestsink	237.5	2689	951

3.4.2 Thermal Modelling

The simplified RC compact thermal model should be capable of taking into account lateral heat dissipation within the module and thermal interference between MOSFETs and the embedded PT1000 thermistor used as temperature sensor on the module baseplate. A thermal model of the power module and heatsink is thus established based on a Foster-type resistor-capacitor (RC) network as shown in Figure 3.19.

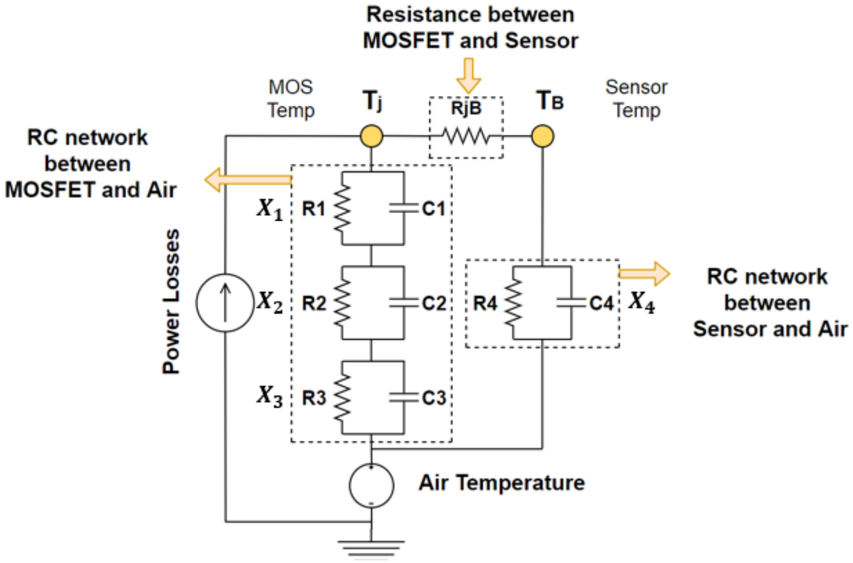

Figure 3.19 Lumped parameter thermal network.

The thermal network shown in Figure 3.19 requires three inputs

- MOSFET power loss P_{loss}
- Measured temperature T_B from Sensor B
- Inlet Air Temperature T_{amp} (Reference/Ambient).

As shown in Figure 3.19, the MOSFET losses P_{loss} are dissipated to the ambient via a third-order Foster network (R_1C_1 to R_3C_3). The temperature Sensor 'B' is thermally connected to the ambient via a first-order foster network (R_4C_4). The resistance R_{jB}, represents the thermal conduction between the device and temperature sensor. Therefore, the thermal network is of fourth order, making it relatively simple from a computational viewpoint and suitable for real-time application in a temperature monitoring system. The device junction temperature $T_j = X_1 + X_2 + X_3 + T_{air}$, where $X_{1,2,3}$ are the temperature rises across the respective RC elements. The lumped network could be replicated for each of the devices in the power module. For simplicity, in the following, only one network will be used to represent only the hottest device (MOS11).

The R_i, C_i parameters have been estimated using a parameters identification procedure based on CFD analyses. In particular, the model of a complete three-phase converter has been established in ANSYS ICEPAK CFD tool as shown in Figure 3.20.

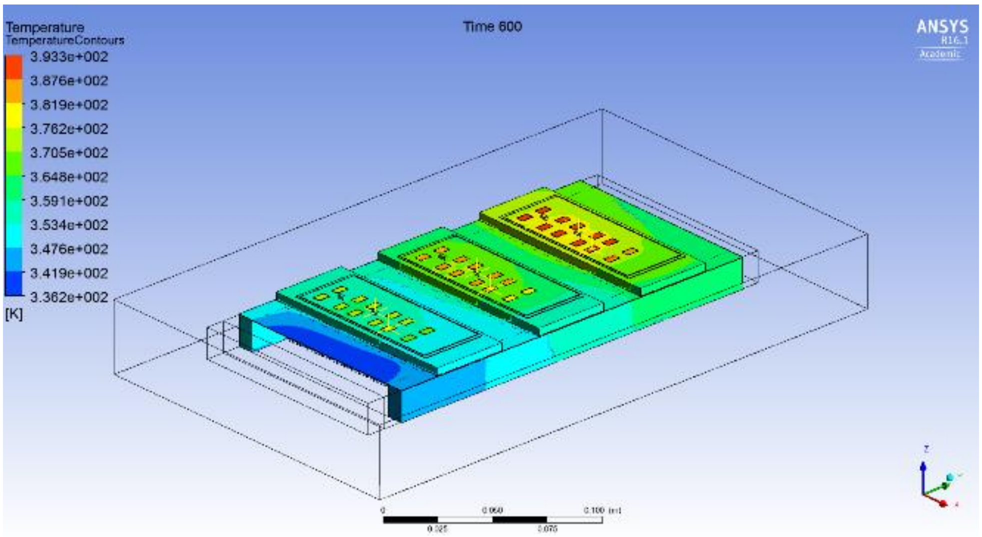

Figure 3.20 Model Simulation using ANSYS Icepak.

The boundary and operating conditions set during CFD simulations, whose results are used for parameter identification of the thermal network, are as follows:

- The power losses of MOSFET 11 P_{loss}= 12.5W (150 W per phase/12 MOSFETs)
- Reference / Ambient / inlet air temp. T_{amp}= 40 °C
- Reference inlet air speed = 4 m/s per phase/leg

The three power modules are mounted on a forced air-cooled parallel plate finned heatsink and the transient response to a step increase in power dissipation, is calculated. The inlet air temperature of the ANSYS Icepak model is 40°C with a fixed air flow rate of 4m/s. The three power modules are mounted on a forced air-cooled parallel plate finned heatsink and the transient response to a step increase of 450W in power dissipation, equally distributed across the 3×12 devices is calculated.

An adaptive mesh has been used in ANSYS, using a finer mesh to discretize the thinnest layers in the DCB. Mesh information of ANSYS ICEPAK model can be seen in Table 3.7.

Table 3.7 Mesh information of ANSYS ICEPAK model			
NODES	3151451	NEXAS	3050912
QUADS	540777	Faces + solids	1605
Computing element quality range		$1.45371\text{e-}13\text{m}^3 \sim 2.54977\text{e-}8\text{m}^3$	

A least square minimization procedure has been employed to calculate the R_i, C_i parameters that minimize the error between the results of the lumped parameters model and CFD. The estimated thermal parameters can be seen in Table 3.8.

Table 3.8 Estimated parameters			
Thermal resistances $[K/W]$		Thermal capacitances $[J/K]$	
R_1	1.71	C_1	37.41
R_2	3.59	C_2	1.17
R_3	2.40	C_3	22.39
R_4	11.27	C_4	4.10
R_{jB}	3.33		

The results of this parameters extraction method are also shown in Figure 3.21 demonstrating a good agreement between the CFD reference and the lumped parameter network.

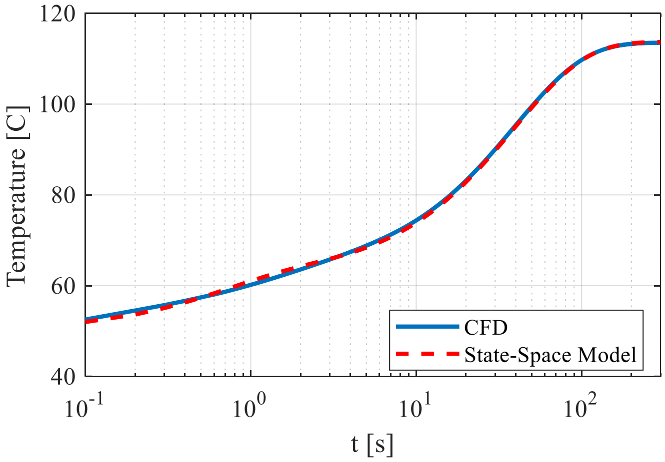

Figure 3.21 Transient thermal response for model parameter estimation.

It can be seen that the electro-thermal coupling simulation using the RC compact thermal model provides reasonable accuracy for the prediction of MOSFET in the power module.

Consequently, the model can be used for real-time temperature estimation. However, it must be noted that the derived model can the junction temperature accurately only if the following conditions are met.

- Inlet air temperature is known with reasonable accuracy,
- No change in boundary conditions,
- Modelling error in thermal model is minimal.
- Modelling error in power loss is minimal.

3.5 Summary

In this chapter, mathematical methods for thermal modelling methods are developed and applied to the thermal analysis of a power electronics module and its cooling system based on a parallel plate heatsink. The FDM is used for conductive thermal modelling, numerical modelling of convective heat transfer. Additionally, a simplified lumped parameter model based on the Foster thermal network is also proposed.

These results do not constitute the main novelty of the thesis but are essential in the derivation of the multi-parametric model order reduction and compact thermal modelling with reduced-order observer and disturbance estimation which are the subject of the following chapters. The computational complexity of the obtained 3-D dynamic finite difference thermal model will be reduced using model order reduction techniques in Chapter 4. Additionally, the design parameters conserved in multi-parametric order reduction technique are the convective heat transfer coefficients obtained from numerical modelling of convective heat transfer. Finally, the RC parameters estimated by the developed compact thermal model will be used in the observer design in Chapter 5.

Chapter 4 Multi-Parameter Model Order Reduction for Thermal Modelling of Power Electronics

4.1 Introduction

In this chapter, a novel multi-parameter model order reduction is applied to the thermal modelling and simulation of power electronics modules and air cooling system. Although widely employed, simulation tools based on finite elements (FE) or finite difference methods (FDM) result in computationally expensive models that hamper the analysis in studies where one or more parameters are changed. Model order reduction techniques can be applied to reduce the computational complexity. However, standard reduction techniques cannot easily consider parameters variability and need to be reapplied for each parameter value.

In order to use MOR techniques in design studies, it is desirable that the reduced order model conserves a dependency on a design parameter, e.g. the coolant mass flow rate, without the need to repeat the reduction process for each variation in parameters. This chapter presents a parametric MOR method that conserves parameters and demonstrates its application to a case where the boundary conditions representing a forced air cooled heatsink are modelled through several heat transfer coefficient parameters which are kept in the reduced order model. The method, based on multi-moment matching and block Arnoldi’s orthogonalization on standard Krylov subspaces, is analytically derived. The method is illustrated and its benefits demonstrated with reference to a power module mounted on a forced air cooled finned heatsink. Detailed comparisons with commercial CFD software and experimental measurements demonstrate the accuracy and computational efficiency of the proposed method.

4.2 Non-Parametric Model Order Reduction Methods Based on Block Krylov Subspace

A multi-input-multi-output (MIMO) system of ordinary differential equations (ODE) can be obtained as

$$C\dot{T}(t) + KT(t) = FQ(t)$$

$$y = E^T T(t) \tag{4.2.1}$$

Where

- $K(x, y, z)$: The thermal conductivity matrix generated from $R_{th}(x, y, z)$.
- $C(x, y, z)$: The heat capacity matrix generated from $C_{th}(x, y, z)$.
- $Q(x, y, z, t)$: The heat source generated from $q(x, y, z, t)$.
- T : The temperature distribution vectors.
- y : The chosen output temperature distribution vectors.
- $F \in R^{n\times m}$: The input matrix.
- $E \in R^{n\times p}$: The output matrix.
- n: The dimension of state space.
- m: The number of inputs.
- p: The number of outputs.

4.2.1 Arnoldi's Orthogonalization on Standard Krylov Subspaces

The Krylov subspace techniques require a single matrix representation of a first order ODE system. Equation (4.2.1) can be rewritten as

$$A\dot{T}(t) = T(t) + BQ(t)$$

$$y = E^T T(t) \tag{4.2.2}$$

Where

- $A = -K^{-1}C$

- $B = -K^{-1}F$

To make the derivation clear, reduction algorithm based on Krylov subspace can start from the single-input-single-output (SISO) case, i.e. $m = p = 1$ (for SISO the lower case letters b and e are used for the input and output arrays) as equation (4.2.3). Krylov subspace reduction in MIMO can be obtained using the similar method.

$$A\dot{T}(t) = T(t) + b \cdot Q(t)$$
$$y = e^T \cdot T(t) \tag{4.2.3}$$

The SISO transfer function can be defined as:

$$G(s) = -e^T(I - sA)^{-1}b \tag{4.2.4}$$

The Taylor series expansion of $G(s)$ about $s_0 = 0$ is expressed as:

$$G(s) = -e^T(I + sA + s^2A^2 + \cdots)b_K = \sum_{i=0}^{\infty} m_i s^i \tag{4.2.5}$$

Where $m_i = -e^T A^i b$ are called moments about s_0.

Krylov subspace methods can be used to reduce the system order by choosing $G_r(s)$ as a Padé or Padé-type approximant of $G(s)$, and $G_r(s)$ is the r-th Padé approximant of the transfer function $G(s)$ about the expansion point s_0,

For $r = 1,2, \ldots$, the subspace:

$$K_r^R\{A_K, b\} = span\{b, Ab, \ldots, A^{r-1}b\} \tag{4.2.6}$$

$K_r^R\{A, b\}$ is called the r-th right Krylov subspace, induced by A and b. The vectors from (4.2.6) quickly become almost linearly dependant and the solution is to construct more stable basis vectors $v_1, v_2, \ldots, v_r$ saved in columns of matrix V as follows

$$K_r^R\{A, b\} = span\{v_1, v_2, \ldots, v_r\} \tag{4.2.7}$$

The Arnoldi process produces the sequence of the vectors $v_1, v_2, \ldots, v_r$,which span the right Krylov subspace (4.2.6) and are othonormal [73]:

$$v_i^T v_j = \begin{cases} 1, if\ i = j \\ 0, if\ i \neq j \end{cases} for\ all\ 1 \leq i, j \leq r \tag{4.2.8}$$

Then, the upper Hessenberg matrix $H_r = R^{r\times r}$ (with $h_{ij} = 0,\ \forall(i,j), |i-j| > 1$) can be obtained as follows:

$$V^T \cdot A \cdot V = H_r \tag{4.2.9}$$

The matrix H_r can be considered as an orthogonal projection of the matrix A onto the Krylov-subspace (4.2.6) and it is equal to the system matrix of the reduced system A_r. The algorithm can be summarised as follows [73].

- Set $\hat{v} = b$
- Compute $h_{i,i-1} = \|\widehat{v_i}\|$ for $i = 1,2,\dots,r$ and stop when $h_{i,i-1} = 0$
- Set $v_i = \widehat{v_i}/h_{i,i-1}$
- Set $v_{i+1} = Av_i$
- Set $h_{i,i-1} = v_j^T\hat{v}_{i+1}$ and $\hat{v}_{i+1} = \hat{v}_{i+1} - v_j h_{j,i}$ for $j = 1,2,\dots,i$
- Obtain $V_r = [v_1, v_2, \dots, v_r]$

System (4.2.3) can be reduced as

$$A_r\dot{T}(t) = T(t) + b_r \cdot Q(t)$$

$$y = e_r^T \cdot T(t) \tag{4.2.10}$$

Where

- $A_r = V_r^T A V_r$
- $b_r = V_r^T b$
- $e_r = V_r^T e$

4.2.2 Non-Parametric Moment Matching of Block Arnoldi Method

In Section 4.2.1, the Arnoldi reduction method based on Krylov subspace in SISO case has been derived. The block Arnoldi method can obtain the reduction of MIMO heat transfer model in a similar manner to the standard SISO case [84]. Transforming (4.2.1) into the frequency domain result in a matrix-valued rational transfer function $G: C \rightarrow C^{p\times m}$ given by:

$$G(s) = E^T \cdot (K + sC)^{-1} \cdot F, \qquad s \in \mathbb{C} \tag{4.2.11}$$

Which can be rewritten as

$$G(s) = E^T \cdot (I - (-K^{-1}C)s)^{-1} \cdot (K^{-1}F) \tag{4.2.12}$$

The block Arnoldi method obtains the information of the leading Taylor coefficients of $G(s)$. Expanding $G(s)$ in (4.2.12) around a point s_0:

$$G(s) = \sum_{i=0}^{\infty} E \cdot M_i \, s^i \tag{4.2.13}$$

Where the moments M_i are given by:

$$M_i = [(-(s_0C + K))^{-1}C]^i \cdot (s_0C + K)^{-1} \cdot F \tag{4.2.14}$$

If, for simplicity, $s_0 = 0$, then $M_i = (-K^{-1}C)^i \cdot (K^{-1}F)$, therefore, matching the moments of the reduced order model to the first i moments of the original system (4.2.13) can be obtained by selecting the projection matrix V:

$$V = \ Kr^i(A, B) = span([B \ AB \ A^2B \ \dots \ A^{N-1}B]) \tag{4.2.15}$$

Where

- $A = -K^{-1}C$
- $B = K^{-1}F$

$Kr^N(A, B)$ is so-called block Krylov subspace. m columns of the matrix $B = [b_1 \ b_2 \ \dots \ b_m]$ are starting vectors of the block Krylov subspace $Kr^N(A, B)$. The moment matching based on Krylov subspaces is expressed to find a low-dimensional model that matches the first moments in the Taylor expansion shown in (4.2.14). A reduction to a specified order r is obtained by selecting a subspace spanned by an orthogonal basis formed by the first r columns of $K^i(A, B)$. A numerically stable method to generate orthogonal basis vectors of this subspace, based on the Arnoldi process, is detailed in the Table 4.1 [90].

Table 4.1 Arnoldi's orthogonalization

$A = -K^{-1}C, B = K^{-1}F.$	Block Krylov subspaces
$for\ i = 1, \dots, j_{max}$	Normalized B_i to $\|v_i\|$=1
$\quad v_i = B_i / \|B_i\|$	Start computation of v_{i+1}
$for\ j = 1, \dots, j_{max} - 1$	One matrix multiplication
$\quad t = Av_i$	t is in the space K_{j+1}
$\quad h_{ij} = v_i^T t$	$h_{ij}v_i$= projection of t on v_i
$\quad t = t - h_{ij}v_i$	Subtract that projection
end	t is orthogonal to $v_1, \dots, v_j$
$\quad h_{j+1,j} = \|t\|$	Compute the length of t
$\quad v_{j+1} = t/h_{j+1,j}$	Normalize t to $\|v_{j+1}\|$=1
end	$v_1, \dots, v_{jmax}$ are orthonormal

Then the reduction of the full-order system (4.2.1) can be expressed with the projection matrix V, as in (4.2.16)

$$C_r\dot{z} + K_r z = F_r \cdot Q(t)$$

$$y_r = E_r^T \cdot z \tag{4.2.16}$$

Where

- $C_r = V^T CV$
- $K_r = V^T KV$
- $F_r = V^T F$
- $E_r = V^T E$

4.2.3 Validation of Non-Parametric Model Order Reduction Methods

The same simplified model with Section 3.2 is applied in the validation of the proposed MOR method. In the simplified case, the copper base plate has a convective boundary condition on the bottom layer, which is modelled by a constant heat transfer coefficient

$h = 1.2 \times 10^4 W/(m^2K)$ and the inlet air temperature $T_{air} = 0$°C. The discretization used in the full-order model results in a system with 5879 nodes, while the chosen reduced order has 18 ($r = 2m$) states, corresponding to 9 nodes (m =9) representing the input power source on the MOSFET.

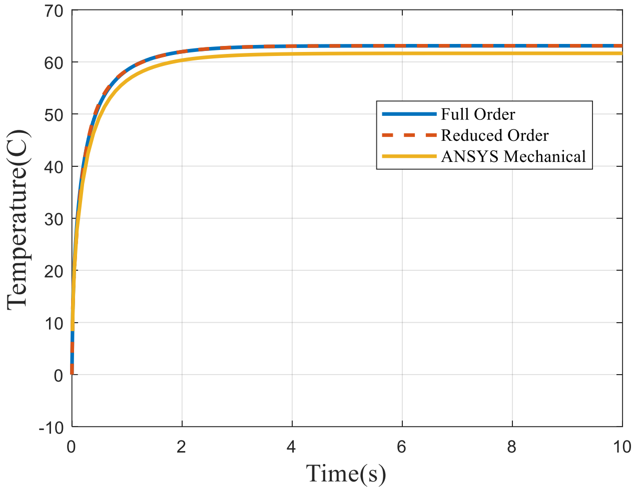

(a)

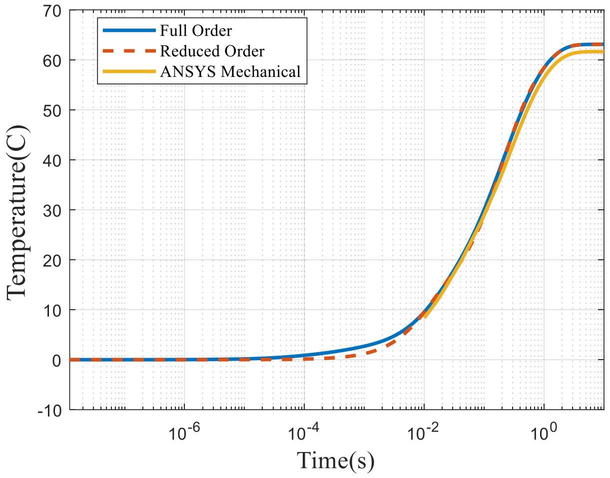

(b)

Figure 4.1 Comparison of reduced-order, full-order model and ANSYS.

Figure 4.1 show the transient response of the MOSFET temperature obtained via reduced-order and full-order numerical simulation and commercial FE tool ANSYS Mechanical. An excellent data agreement can be found among the finite difference full order, the proposed reduced order method and the ANSYS.

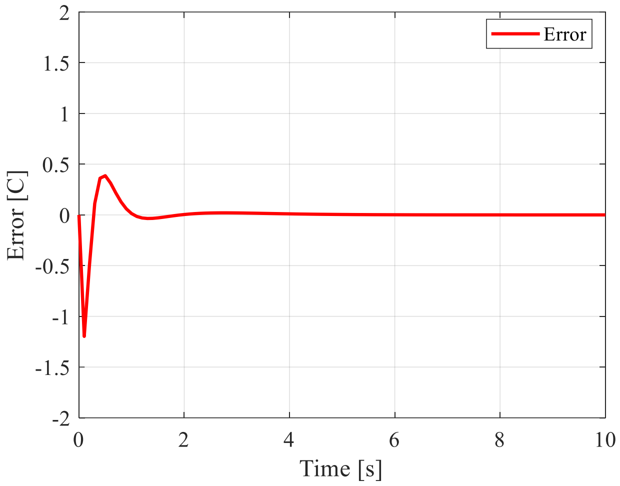

Figure 4.2 Transient error between full-order model and reduced-order model

Figure 4.2 illustrates the transient temperature error between full-order model and reduced-order model, which is less than 1%.

4.3 Multi-Parameter Model Order Reduction

In this thesis, the geometry-based numerical thermal modelling with MOR should be developed to address the fast thermal simulation in the electronic design process, including the design of power modules and cooling systems. Some geometrical parameters, e.g. the length and width of baseplate and/or property parameters, e.g. the thermal conductivities of TIMs or sinter materials, will be changed with varied designed power converters. Similar parameter variation, e.g. the convective heat transfer coefficients, can be found in different designed cooling system. In the non-parametric case proposed in section 4.2, the reduction processes need to be repeated as the original full-order systems are changes due to the varied designed parameters. In order to use MOR techniques in design studies, it is desirable that the reduced order model conserves a dependency on a design parameter, especially the design parameters of the cooling system, without the need to repeat the reduction process for each variation in parameters.

As an example, the parameters conserved in this thesis are local heat transfer coefficients obtained from proposed convective thermal modelling of cooling system. The mentioned geometrical parameters and property parameters can also be conserved using the same method.

Similarly to the non-parametric case, ODEs system of the form (4.2.1) are considered. In section 3.3, the local equivalent heat transfer coefficient $h_{equ}(z)$, as a function of axial position of baseplate along the air flow, has been analysed. Based on this case, it is assumed that the convection boundary layer has a multi-parameter dependence on air mass flow.

The MIMO system with heat transfer coefficients $h_1 h_2 \dots h_n$ in discretized form are thus given by:

$$C\dot{T}(t) + (K + h_1 K_1 + h_2 K_2 + \cdots + h_n K_n)T(t) = F \cdot Q(t)$$

$$y = E^T \cdot T(t) \tag{4.3.1}$$

The multi-parameter model can be derived from 2-parameter model order reduction as an example. The MIMO system with two parameters h_1 and h_2 in discretized form is given by:

$$
\begin{gathered}
C\dot{T}(t) + (K + h_1K_1 + h_2K_2)T(t) = F \cdot Q(t) \\
y = E^T \cdot T(t)
\end{gathered}
\tag{4.3.2}
$$

4.3.1 Multi-Parametric Moment Matching

The transfer function for (4.3.2) is

$$
\begin{aligned}
G(s) &= E \cdot (K + h_1K_1 + h_2K_2 + sC)^{-1} \cdot F \\
&= E[I - (-(K + h_1K_1 + h_2K_2)^{-1}Cs)]^{-1} \\
&\quad \cdot (K + h_1K_1 + h_2K_2)^{-1}F \\
&= E\sum_{i=0}^{\infty}[-(K + h_1K_1 + h_2K_2)^{-1}C]^i(+h_1K_1 + h_2K_2)^{-1}Fs^i \\
&= E\sum_{i=0}^{\infty} M_i s^i
\end{aligned}
\tag{4.3.3}
$$

Where $M_i, i = 0,1, \ldots$ are the moments of $G(s)$.

When $i = 0$;

$$
\begin{aligned}
M_0 &= (K + h_1K_1 + h_2K_2)^{-1}F \\
&= \big(I + K^{-1}(h_1K_1 + h_2K_2)\big)^{-1}K^{-1}F \\
&= \Big(I - \big(-K^{-1}(h_1K_1 + h_2K_2)\big)\Big)^{-1}K^{-1}F
\end{aligned}
\tag{4.3.4}
$$

When $i = 1$;

$$
\begin{aligned}
M_1 &= -(K + h_1K_1 + h_2K_2)^{-1}C(K + h_1K_1 + h_2K_2)^{-1}F \\
&= -(K + h_1K_1 + h_2K_2)^{-1}CM_0 \\
&= -\Big(I - \big(-K^{-1}(h_1K_1 + h_2K_2)\big)\Big)^{-1}K^{-1}CM_0
\end{aligned}
\tag{4.3.5}
$$

For the ith moment,

$$
\begin{aligned}
M_i &= [-(K+h_1K_1+h_2K_2)^{-1}C]^i(K+h_1K_1+h_2K_2)^{-1}F \\
&= [-(K+h_1K_1+h_2K_2)^{-1}C]M_{i-1} \\
&\cdots \\
&= [-(K+h_1K_1+h_2K_2)^{-1}C]^iM_0 \\
&= \left[-\left(I-\left(-K^{-1}(h_1K_1+h_2K_2)\right)\right)^{-1}\right]^i[K^{-1}C]^iM_0
\end{aligned}
\tag{4.3.6}
$$

The term $f(h_1,h_2)=\left(I-\left(-K^{-1}(h_1K_1+h_2K_2)\right)\right)^{-1}$ appearing in $M_0,M_1,\cdots,M_j$ is an infinitely differentiable function in an open neighborhood around $(h_1,h_2)=(0,0)$, therefore it can be expressed using the multi-variable Taylor expansion as:

$$
\begin{aligned}
f(h_1,h_2) &= f(0,0) \\
&+\frac{1}{1!}\left[f_{h_1}(0,0)h_1+f_{h_2}(0,0)h_2\right] \\
&+\frac{1}{2!}\left[f_{h_1h_1}(0,0)h_1^2+2f_{h_1h_2}(0,0)h_1h_2+f_{h_2h_2}(0,0)h_2^2\right] \\
&+\cdots
\end{aligned}
\tag{4.3.7}
$$

Where

$$
\begin{aligned}
f_{h_1}(h_1,h_2) &= \frac{\partial}{\partial h_1}\left(f(h_1,h_2)\right) \\
&= -\left(I-\left(-K^{-1}(h_1K_1+h_2K_2)\right)\right)^{-2}\cdot(K^{-1}K_1)
\end{aligned}
\tag{4.3.8}
$$

$$
\begin{aligned}
f_{h_2}(h_1,h_2) &= \frac{\partial}{\partial h_2}\left(f(h_1,h_2)\right) \\
&= -\left(I-\left(-K^{-1}(h_1K_1+h_2K_2)\right)\right)^{-2}\cdot(K^{-1}K_2)
\end{aligned}
\tag{4.3.9}
$$

$$
\begin{aligned}
f_{h_1h_1}(h_1,h_2) &= \frac{\partial^2}{\partial h_1^2}\left(f(h_1,h_2)\right) \\
&= 2\left(I-\left(-K^{-1}(h_1K_1+h_2K_2)\right)\right)^{-3}\cdot(K^{-1}K_1)^2
\end{aligned}
\tag{4.3.10}
$$

$$f_{h_2h_2}(h_1,h_2) = \frac{\partial^2}{\partial h_2^2}\big(f(h_1,h_2)\big)$$
$$= 2\Big(I - \big(-K^{-1}(h_1K_1 + h_2K_2)\big)\Big)^{-3} \cdot (K^{-1}K_2)^2 \tag{4.3.11}$$

$$f_{h_1h_2}(h_1,h_2) = \frac{\partial^2}{\partial h_1 h_2}\big(f(h_1,h_2)\big) = \frac{\partial}{\partial h_1}\left(\frac{\partial}{\partial h_2}\big(f(h_1,h_2)\big)\right)$$
$$= 2\Big(I - \big(-K^{-1}(h_1K_1 + h_2K_2)\big)\Big)^{-3} \cdot (K^{-1}K_1) \cdot (K^{-1}K_2) \tag{4.3.12}$$

Therefore, equation (4.3.7) can be expressed as

$$\begin{aligned} f(h_1,h_2) &= f(0,0) \\ &+\frac{1}{1!}\left[f_{h_1}(0,0)h_1 + f_{h_2}(0,0)h_2\right] \\ &+\frac{1}{2!}\left[f_{h_1h_1}(0,0)h_1^2 + 2f_{h_1h_2}(0,0)h_1h_2 + f_{h_2h_2}(0,0)h_2^2\right] \\ &+\cdots \\ &= I - K^{-1}(K_1h_1 + K_2h_2) + \big(-K^{-1}(K_1h_1 + K_2h_2)\big)^2 + \cdots \\ &= \sum_{i_0=0}^{\infty}(-K^{-1}(K_1h_1 + K_2h_2))^{i_0} \end{aligned} \tag{4.3.13}$$

Consequently, M_0 of equation (4.3.4) can be written as follows

$$M_0 = \sum_{i_0=0}^{\infty}(-K^{-1}(K_1h_1 + K_2h_2))^{i_0}K^{-1}F \tag{4.3.14}$$

A simplification can be achieved if mixing moments can be ignored. This is based on the assumption that $K_1 \cdot K_2 = 0$. For the problem under investigation, i.e. the thermal analysis of power modules with convective boundary conditions, the parameters series h_1 h_2 ... h_n and submatrices K_1 K_2 ... K_n only appear in the equations of the states on boundary layer of the baseplate.

The temperature distribution $T(x,y,z)$ is discretized and stored in a square system of dimension of $n = n_x n_y n_z$. x- and y-axis represent the temperature probes on horizontal layers while z-axis represents the vertical temperature distributions. Thermal capacity and conductivity matrices C, K, K_1, $K_2\ldots$ are sparse matrices with only few non-zero elements.

According to the heat transfer equation, the non-zero elements of K, K_1 and K_2 are the inverse value of the heat thermal resistances between nodes of the discretization. Figure 4.3 visually illustrates the heat conduction matrix on the n_zth layer.

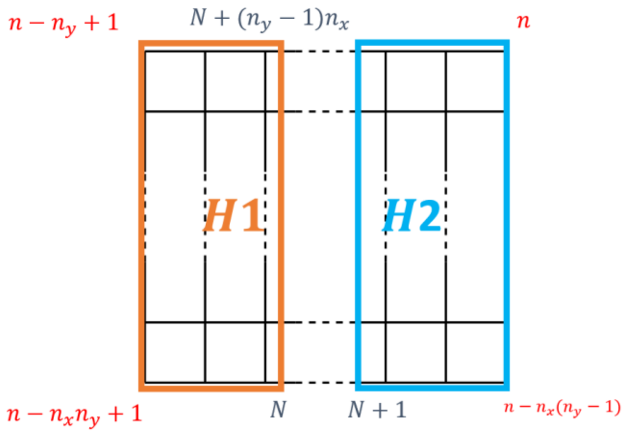

Figure 4.3 2D figure for analysis of heat transfer matrix on the n_z th layer

The 2D illustration shows that the heat transfer matrix is divided into two sections. The non-zero elements of K_1 are contained in the left (orange) area with heat transfer coefficient h_1 and are zero elsewhere and vice versa for K_2. For example, for the nth node , the heat transfer is non zero only between its adjacent nodes, which are $(n-1)$th, $(n-n_x)$th and $(n-n_xn_y)$th. This means that the non-zero elements of the nth row are only located in the the nth, $(n-1)$th, $(n-n_x)$th and $(n-n_xn_y)$th columns. Consequently, matrix K_1 and K_2 can be expresses follows

$$K=\begin{bmatrix} E_{conduction} \\ E_{zeroK} \end{bmatrix}$$

$$K_1=\begin{bmatrix} E_{zeroK_1} \\ E_{h_1} \end{bmatrix}$$

$$E_{h_1}=\begin{bmatrix} \ddots & \vdots & \vdots & \vdots & \vdots \\ \cdots & E_{(n-n_xn_y+1,\ n-n_xn_y+1)} & E_{(n-n_xn_y+1,\ n-n_xn_y+2)} & \cdots & 0 \\ \cdots & E_{(n-n_xn_y+2,\ n-n_xn_y+1)} & E_{(n-n_xn_y+2,\ n-n_xn_y+2)} & \cdots & 0 \\ \cdots & \vdots & \vdots & \ddots & 0 \\ \cdots & 0 & 0 & 0 & 0 \end{bmatrix}$$

$$K_2=\begin{bmatrix} E_{zeroK_2} \\ E_{h_2} \end{bmatrix}$$

$$E_{h_2} = \begin{bmatrix} \ddots & \vdots & \vdots & \vdots & \vdots \\ \cdots & 0 & 0 & 0 & 0 \\ \ldots & 0 & \ddots & \vdots & \vdots \\ \cdots & 0 & \cdots & E_{(n-1,\ n-1)} & E_{(n-1,\ n)} \\ \cdots & 0 & \ldots & E_{(n,\ n-1)} & E_{(n,\ n)} \end{bmatrix} \tag{4.3.15}$$

Where

- $K\ K_1\ K_2 \in \mathbb{R}^{n\times n}$,
- $E_{conduction}\ \ E_{zeroK_1}\ E_{zeroK_1} \in \mathbb{R}^{(n-n_x n_y)\times n}$
- $E_{zeroK}\ E_{h_1}\ E_{h_2} \in \mathbb{R}^{(n_x n_y)\times n}$.

It is evident that the locations of non-zero elements in K_1 and K_2, results in $K_1 \cdot K_2 = 0$. Similar assumption and derivation can be applied in the case with more than 2 parameters. The terms containing the parameters in (4.3.14) can be further simplified using:

$$(h_1K_1 + h_2K_2)^{\,i_0} \approx (K_1 + K_2)^{\,i_0}\frac{h_1^{\,i_0} + h_2^{\,i_0}}{2} \qquad i_0 = 0{,}1, \ldots \infty \tag{4.3.16}$$

The error in this approximation can be expressed as:

$$\begin{aligned} K_e = {} & (h_1K_1 + h_2K_2)^{\,i_0} - (K_1 + K_2)^{\,i_0}\frac{h_1^{\,i_0} + h_2^{\,i_0}}{2} \\ = {} & (h_1K_1)^{\,i_0} + (h_2K_2)^{\,i_0} - \left(K_1^{\,i_0} + K_2^{\,i_0}\right)\frac{h_1^{\,i_0} + h_2^{\,i_0}}{2} \\ = {} & \frac{h_1^{\,i_0} - h_2^{\,i_0}}{2}\left(K_1^{\,i_0} - K_2^{\,i_0}\right) \end{aligned} \tag{4.3.17}$$

Where

$$K_e(\,i_0 = 0) = \ 0 \tag{4.3.18}$$

$$K_e(\,i_0 = 1) = \frac{h_1 - h_2}{2}(K_1^1 - K_2^1) \tag{4.3.19}$$

$$\begin{aligned} K_e(\,i_0 = 2) &= \frac{h_1^2 - h_2^2}{2}(K_1^2 - K_2^2) \\ &= \frac{(h_1 - h_2)(h_1 + h_2)}{2}(K_1^2 - K_2^2) \end{aligned} \tag{4.3.20}$$

$$\ldots$$

$$K_e(\, i_0 = \, i_\infty) = \frac{h_1^{i_\infty} - h_2^{i_\infty}}{2}\left({K_1}^{i_\infty} - {K_2}^{i_\infty}\right)$$

$$= \frac{(h_1 - h_2)\begin{pmatrix} h_1^{i_\infty - 1} + h_1^{i_\infty - 2} h_2 \\ + \cdots \\ h_1 h_2^{i_\infty - 2} + h_2^{i_\infty - 1} \end{pmatrix}}{2}\left({K_1}^{i_\infty} - {K_2}^{i_\infty}\right) \tag{4.3.21}$$

It can then be concluded that the smaller $h_1 - h_2$, the smaller the error. This can be achieved with a finer discretization of the convective heat transfer at the boundary condition: assuming there are n heat transfer coefficients $h_1 h_2 \dots h_n$, the error will be proportional to $(h_1 - h_2)(h_2 - h_3)\dots(h_{n-1} - h_n)$. With an increasing n, the step difference of adjacent parameters $h_{n-1} - h_n$ will reach zero, and error K_e approaches zero correspondingly.

Based on the above two assumptions, the term (4.3.14) can be rewritten as:

When $i = 0$;

$$M_0 = \sum_{i_0}^{\infty} (-K^{-1}(h_1 K_1 + h_2 K_2))^{i_0} K^{-1} F$$

$$= \sum_{i_0}^{\infty} \left(-K^{-1}(K_1 + K_2)\right)^{i_0} K^{-1} F (h_1^{i_0} + h_2^{i_0})/2 \tag{4.3.22}$$

When $i = 1$;

$$M_1 = -\left(I - \left(-K^{-1}(h_1 K_1 + h_2 K_2)\right)\right)^{-1} K^{-1} C M_0$$

$$= \left[-\sum_{i_1}^{\infty} \left(-K^{-1}(K_1 + K_2)\right)^{i_1} K^{-1} C (h_1^{i_1} + h_2^{i_1})/2 \right]$$

$$\cdot \left[\sum_{i_0}^{\infty} \left(-K^{-1}(K_1 + K_2)\right)^{i_0} K^{-1} F (h_1^{i_0} + h_2^{i_0})/2 \right] \tag{4.3.23}$$

For the ith moment

$$M_i = [-(K + h_1 K_1 + \, h_2 K_2)^{-1} C] M_{i-1}$$

$$= \left[-\sum_{t_i}^{\infty} \left(\left(-K^{-1}(K_1 + K_2)\right)^{t_i} K^{-1} C (h_1^{t_i} + h_2^{t_i})/2 \right) \right] \cdot M_{i-1}$$

$$= \left[-\sum_{t_i}^{\infty} \left(\left(-K^{-1}(K_1+K_2)\right)^{t_i} K^{-1} C (h_1^{t_i} + h_2^{t_i})/2 \right) \right]$$

$$\cdot \left[-\sum_{t_{i-1}}^{\infty} \left(\left(-K^{-1}(K_1+K_2)\right)^{t_{i-1}} K^{-1} C (h_1^{t_{i-1}} + h_2^{t_{i-1}})/2 \right) \right] \cdot M_{i-2}$$

$$\cdots$$

$$= (-1)^i \sum_{t_i=0}^{\infty} \sum_{t_{i-1}=0}^{\infty} \cdots \sum_{t_1=0}^{\infty} \sum_{t_0=0}^{\infty} \begin{bmatrix} \left(-K^{-1}(K_1+K_2)\right)^{t_i} K^{-1} C \\ \cdot \left(-K^{-1}(K_1+K_2)\right)^{t_{i-1}} K^{-1} C \\ \cdots \\ \cdot \left(-K^{-1}(K_1+K_2)\right)^{t_1} K^{-1} C \\ \cdot \left(-K^{-1}(K_1+K_2)\right)^{t_0} K^{-1} F \end{bmatrix}$$

$$\cdot \left(\frac{h_1^{t_i} + h_2^{t_i}}{2} \right) \left(\frac{h_1^{t_{i-1}} + h_2^{t_{i-1}}}{2} \right) \cdots \cdot \left(\frac{h_1^{t_1} + h_2^{t_1}}{2} \right) \left(\frac{h_1^{t_0} + h_2^{t_0}}{2} \right) \tag{4.3.24}$$

As demonstrated in (4.3.22) - (4.3.24), the parameters h_1 and h_2 are separated from the system matrices. Consequently, it is possible to make the subspace $span(M_0, M_1, M_2, \ldots\ M_i)$ independent of the parameters. The first moment M_0 can then be expressed as the Krylov subspace:

$$spancol\{V_0\} = Kr^{i_0}(-K^{-1}(K_1 + K_2), K^{-1}F) \tag{4.3.25}$$

Similar methods can be applied in the multi-parameter system with more than two parameters in (4.3.1) as follows

$$spancol\{V_0\} = Kr^{i_0}(-K^{-1}(K_1 + K_2 + \cdots + K_n), K^{-1}F) \tag{4.3.26}$$

The generation of orthogonal basis vectors of this subspace, based on the Arnoldi process, is reported in the Table 4.2.

Table 4.2 Multi-parameteric Arnoldi's orthogonalization

$A = -{K_0}^{-1}(sum(K_i)),\ B = -{K_0}^{-1}F.$	Block Krylov subspaces
$for\ i = 1, \ldots, j_{max}$	Normalized B_i to $\|v_i\|$=1
$v_i = B_i/\|B_i\|$	Start computation of v_{i+1}
$for\ j = 1, \ldots, j_{max} - 1$	One matrix multiplication
$t = Av_i$	t is in the space K_{j+1}

$h_{ij} = v_i^T t$	$h_{ij} v_i$= projection of t on v_i
$t = t - h_{ij} v_i$	Subtract that projection
end	t is orthogonal to $v_1, \dots, v_j$
$h_{j+1,j} = \|t\|$	Compute the length of t
$v_{j+1} = t/h_{j+1,j}$	Normalize t to $\|v_{j+1}\|$=1
end	$v_1, \dots, v_{jmax}$ are orthonormal

The proposed MOR procedure can be summarized in the following steps:

1. The heat transfer equation is discretized using Finite Difference (or FE) methods into a set of parametric ODE of order N (4.3.1) dependent on the parameters $h_{1,\dots}h_n$.

2. The first k moments $M_k, i = 0, \dots, k$ of the Taylor series of the transfer function are calculated using (4.3.22) - (4.3.24) which are, by definition, Krylov subspaces as in (4.3.26).

3. The Arnoldi method (Appendix) is applied to generate a numerically stable, orthogonal basis sets for the Krylov subspaces, resulting in the projection matrix V of dimension $r \ll N$.

4. The original full-order system of order N is now transferred to a reduced-order model of order r, where the dependence on the parameters is conserved in the system matrices C_r, K_r, F_r.

4.3.2 Validation of Multi-Parametric Model Order Reduction Methods

The same simplified model with Section 3.2 is applied in the validation of the proposed multi-parametric MOR method. The difference of the simplified model compared with the model used in Section 3.2 and Section 4.1, is the convective heat transfer coefficient h. There are three local heat transfer coefficients $h_{1\sim 3}$ at different axial position of baseplate along the air flow, as shown in Figure 4.4.

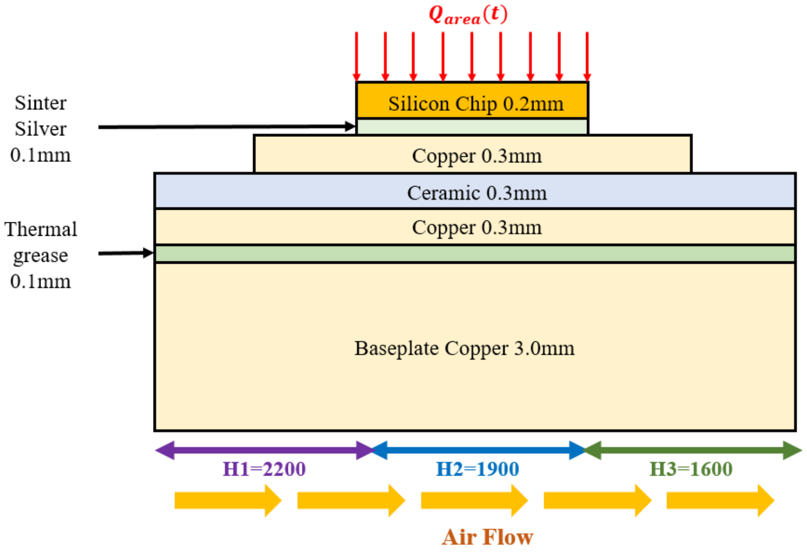

Figure 4.4 Simplified model with different heat transfer coefficients.

In the simplified case, the copper base plate has a convective boundary condition on the bottom layer, which is modelled by different heat transfer coefficient $h_{1\sim3} = 2200, 1900, 1600 W/(m^2K)$ and the inlet air temperature $T_{air} = 0$°C. The discretization used in the full-order model results in a system with 5879 nodes, while the chosen reduced order has 18 $(r = 2m)$ states, corresponding to 9 nodes (m =9) representing the input power source on the MOSFET.

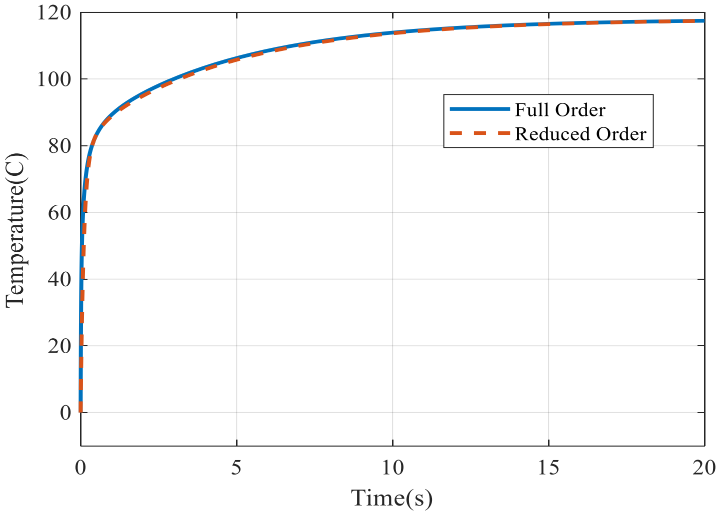

(a)

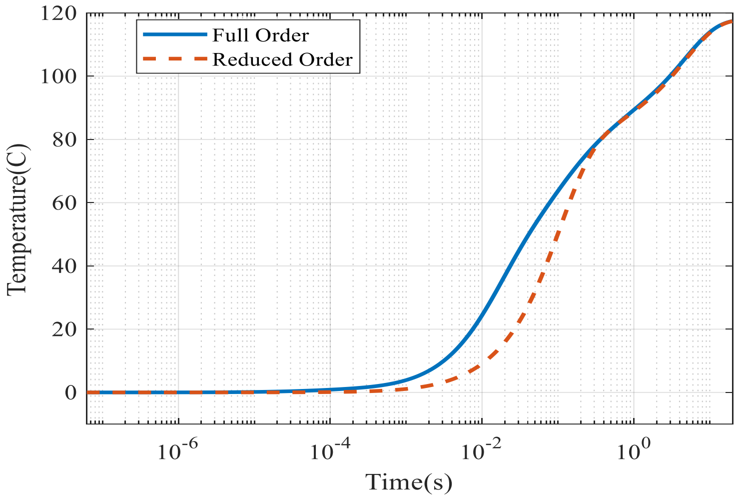

(b)

Figure 4.5 Comparison of reduced-order and full-order model.

Figure 4.5 show the transient response of the MOSFET temperature obtained via multi-parameter reduced-order and full-order numerical simulation. An excellent data agreement can be found among the finite difference full order, the proposed reduced order method and the ANSYS.

Figure 4.6 illustrates the transient temperature error between full-order model and reduced-order model, which is less than 1%.

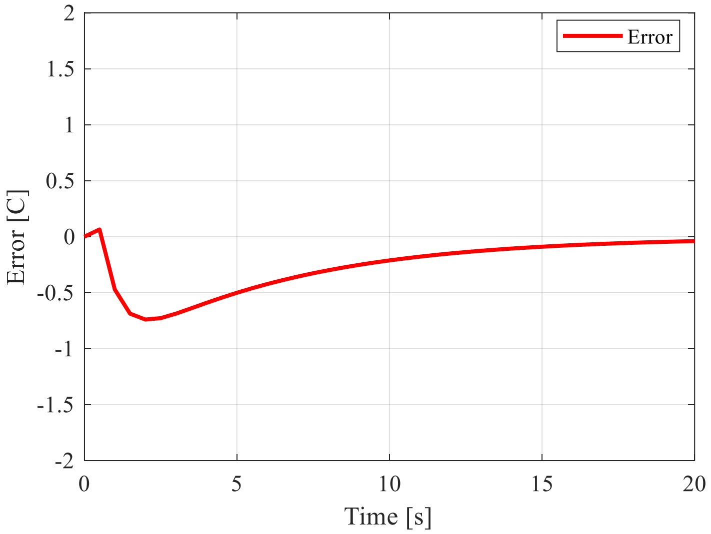

Figure 4.6 Transient error between full-order model and reduced-order model

As to the calculating time, the solving time of multi-parameter MOR model is similar to the non-parameter MOR proposed in Section 4.1, while avoiding the repeated MOR process due to the change of boundary conditions will contribute to the evident reduction of calculation load.

4.4 Key Steps in MATLAB/Simulink of 3-D Model with MOR

Due to the complexity of the geometry structure multi-chip power modules, the complete 3-D numerical thermal modelling is separated into 12 sub-models and each sub-model has one MOSFET chip, as is shown in Figure 4.7.

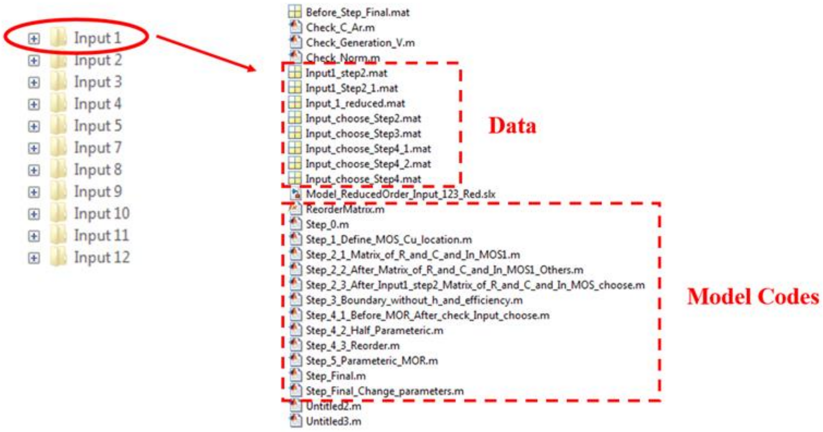

Figure 4.7 Key steps in MATLAB/Simulink of 3-D numerical model with MOR

Firstly, relative MATLAB codes are programmed. There are over 5000-line MATLAB codes for each sub-model, resulting huge computational load. Consequently, the MATLAB codes are divided into several steps as follows.

- Step 1 is the geometry definition of power modules.
- Step 2.1 to 2.3 is the generation of 3-D thermal model without convective boundary condition.
- Step 3 supplies the boundary condition without convective heat transfer coefficients.
- Step 4 and 5 are used for model order reduction.
- The final step is introducing the heat transfer coefficients to complete the reduced order model.

To realise the automatic control, Step 0 is used to run the model and save data as well as change the MOSFET location for each sun-model automatically. After the above MATLAB programing, the second step is data saving and the final step is running Simulink Model.

4.5 Experimental Validation of Multi-Parameter Model Order Reduction

Experimental validation of the proposed MOR technique is presented in this section with reference to a configuration, with one power module and two power resistors acting as heat sources. The experimental validation provides a more challenging application of air-force cooling system and Silicon Carbide (SiC) MOSFET-based half-bridge with DC power supply, which is partly representative of real industrial applications. In this validation, DC currents are used as source of power losses. These can be easily measured, reducing the uncertainties. The difference between the validation introduced in this section and the Section 4.3 is not only the increased system complexity, but also the use of convective heat transfer model developed in Chapter 3 to calculate convective heat transfer coefficients.

Except for the experimental validation under DC power supply of power module and fixed air flow rate, validation with time-varied pause power supply of power module and transient air flow rate is introduced to modify a more complex condition.

4.5.1 Power Module

Figure 4.8 shows CAD drawings of the half-bridge wire-bondless power module, which is the same module used in Section 3.4.

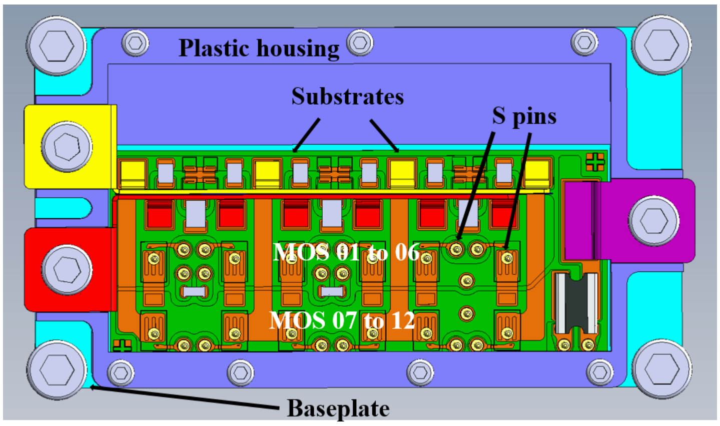

Figure 4.8. CAD drawings of the half-bridge wire-bondless power module.

The module has been designed and manufactured to provide a power electronic building block (PEBB) for a 99% efficient 3-phase power converter with a power-to-weight ratio of 10 kW/kg. This means that for output power of 45 kW, maximum three-phase power loss of 450 W (150 W per phase/leg) is the allowable limit.

To reduce the complexity and cost of the real-time thermal model, an experimental combination with one power module and two power resistors are utilized, instead of three parallel power modules. Both the two resistors and power module are mounted on the heatsink via thermal pad (Kerafol KERATHERM Thermal Pad $6.5W/mK$ Gap Fill) to ensure good heat transfer.

4.5.2 Force-Air Cooling System

The heatsink used in these experiments is a typical hollow-fin heatsink (Fischerelectronik) with an integrated axial fan, as shown in Figure 4.9.

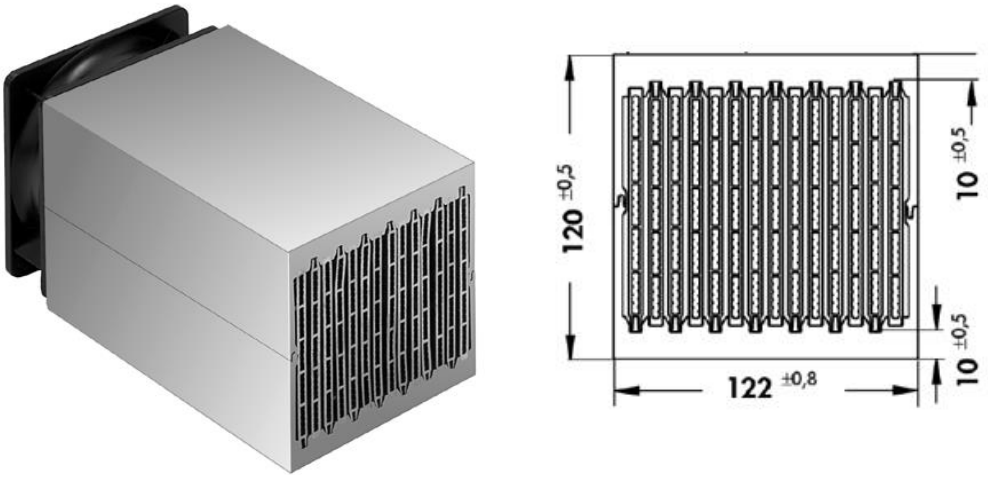

(a) The prototype of heatsink (b) Cross-section layout of heatsink

Figure 4.9. Hollow-fin cooling aggregates.

The technical data of the fans is shown in the following Table 4.3.

Table 4.3 Technical data of the fans	
Dimensions	$119 \times 119 \times 38mm$
Voltage	230V AC

Power input	19W
Max. air flow	$160m^3/h$
Temperature range	$-40°\text{C} \ldots + 85°\text{C}$
Noise level	47 dB(A)
Rated speed	2650/min
Weight	550g

The outlet air temperature of heat sink needs be limited in 55-65℃ with an inlet air temperature of 40℃. The fluid heat transfer equation is expressed in as follows

$$\Delta Q = c_{air} m \Delta T \tag{4.4.1}$$

Where

- ΔQ : The heat flowing into the heat sink [450W].
- $\dot{m}$: mass flow rate of air [kg/s].
- c_{air} : The specific heat of air $1.01e^3$ [$J/(kg \cdot K)$].
- ΔT: The air temperature increased by heat flow [℃].

With a maximum three-phase power loss of 450 W, inlet air flow with an approximate range of 1m/s to 2m/s is suitable for the system cooling.

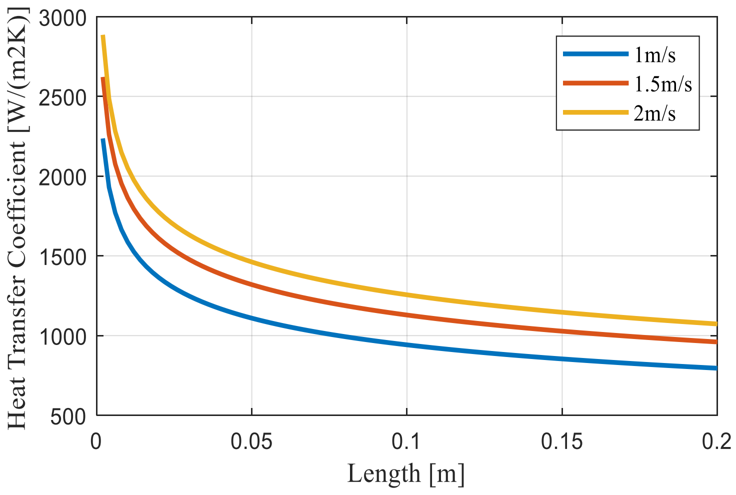

Figure 4.10. Heat transfer coefficient along the axial direction of the air flow.

Applying the numerical model proposed in Section 3.3, the resulting heat transfer coefficient as function of the axial distance from the inlet for the heatsink is shown in Figure 4.10 for three different values of air mass flow from 1m/s to 2m/s.

4.5.3 Experimental Setup

Figure 4.11 shows the experimental setup used to evaluate the discussed models. In this configuration, two resistors were used in place of power modules to simplify the construction. Both the resistors and power module are connected to DC power supplies.

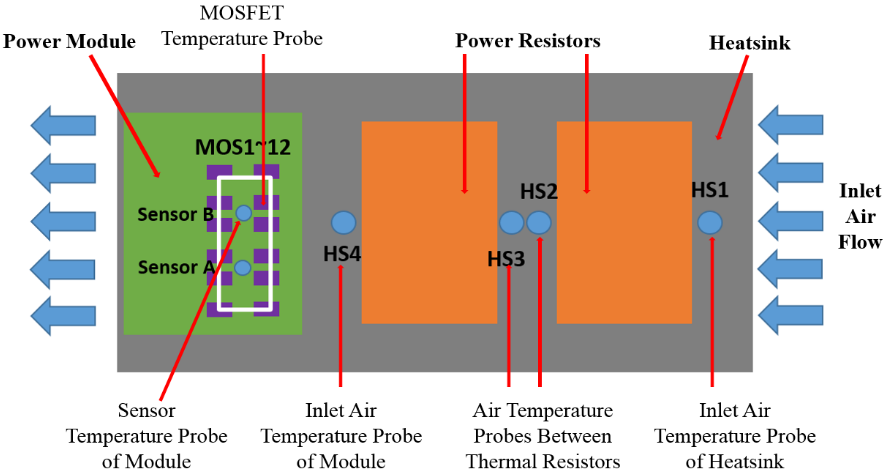

(a) Thermal model design

(b) Figure of power module and gate drive board

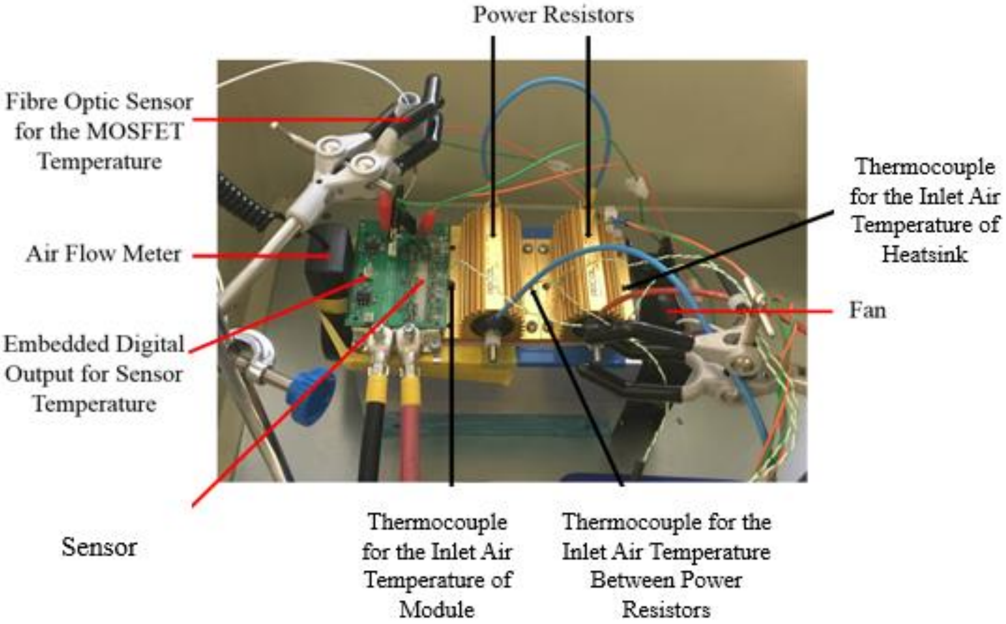

(c) General view of experimental rig

Figure 4.11. Experimental layout.

As shown in Figure 4.11(a), the rig includes four thermocouples, positioned in the airflow at the inlet, outlet and in between the modules, allowing the air temperature to be monitored, although only the inlet air temperature measured by HS4 is used as the input ambient temperature. The PICO thermocouple system is shown in Figure 4.12.

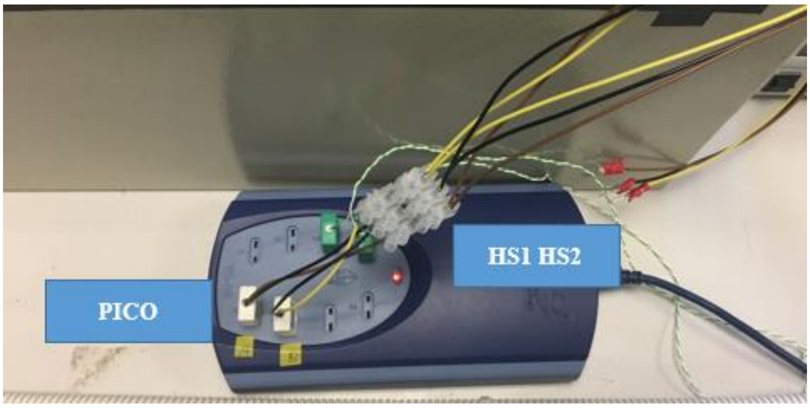

Figure 4.12 PICO thermocouple System

As shown in Figure 4.11(b), the gate driver adapter board mounted on the power module features a cutout that allows direct visual and physical access to the three of the twelve MOSFETs in the module. The top surface of the module is coated with Boron-Nitride paint to provide a high emissivity surface for the thermal camera. Thermal camera is utilized for steady-state temperature measurement. The thermal camera used is a Flir ets320 as shown in Figure 4.13. It has a refresh rate of 9Hz and the accuracy is +/-3%.

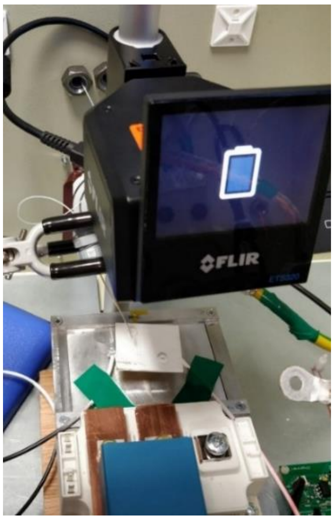

Figure 4.13 Thermal Camera

The Fibre Optic temperature measurement system (Opsens Coresens GSX-2-N module and an OTF-F temperature sensor) is used to monitor MOSFET die temperature directly for comparison with the MOR model predictions and validation of the proposed methodology [141]. The view of the devices and its quick test result is shown in Figure 4.14.

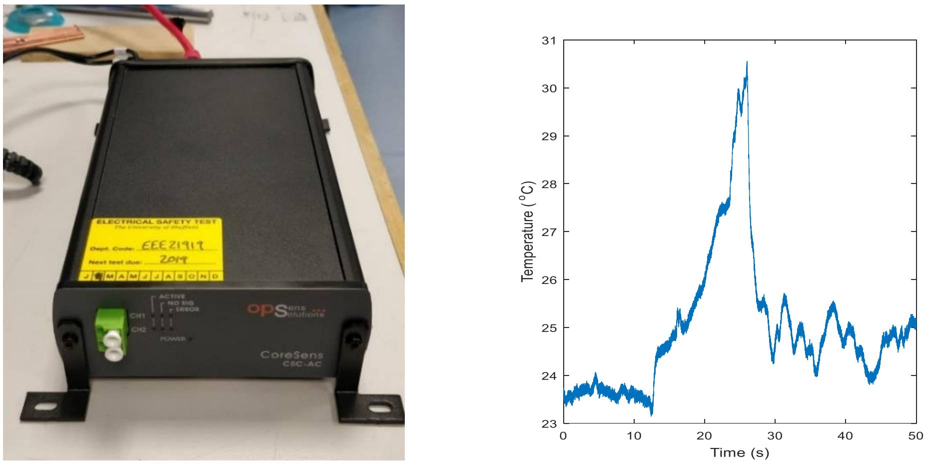

(a) General View of Fibre Optic system

(b) Quick input test moving hand closer/further from probe tip

Figure 4.14 Fibre Optic System

The Opsens Fibre Optics sensors can be directly placed in contact on the surface of the MOSFETs. Fibreoptic monitoring system is precise and tailored for high speed measurement, especially in thermal monitoring. The Fibre optic sensor has a very high accuracy of ±0.3°C and therefore error bars in the measurement are extremely small.

4.5.4 Experimental Data and Simulation Results

The influence of convective boundary condition in experiment is shown in Figure 4.15. The convective boundary condition is affected by the air flow rate. Based on the same input power and experiment layout, the steady state temperature captured by thermal camera can shows the effect of the change of the air flow rate on convective boundary condition. With an increasing air flow rate from 1m/s to 1.5m/s, the maximum temperature of the power module in steady state reduces from 103℃ to 94.1℃.

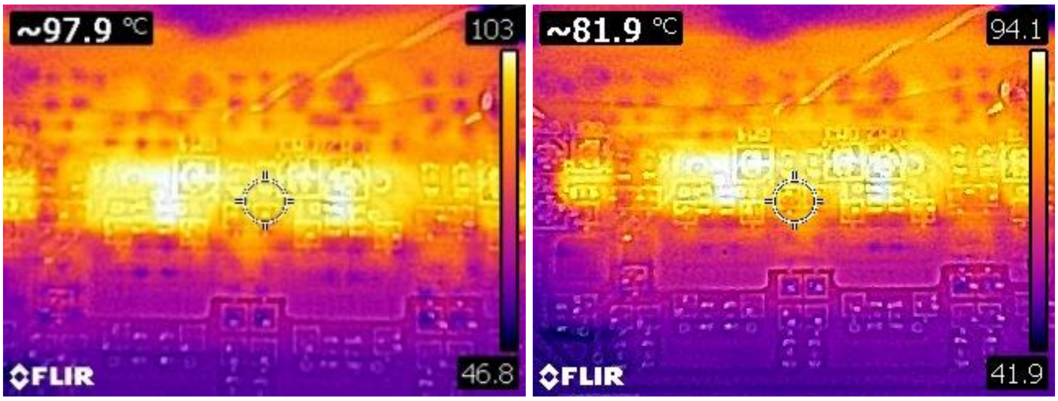

(a) 1m/s for peak current of 70A

(b) 1.5m/s for peak current of 70A

Figure 4.15. Steady-State temperature from thermal camera.

The proposed MOR method is applied to the system. Figure 4.16 illustrates surface temperature responses of the 11-th MOSFET identified in Figure 4.8 calculated by reduced order simulation and compared to transient results obtained with experiment and commercial FE software ANSYS.

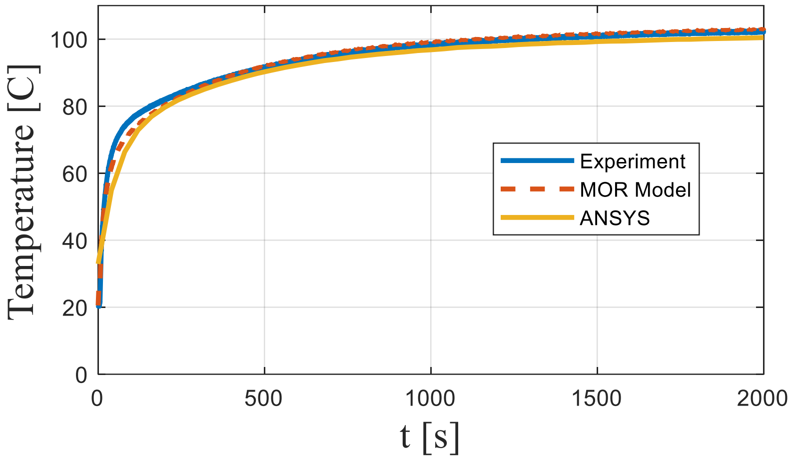

(a) 1m/s for peak current of 90A

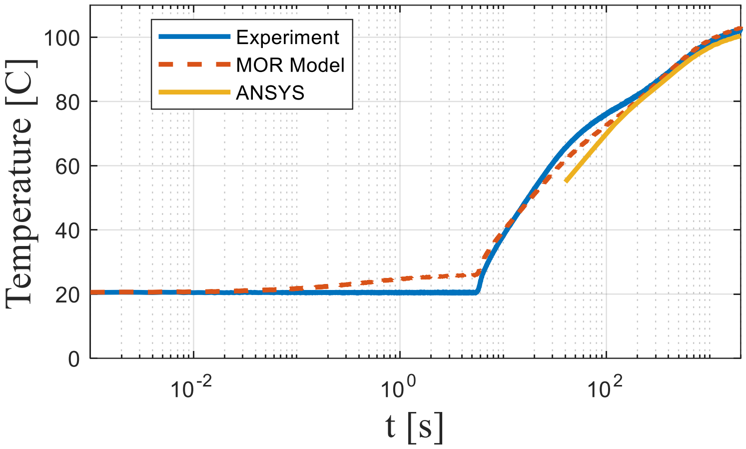

(b) Log plot of (a)

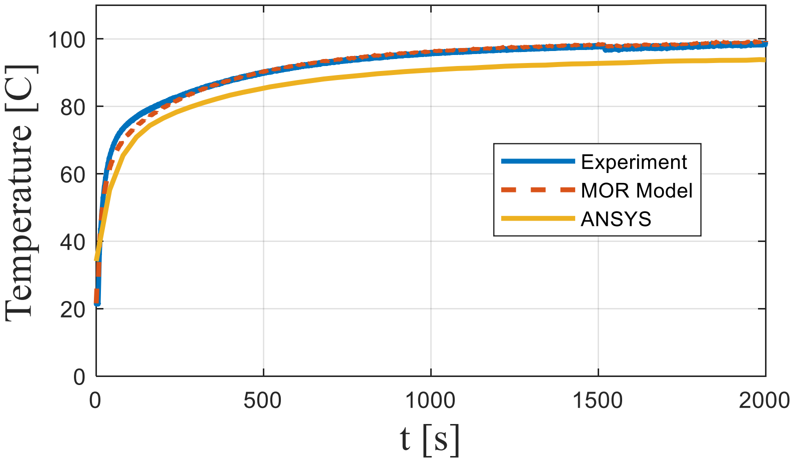

(c) 1.5m/s for peak current of 90A

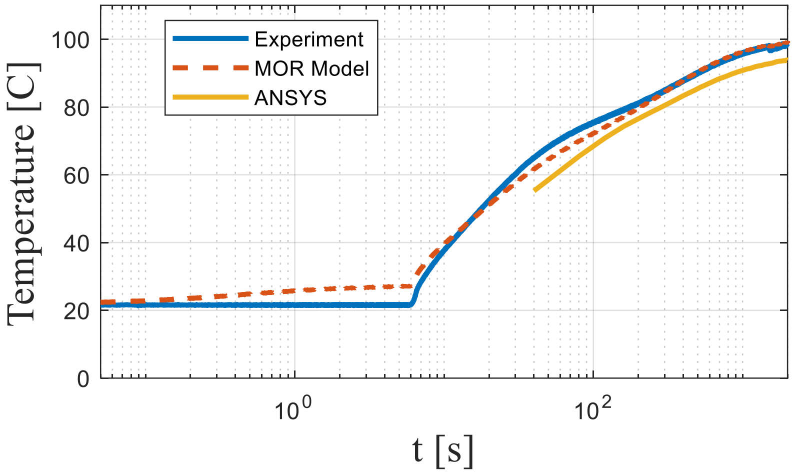

(d) Log plot of (c)

Figure 4.16. Comparison between experimental data and estimated values.

Compared with ANSYS, both the complex geometry structure of heatsink and air force cooling can be considered in reduced order model, resulting a better data agreement.

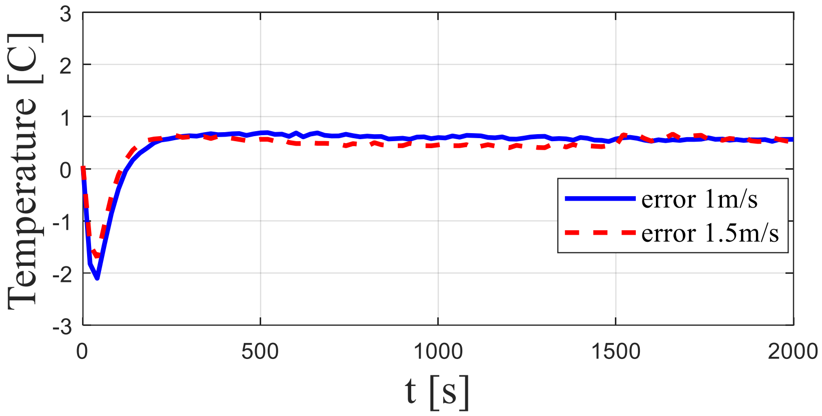

Figure 4.17. Transient error of MOR compared with experiment data.

The dynamic and steady state errors identified in Figure 4.17 are less than 1%, confirming the accuracy of the proposed MOR method. It should be noted that the slight error in the initial stage shown in Figure 4.17, mainly comes from a few second delay in the instrument operation and temperature measurement during the experimental process.

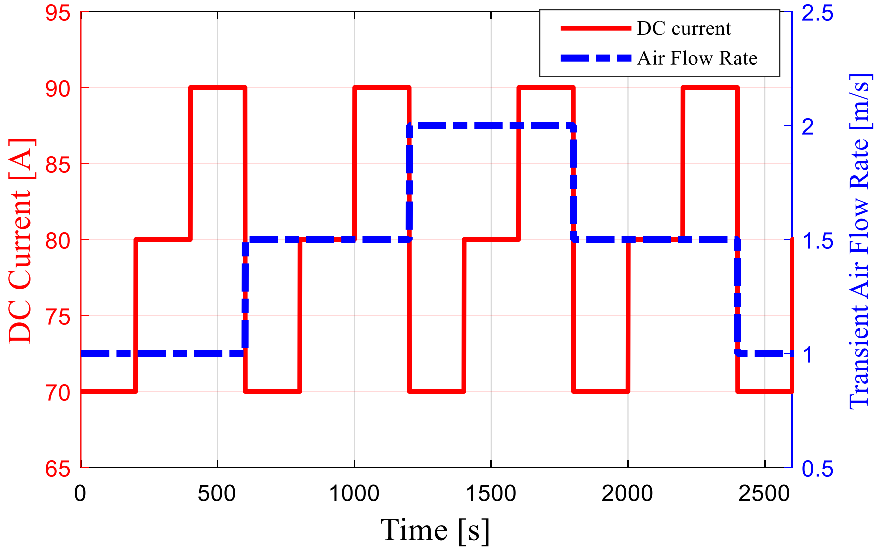

(a) Module current and transient air flow rate

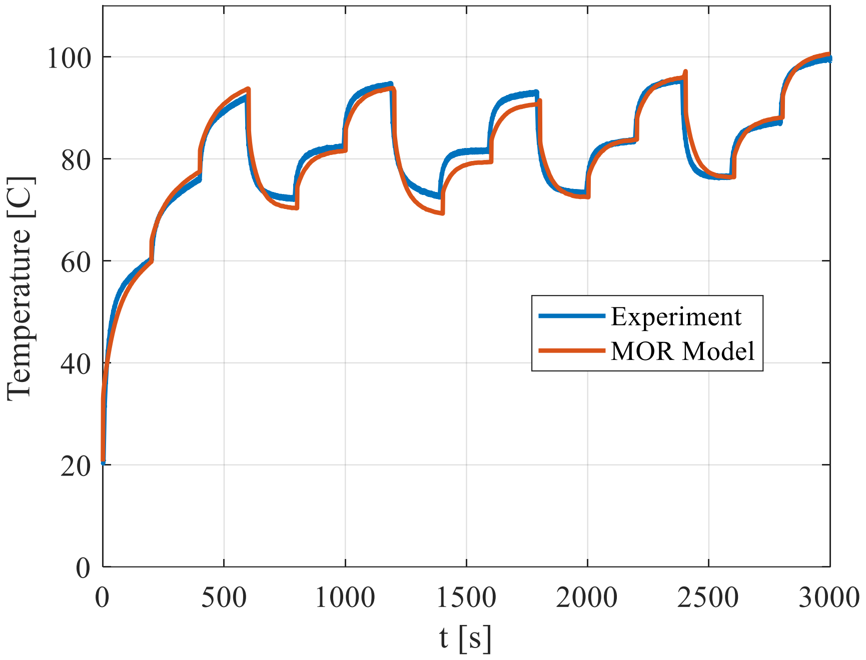

(b) Transient thermal response from experiment and MOR model.

Figure 4.18. Comparison between experimental data and estimated values.

In Figure 4.18, a more complex boundary condition is introduced to test the accuracy of the parametric MOR numerical model. In this test the air-flow velocity and the DC current are variable following the profiles shown in Figure 4.18(a). A good accuracy is demonstrated for the reduced order model, confirming its transient accuracy and robustness.

The discretization employed in the full order model results in a system with 48595 nodes, while the reduced order has 12 states corresponding to 12 temperature nodes per MOSFET. On the same computer and with the same mesh size, ANSYS takes over 500 minutes while the reduced-order simulation only takes about 5 seconds.

4.6 Conclusion

In this chapter, a novel multi-parameter order reduction is developed and applied to a power module with forced-air-cooling systems. The multi-moment matching technique is used to preserve in the reduced order a number of parameters, making calculations in variable operating conditions significantly more efficient. An example of a power module cooling system with different mass air flow rates is reported and experimental data proves the accuracy of this reduced-order numerical model. A significant increase in computational efficiency is demonstrated resulting in faster calculation time and memory requirements.

The method can have applications at both the design stage and during operation of power conversion systems. Optimization of layout in power electronics modules and converters design might require many iterations using different values of parameters e.g. of materials or cooling conditions. With the proposed parametric MOR such applications can be greatly simplified as the reduced order model conserves dependency on parameters which can be simply modified at each iteration without requiring additional computations. Thanks to its low computational complexity, the resulting reduced order model can also be used in real-time applications as an observer for temperature estimation of power devices during converter operation.

Chapter 5 Reduced-Order Thermal Observer for Power Modules

5.1 Introduction

Accurate knowledge of power device die temperature is critical to the implementation of control and health management algorithms which have been proposed to monitor and extend the lifetime of power modules under in-service conditions. Temperature variation can also be reduced using dynamically controlled cooling. To achieve this, a suitable model of the cooling system behaviour must be available. To perform this analysis, a range of design variables, such as inlet air temperature, velocity of the air flow, material composition of the power modules, and the geometry of the assembly, must be considered.

Examples of methods used to perform thermal analysis in power electronics include computational fluid dynamics (CFD), compact thermal model, and empirical lumped element model. Of the methods above, CFD can be used to simulate conductive and convective heat transfer simultaneously, providing the most accurate and detailed temperature distribution of the power electronic system under consideration. Although accurate thermal models of power electronics assemblies based on CFD are widely available, their computational complexity hinders the application in real-time temperature monitoring applications.

This chapter proposes a reduced order state space observer to provide a real-time estimation of temperature in power electronics modules. The observer is coupled with a disturbance estimator, to minimize the error caused by uncertainties in the model and unknown operating conditions.

5.2 State Space Thermal Modelling

In Section 3.4, the R_i, C_i parameters have been estimated using a parameters identification procedure based on CFD analyses. The obtained parameters can be are listed as follows

$$C_1 \frac{dX_1}{dt} + \frac{X_1}{R_1} = P_{loss} - \frac{X_1 + X_2 + X_3 - X_4}{R_{jB}} \tag{5.2.1}$$

where $X_{1,\ldots,4}$ are the temperature rises across the respective capacitances. Then the above equation can be rewritten as

$$\frac{dX_1}{dt} = -\frac{1}{C_1}\left(\frac{1}{R_1} + \frac{1}{R_{jB}}\right)X_1 - \frac{1}{C_1}\frac{X_2}{R_{jB}} - \frac{1}{C_1}\frac{X_3}{R_{jB}} + \frac{1}{C_1}\frac{X_4}{R_{jB}} + P_{loss} \tag{5.2.2}$$

Similarly

$$\frac{dX_2}{dt} = -\frac{1}{C_2}\frac{X_1}{R_{jB}} - \frac{1}{C_2}\left(-\left(\frac{1}{R_2} + \frac{1}{R_{jB}}\right)X_2\right) - \frac{1}{C_2}\frac{X_3}{R_{jB}} + \frac{1}{C_2}\frac{X_4}{R_{jB}} + P_{loss} \tag{5.2.3}$$

$$\frac{dX_3}{dt} = -\frac{1}{C_3}\frac{X_1}{R_{jB}} - \frac{1}{C_3}\frac{X_2}{R_{jB}} - \frac{1}{C_3}\left(-\left(\frac{1}{R_3} + \frac{1}{R_{jB}}\right)X_3\right) + \frac{1}{C_3}\frac{X_4}{R_{jB}} + P_{loss} \tag{5.2.4}$$

$$\frac{dX_4}{dt} = \frac{1}{C_4}\frac{X_1}{R_{jB}} + \frac{1}{C_4}\frac{X_2}{R_{jB}} + \frac{1}{C_4}\frac{X_3}{R_{jB}} - \frac{1}{C_4}\left(-\left(\frac{1}{R_4} + \frac{1}{R_{jB}}\right)X_4\right) \tag{5.2.5}$$

Using the above derivations, the thermal model can be written in the state-space form as:

$$\begin{aligned} \dot{x} &= Ax + Bu \\ y &= Cx \end{aligned} \tag{5.2.6}$$

Where

- x: The vector of states
- y: The state outputs (T_j and T_B)
- u: The vector of inputs
- A: The state matrix
- B: The input matrix
- C: The observation matrix

The matrices of equation (5.2.6) are given by

$$A = \begin{bmatrix} A_{11} & A_{12} \\ A_{21} & A_{22} \end{bmatrix} \qquad B = \begin{bmatrix} B_1 \\ B_2 \end{bmatrix}$$

$$C = \begin{bmatrix} 1 & 1 & 1 & 0 \\ 0 & 0 & 0 & 1 \end{bmatrix} \qquad u = \begin{bmatrix} P_{loss} \\ T_{air} \end{bmatrix}$$

$$x = \begin{bmatrix} x_1 \\ x_2 \\ x_3 \\ \ldots \\ x_4 \end{bmatrix} = \begin{bmatrix} x_{MOS} \\ \cdots \\ x_{Sensor} \end{bmatrix} \qquad y = \begin{bmatrix} T_j \\ T_B \end{bmatrix} \tag{5.2.7}$$

Where

- $$A_{11} = \begin{bmatrix} -\frac{1}{C_1}\left(\frac{1}{R_1} + \frac{1}{R_{jB}}\right) & -\frac{1}{C_1 R_{jB}} & -\frac{1}{C_1 R_{jB}} \\ -\frac{1}{C_2 R_{jB}} & -\frac{1}{C_2}\left(\frac{1}{R_2} + \frac{1}{R_{jB}}\right) & -\frac{1}{C_2 R_{jB}} \\ -\frac{1}{C_3 R_{jB}} & -\frac{1}{C_3 R_{jB}} & -\frac{1}{C_3}\left(\frac{1}{R_3} + \frac{1}{R_{jB}}\right) \end{bmatrix}$$
- $$A_{21} = \begin{bmatrix} \frac{1}{C_4 R_{jB}} & \frac{1}{C_4 R_{jB}} & \frac{1}{C_4 R_{jB}} \end{bmatrix}$$
- $$A_{12} = \begin{bmatrix} \frac{1}{C_1 R_{jB}} & \frac{1}{C_2 R_{jB}} & \frac{1}{C_3 R_{jB}} \end{bmatrix}^T$$
- $$A_{22} = \left[-\frac{1}{C_4}\left(\frac{1}{R_4} + \frac{1}{R_{jB}}\right)\right]$$
- $$B_1 = \begin{bmatrix} \frac{1}{C_1} & 0 \\ \frac{1}{C_2} & 0 \\ \frac{1}{C_3} & \frac{1}{C_3}\left(\frac{1}{R_3} + \frac{1}{R_{jB}}\right) \end{bmatrix}$$
- $$B_2 = \left[0 \quad \frac{1}{C_4}\left(\frac{1}{R_4} + \frac{1}{R_{jB}}\right)\right]$$

5.3 Reduced Order Observer of Thermal Model

The model (5.2.6) could be used as an open-loop estimator of device temperature if the inputs, i.e. ambient temperature and power losses, and the parameters of the network are accurately estimated. However, this accurate knowledge of environmental conditions and parameters is rarely possible in practical applications.

This section proposes the use of an observer which provides a correction feedback mechanism which tries to correct the errors due to imprecise knowledge of conditions, inputs and parameters, e.g. caused by changes in the inlet air temperature and airflow rate and modelling errors e.g. in the estimated power loss and estimated thermal parameters.

A full-order observer, based on the thermal model (5.2.6), can be written in state-space form as:

$$\begin{aligned} \dot{\hat{x}}(t) &= A\hat{x}(t) + Bu(t) + L(y(t) - \hat{y}(t)) \\ \hat{y}(t) &= C\hat{x}(t) \end{aligned} \tag{5.3.1}$$

Where

- $\hat{x}(t)$: The estimated state of the system.
- $\hat{y}(t)$: The observer output (estimated MOS junction temperature and estimated sensor temperature).
- L: The gain of observer.

An observer is a dynamic system, designed to be an approximate replica of the real system, used to estimate the states of the real system. The observer is driven by the same inputs (MOS power loss and inlet air/ambient temperature) as the real system, with an additional correction term that is derived from the difference between the actual measurement y from the real system and predicted output $\hat{y}$ derived from the observer. The correction term is composed of the error $y - \hat{y}$ and feedback matrix or gain. Consequently, an observer uses the difference between the measurement and prediction to improve prediction accuracy.

Due to the fact that there are no temperature sensors on the MOS chip, the state temperature cannot be measured directly. However, the module does incorporate two PT1000 thermistors used as temperature sensors attached to the DBC substrate. Therefore, the temperature of this sensor can be directly measured and does not need to be estimated. In this case, a reduced-order observer will suffice. For the thermal model analysed in the section, the full system has 4 states $(X_1, \dots, X_4)$ however, one of them (X_4) can be measured directly as it represents the sensor temperature, therefore a reduced order observer with only 3 states is necessary. The derivation of the reduced-order observers is obtained by partitioning the state vector into two sub-states:

$$x = \begin{bmatrix} x_{MOS} \\ \cdots \\ x_{Sensor} \end{bmatrix}$$

$$x_{Sensor} = y = Cx = \hat{x}_{sensor} \tag{5.3.2}$$

Where

- $C = [0 \quad I]$: The observation vector (of dimension m=1).
- x_{MOS}: The component of the state vector that cannot be measured directly (of dimension 3).

The assumption that $y = x_{Sensor}$ makes the resulting equations simpler, but it is not necessary. Equivalent results can be obtained for any observation matrix C of rank m. In terms of x_{MOS} and x_{Sensor} the plant dynamics are written as

$$\begin{gathered} \dot{x}_{MOS} = A_{11}x_{MOS} + A_{12}x_{Sensor} + B_1u \\ \dot{x}_{Sensor} = A_{21}x_{MOS} + A_{22}x_{Sensor} + B_2u \end{gathered} \tag{5.3.3}$$

$$\hat{x}_{sensor} = x_{Sensor} = y \tag{5.3.4}$$

A block-diagram representation of the reduced-order observer is shown in Figure 5.1.

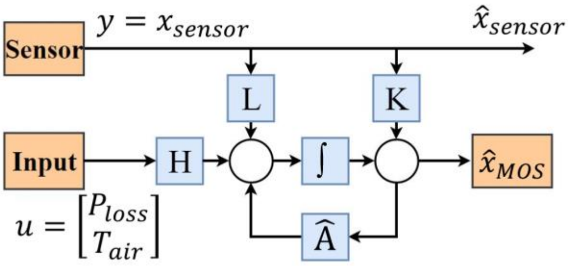

Figure 5.1. Reduced-order observer.

For the remaining sub-states, we define the reduced-order observer by:

$$\hat{x}_{MOS} = Ky + z \tag{5.3.5}$$

Where z is the state of a system of order $m = 3$:

$$\dot{z} = \hat{A}z + Ly + Hu \tag{5.3.6}$$

It is necessary to ensure the convergence of the temperature estimation error $e_{MOS} = x_{MOS} - \hat{x}_{MOS}$ to zero. From the above equations:

$$\dot{e}_{MOS} = \hat{A}e_{MOS} + \left(A_{11} - KA_{21} - \hat{A}\right)x_{MOS} + \begin{pmatrix} A_{12} - KA_{22} \\ -L + \hat{A}K \end{pmatrix} x_{Sensor} + (B_1 - KB_2 - H)u \tag{5.3.7}$$

A sufficient condition for the error to converge to zero is to choose the matrices to satisfy

$$\begin{aligned} \hat{A} &= A_{11} - KA_{21} \\ L &= A_{12} - KA_{22} + \hat{A}K \\ H &= B_1 - KB_2 \end{aligned} \tag{5.3.8}$$

When the conditions shown in (5.3.8) are all satisfied, the error in estimation of x_{MOS} is given by

$$\dot{e}_{MOS} = \hat{A}e_{MOS} \tag{5.3.9}$$

Therefore the gain matrix K should be chosen to make the eigenvalues of $\hat{A} = A_{11} - KA_{21}$ lie in the open left-half plane. Additionally, A_{11} and A_{21} in the reduced-order observer take the roles of A and C in the full-order observer; once the gain matrix K is chosen, there is no further freedom in the choice of L and H.

5.4 Time-Domain Disturbance Estimation

Device junction temperature depends not only on power dissipation but also on environmental conditions such as changes in ambient temperature, e.g. caused by heating of nearby devices mounted on the same cooling system, or changes in coolant flow rate. Changes in inlet air temperature and air flow will introduce an error between the estimated and real MOSFET temperature. To reduce estimation errors between the real value and reference values, a state observer may be used. Power losses are assumed to be subject to an estimation error, a disturbance estimation will be introduced to estimate and compensate this error. The so-called unknown input observer (UIO) have been reviewed in Chapter 2. In this case, a typical state space model used for the UIO is

$$\begin{aligned} \dot{x} &= Ax + Bu + B_d d \\ y &= Cx \end{aligned} \tag{5.4.1}$$

Where

- x: The vector of states
- y: The state outputs (T_j and T_B)
- u: The vector of known inputs
- d: The vector of unknown inputs
- A: The state matrix
- B: The input matrix of known inputs
- B_d: The input matrix of unknown inputs
- C: The observation matrix

It is assumed that the vector of inputs is unknown. Consequently, an UIO design is investigated for a linear system in equation (5.4.1). The general expression of the UIO is

$$\begin{aligned} \dot{z} &= -NB_d(z + Nx) - N(Ax + Bu) \\ \hat{d} &= z + Nx \end{aligned} \tag{5.4.2}$$

Where

- $B_d = \begin{bmatrix} \frac{1}{C_1} & \frac{1}{C_2} & \frac{1}{C_3} & 0 \end{bmatrix}^T$
- N: The observer gain matrix need be designed.

Consequently, the estimation error is

$$e = \hat{d} - d \tag{5.4.3}$$

And error dynamic is

$$\begin{aligned} \dot{e} &= \dot{z} + N\dot{x} - \dot{d} \\ &= -NB_d\hat{d} - N(Ax + Bu) + N(Ax + Bu + B_d d) - \dot{d} \\ &= -NB_d(\hat{d} - d) - \dot{d} = -NB_d e - \dot{d} \end{aligned} \tag{5.4.4}$$

Where $\dot{d}$ is zero in this model and the error dynamic equation can be rewritten as

$$\dot{e} = -NB_d e \tag{5.4.5}$$

It is shown that the disturbance estimation error system is stable if the observer gain matrix is chosen to make $-NB_d$ stable, i.e. a matrix whose eigenvalues have strictly negative real part. When the disturbance estima1tion error system reaches steady state, $\dot{e}$ equals to zero and consequently, e equals to zero.

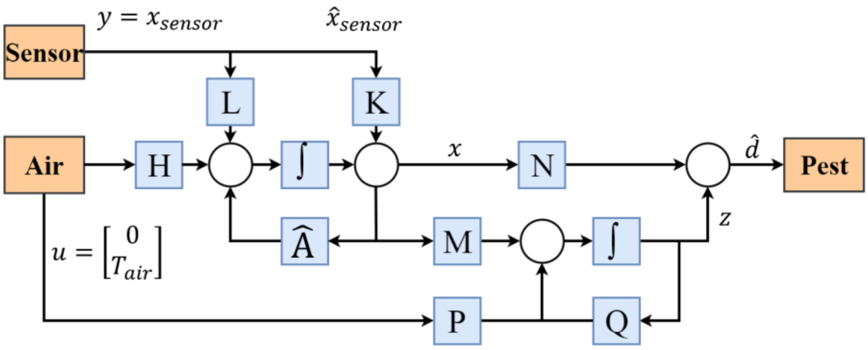

Figure 5.2. Thermal model with UIO disturbance estimation.

The concept of disturbance estimation is illustrated in the block diagram of Figure 5.2. Based on equation (5.4.2), the relative parametric matrices are:

$$\begin{gathered} M = -NB_d N - NA \\ P = -NB \\ Q = -NB_d \end{gathered} \tag{5.4.6}$$

To make the concept of disturbance estimation clearer, a simplified version of Figure 5.2 can be introduced. As shown in Figure 5.3, the thermal model used to calculate estimated power disturbance is an open-loop model, which can be divided into two sections. The first stage is generation of state vectors x via system matrices $H\ L\ \hat{A}$ and K and input vectors are sensor temperature T_{sensor} and inlet air temperature T_{air}. Then the obtained state vectors x and inlet air temperature T_{air} are applied in the block of disturbance estimation consisting $M\ N\ P$ and Q for the estimation of power loss P_{est}.

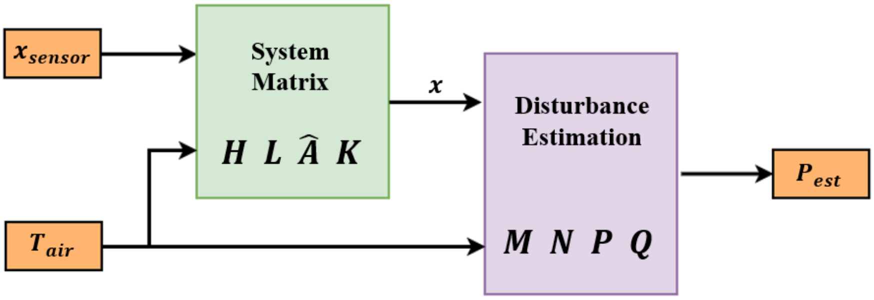

Figure 5.3. Flow chart of thermal model with UIO disturbance estimation.

It is assumed that the input power loss is unknown and therefore can be assumed to be equal to the output of the disturbance estimation P_{est}. The air inlet temperature at the input duct of the heatsink is measured and fed as an input to the observer in Figure 5.2. The estimated loss P_{est}, at the output of the disturbance estimation in Figure 5.2 is fed back as an input to the reduced-order observer in Figure 5.1.

5.5 Simulation and Programing

The Simulink model of power disturbance estimation is shown in Figure 5.4.

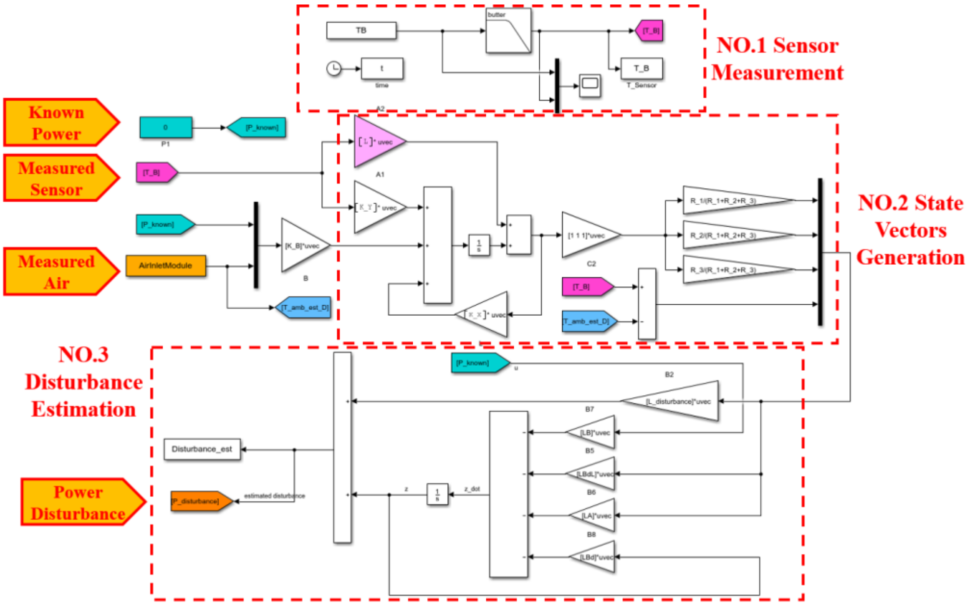

Figure 5.4. The Simulink model of power disturbance estimation.

The Simulink model of reduced order observer model is shown in Figure 5.5.

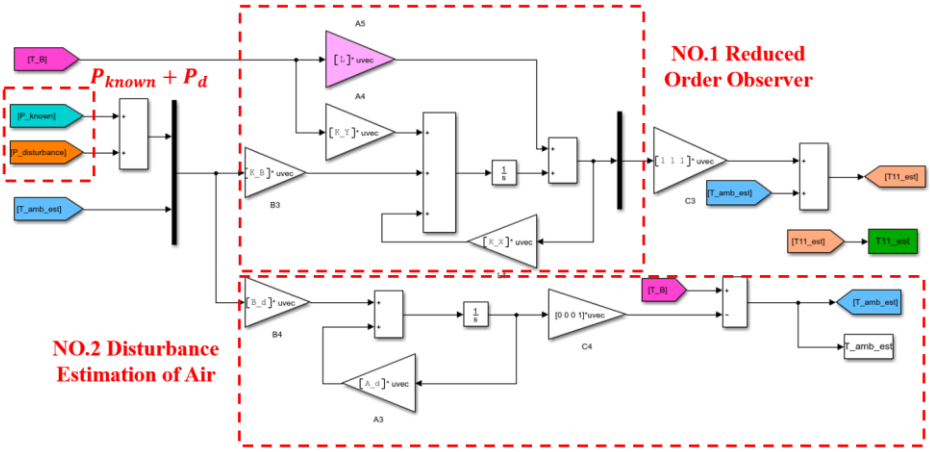

Figure 5.5. The Simulink model of reduced order observer model.

The observer model is generated and shown according to the following procedure.

- State space matrices of Block No.2 in Figure 5.4 and Block No.1 in Figure 5.5.

```
% State-Space Matrices in Continuous Domain
% state matrix
A = [-(1/(R_1*C_1)+1/(R_JB*C_1)),-1/(R_JB*C_1),-1/(R_JB*C_1),1/(R_JB*C_1);
      -1/(R_JB*C_2),-(1/(R_2*C_2)+1/(R_JB*C_2)),-1/(R_JB*C_2),1/(R_JB*C_2);
      -1/(R_JB*C_3),-1/(R_JB*C_3),-(1/(R_3*C_3)+1/(R_JB*C_3)),1/(R_JB*C_3);
       1/(R_JB*C_4),1/(R_JB*C_4),1/(R_JB*C_4),-(1/(R_4*C_4)+1/(R_JB*C_4))];
% input matrix
B = [1/C_1,0;
     1/C_2,0;
     1/C_3,1/(C_3*R_3)+1/(C_3*R_JB);
     0,1/(C_4*R_4)+1/(C_4*R_JB)];
% output matrix
C = [1,1,1,0;
     0,0,0,1];
```

- Reduced order observer of Block No.2 in Figure 5.3 and Block No.1 in Figure 5.4.

```
%   Reduced Order Observer
A_uu = A(1:3,1:3);
A_au = A(4:4,1:3);
A_ua = A(1:3,4:4);
A_aa = A(4:4,4:4);
B_u = B(1:3,1:2);
B_a = B(4:4,1:2);
% calculate eigenvalues
eig_A_uu = eig(A_uu);
op1 = eig_A_uu(1)*8;
op2 = eig_A_uu(2)*8;
op3 = eig_A_uu(3)*8;
% calculating gain matrix
L = acker(A_uu',A_au',[op1 op2 op3])';
% state matrix for unknown states for a reduced order observer
K_X = A_uu-L*A_au;
```

```
% input state matrix for unknown states
K_B = B_u-L*B_a;
% output state matrix for unknown states
K_Y = A_ua-L*A_aa;
```

- Power disturbance estimation of Block No.3 in Figure 5.3.

```
%% Disturbance estimation (Power)
A_disturbance = A;
B_disturbance = [1/C_1;
                 1/C_2;
                 1/C_3;
                 0];
C_disturbance = [0,0,0,1];
B_d_disturbance=B_disturbance;
L_disturbance=[-4 1.5 -3 2]*0.1;
LBdL=L_disturbance*B_d_disturbance*L_disturbance;
LA=L_disturbance*A_disturbance;
LB=L_disturbance*B_disturbance;
LBd=L_disturbance*B_d_disturbance;
```

- Air disturbance estimation of Block No.2 in Figure 5.4

```
%% Disturbance observer (Air)
A_d_air = A;
B_d_air = [1/C_1,0;
           1/C_2,0;
           1/C_3,1/(C_3*R_3)+1/(C_3*R_JB);
           0,1/(C_4*R_4)+1/(C_4*R_JB)];
C_d_air = [0,0,0,1];
```

5.6 Experimental Validation I

The experimental validations of this chapter can be divided into two stages. The first stage provides an application of air-force cooling system and Silicon Carbide (SiC) MOSFET-based half-bridge with DC power supply, having the same experimental layout with that in Chapter 4.

Figure 5.6 shows the experimental design used to evaluate the discussed models. In this configuration, two resistors were used in place of power modules to simplify the construction. Both the resistors and power module are connected to DC power supplies. Both the two resistors and the power module are mounted to the heatsink via thermal pad (Kerafol KERATHERM Thermal Pad 6.5W/mK Gap Fill) to ensure good heat transfer.

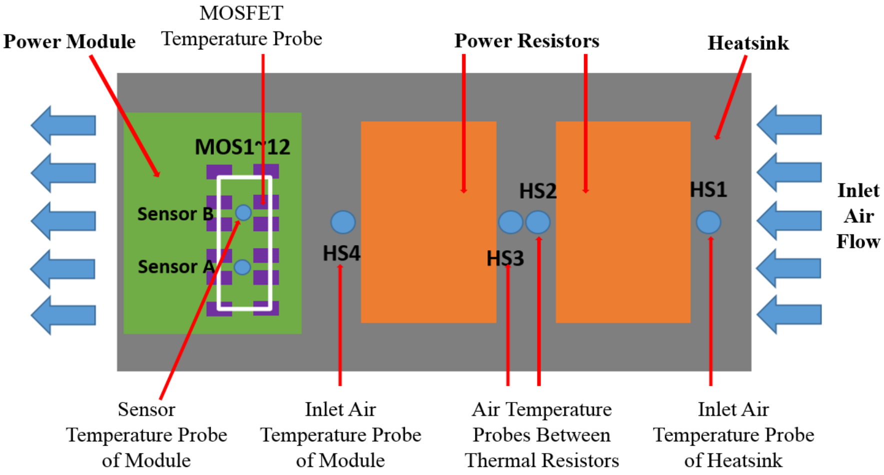

Figure 5.6 Thermal model design

The two embedded temperature sensors A and B within the module are also monitored, one of which is the input variable of the reduced order observer in Section 5.3. The rig includes four thermocouples, positioned in the airflow at the inlet, outlet and in between the modules, allowing the air temperature to be monitored, although only the inlet air temperature measured by HS1 is used as the input ambient temperature. Fibre Optic temperature measurement system (Opsens Coresens GSX-2-N module and an OTF-F temperature sensor) is used to monitor MOSFET die temperature directly for comparison with the observer model predictions.

Transient results obtained by testing at different current levels are shown in Figure 5.7. Using the measured inlet ambient temperature, the observer model with disturbance estimation can accurately predict the MOSFET temperature when compared with experimental data under different boundary conditions. This is despite the fact that the model parameters obtained in Section 3.4 are used (which were derived for the same module in a different experimental configuration).

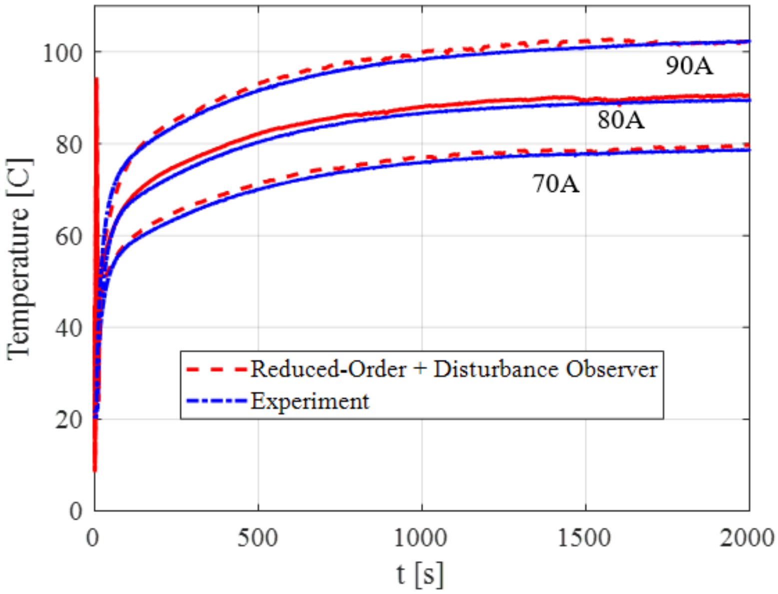

(a) 1m/s for peak current of 70A, 80A and 90A

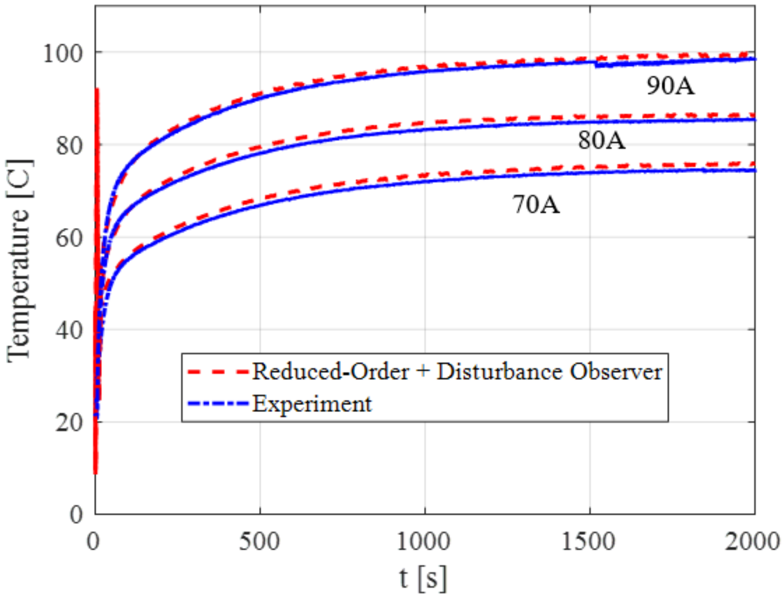

(b) 1.5 m/s for peak current of 70A, 80A and 90A

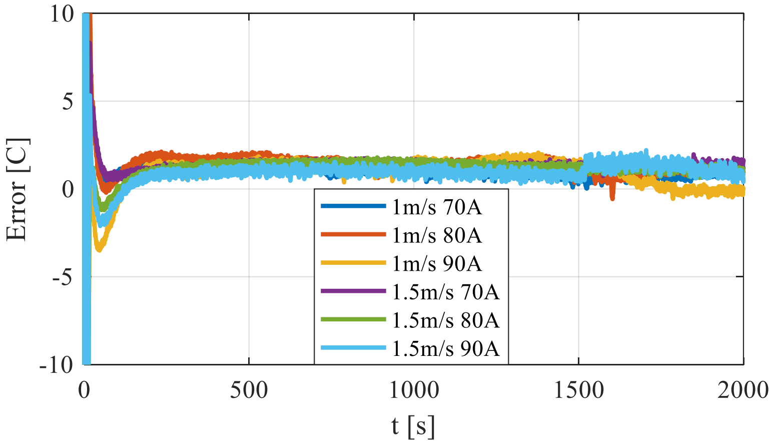

(c) Transient error

Figure 5.7 Comparison between experimental data and estimated values

A more complex boundary condition is introduced to test the accuracy of the observer. In this test the air flow velocity is varied between three different values, furthermore, the DC current is also varied between three levels from 70A to 90A following the profile shown in Figure 5.8.

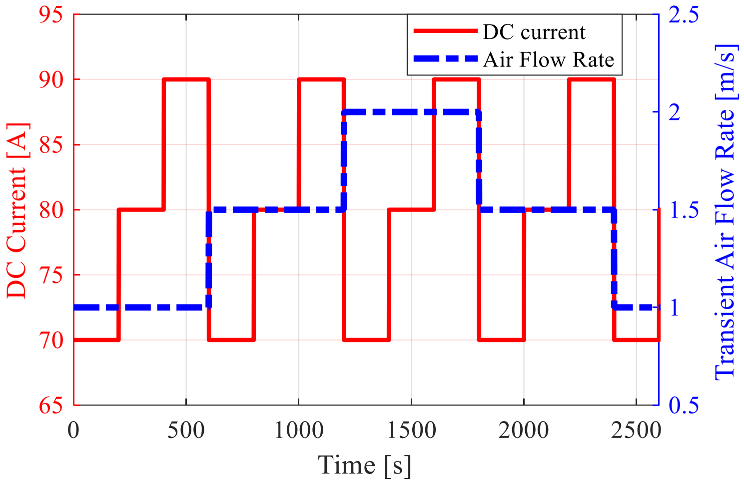

Figure 5.8 Experimental condition with variable DC current and air flow rate.

In Figure 5.9(a), excellent data agreement can be found in the validating process of reduced-order observer model against experiment in the complex condition with time-varying values of power loss and air cooling system, confirming the speed and accuracy of real-time monitoring as well we health management of power modules.

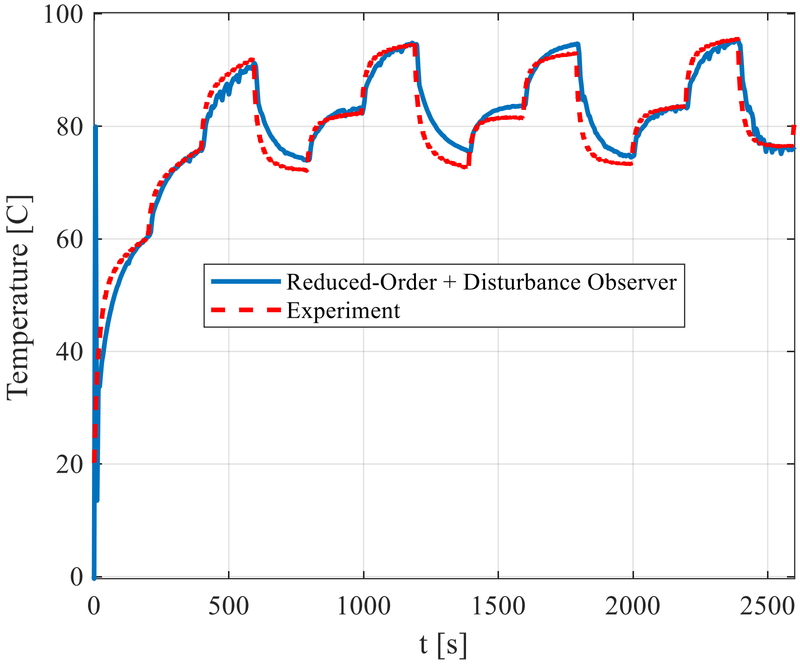

(a) Comparison between estimated and measured MOSFET junction temperature;

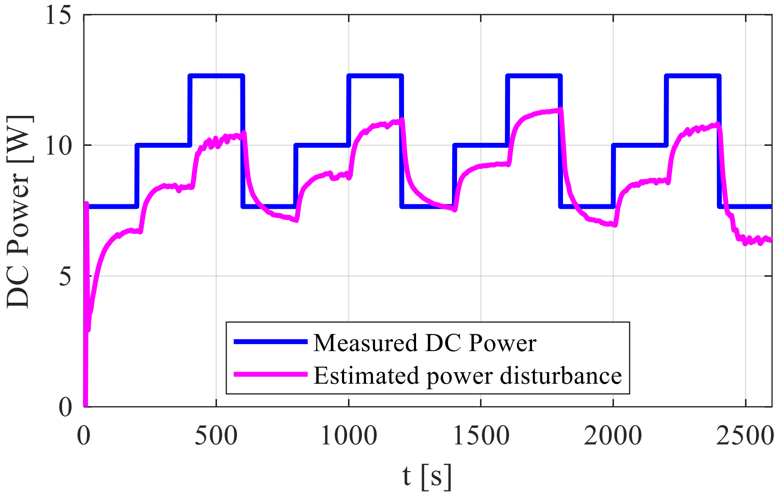

(b) Comparison between estimated power disturbance and measured module power per chip.

Figure 5.9 Comparison between experimental data and estimated values with time-varied DC current and transient air flow rate.

A comparison between estimated power loss P_{est} and measured module power per chip is shown in Figure 5.9(b). The system's dynamic behaviour is affect by both errors in the input values (e.g. estimation of power loss and/or air-cooling boundary conditions) and uncertainties in the parameters of the state-space system. The disturbance observer provides a feedback mechanism to compensate the effects of all the errors combined and cannot provide an accurate separation of the multiple sources of errors. The “estimated power loss” in Figure 5.9(b), is not to be intended as an accurate estimation of the losses but as a compensating power input to the observer, to compensate for all the sources of uncertainties lumped together.

Consequently, the disturbance observer provides a feedback mechanism to compensate the effects of all the errors combined, e.g. due to uncertain loss estimation, ambient conditions and/or parameters. However, the observer cannot provide an accurate separation of the multiple sources of errors and therefore cannot provide an estimation of the losses only.

5.7 Experimental Validation II

The second experimental validation, provides a more challenging application of the proposed method including a relatively complex three-phase converter setup which is fully representative of real industrial applications.

5.7.1 Force-Air Cooling System

This configuration also differs from the first experiment in the manner in which the cooling system was constructed. In this new configuration, each module is mounted to an individual heatsink with ducting being used to enclose these heatsinks and direct the cooling air, with airflow being generated by the fan. The heatsink used in this section is based on around 3 Dynatron K1 heatsinks, as shown in Figure 5.10.

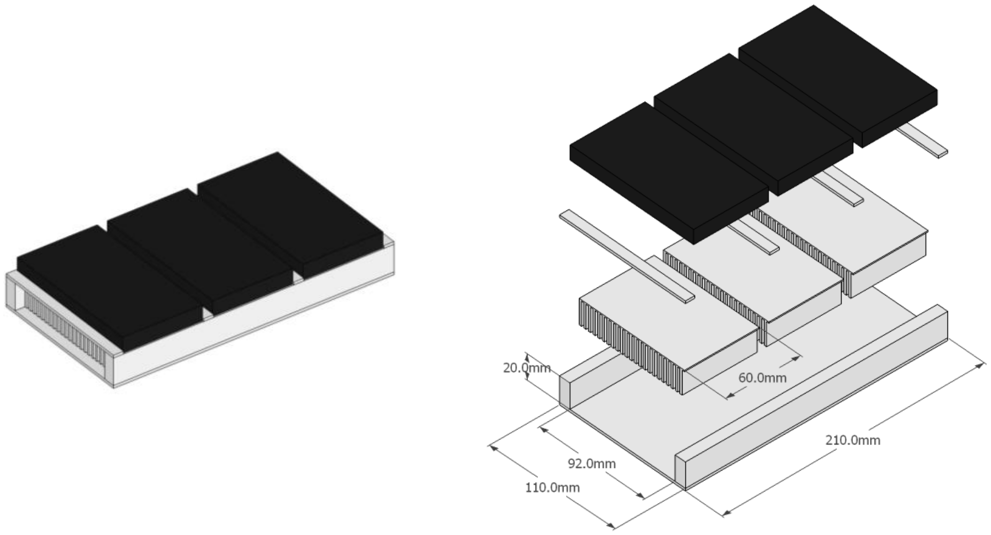

(a) General view (b) Dismantling view

Figure 5.10 Figure of heatsink

Parameters of K1 heatsink is shown in Table 5.1.

Table 5.1 Parameters of K1 heatsink

Length	180 mm (3×60)
Width	95 mm
Baseplate thickness	~4 mm
Number of fins	56
Fin width	~0.6 mm
Fin Spacing	~1.13 mm
Fin Length	~22.5 mm
Total fin path	2570 mm
Total surface area	0.463 m^2

The air-force cooling system is designed as shown in Figure 5.11. The fan is capable of supplying required air flow but not at the required pressure when the heatsink is applied. An additional fan can be placed and operate them in series to increase available pressure.

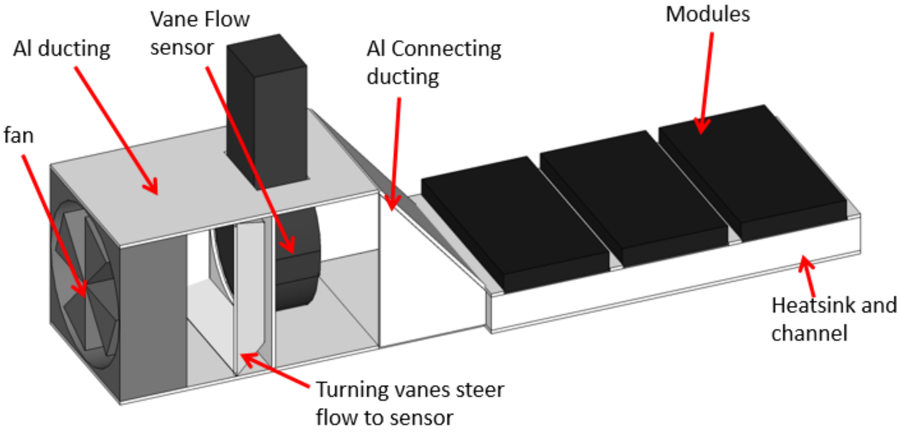

Figure 5.11. Design of air-force cooling system.

5.7.2 Experimental Setup

The second experiment layout is shown in Figure 5.12(a). The physical assembly of this configuration is shown in Figure 5.12(b)-(d). This configuration includes three power modules. The module being monitored is mounted in the final positon on the heatsink (with respect to the airflow direction). The three power modules are driven to generate a three-phase AC output current into a three-phase resistive inductive (RL) load with a frequency of 200Hz.

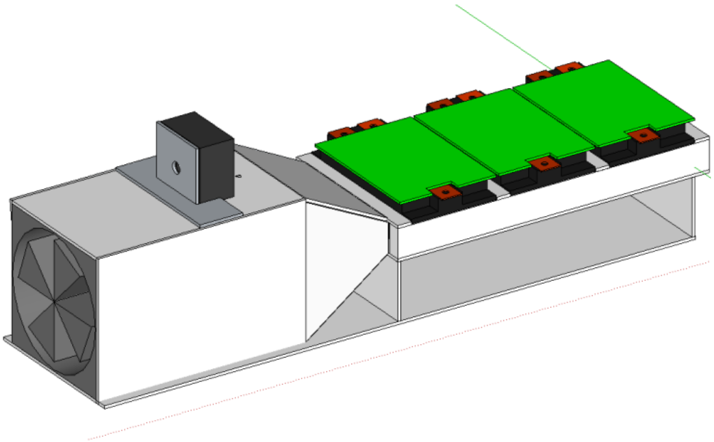

(a) Diagram of Channel/ducting final layout in experiment;

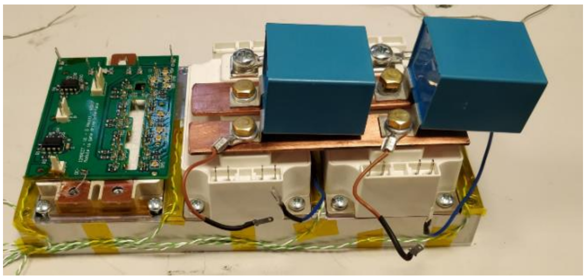

(b) Mounting of modules on heatsink

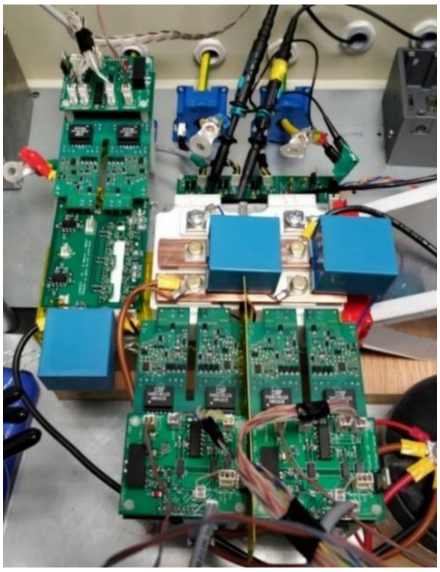

(c) Interface PCBs and wiring

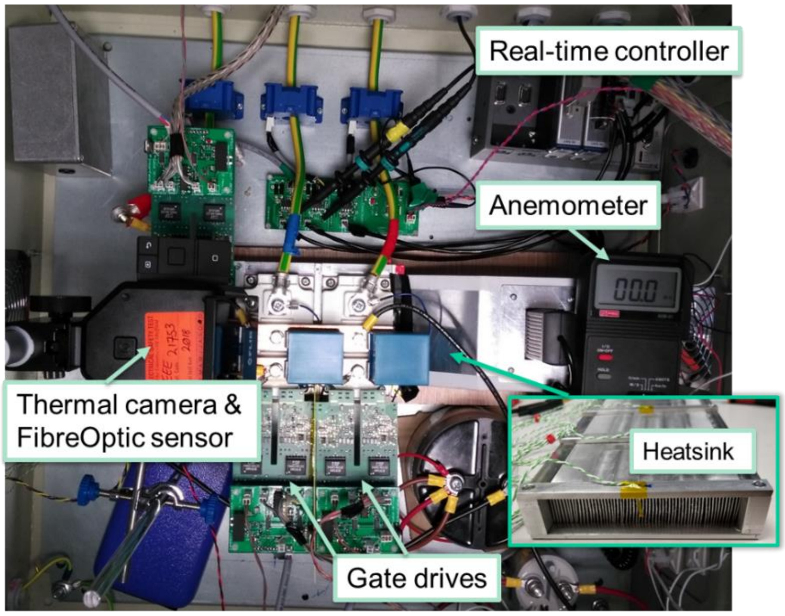

(d) Full experimental test rig with three phase inverter

Figure 5.12. Experimental setup.

Thermocouples installed positioned in airflow at inlet, outlet and between modules, as is shown in Figure 5.13.

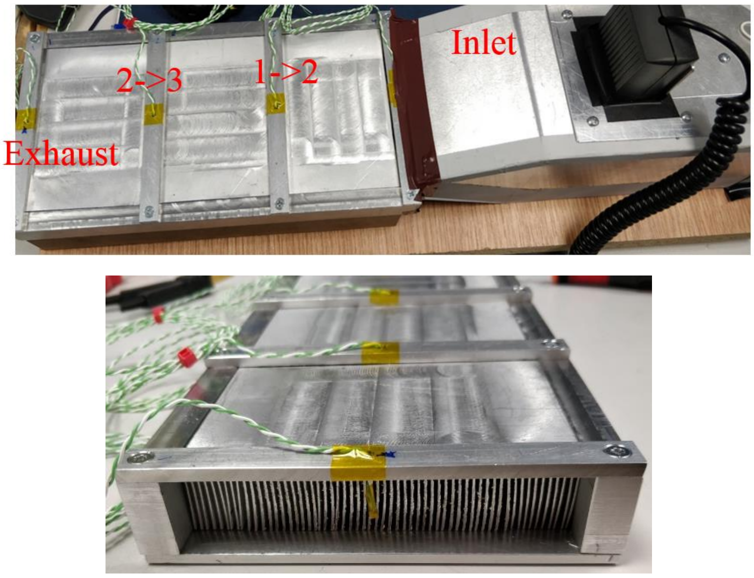

Figure 5.13 Schematic of the inverter

The anemometer used in the experiment is the AVM-01 digital USB anemometer. A clearer schematic of the inverter is shown in the Figure 5.14. It can be seen in Figure 5.14 that the anemometer is mounted in the inlet duct before feeding the heatsink.

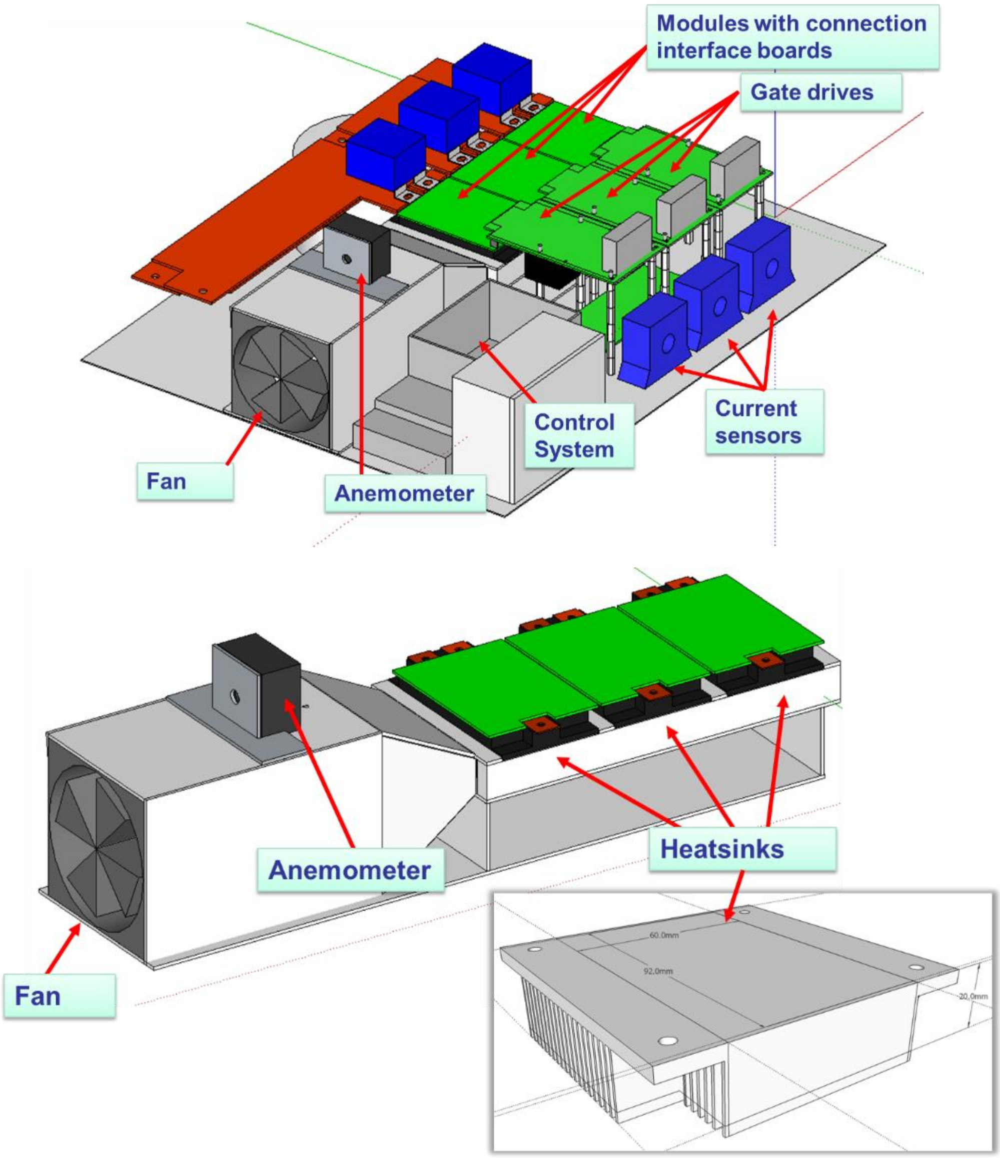

Figure 5.14 A clearer schematic of the inverter

5.7.3 Experimental Data and Simulation Results

The data from the numerical model and experiment (shown in Figure 5.15) were compared to test the behaviour of the disturbance estimation observer. The experiment was repeated for a range of different peak current ranging from 50A to 90A, allowing the model to be evaluated for a range of different power losses. The input power losses in the numerical model is set to 0 to avoid the disturbance caused by power loss estimation error.

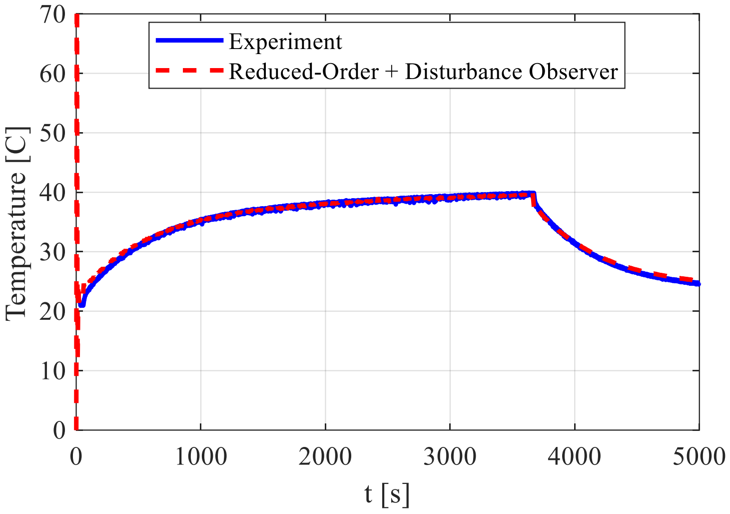

(a) 50A Peak Current

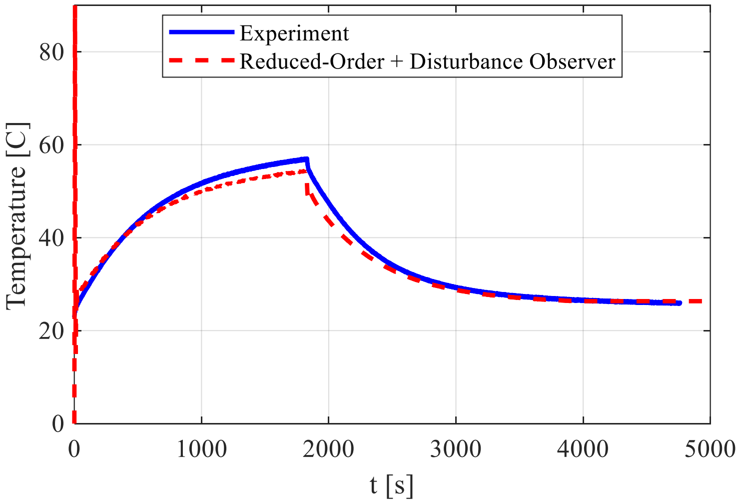

(b) 70A Peak Current

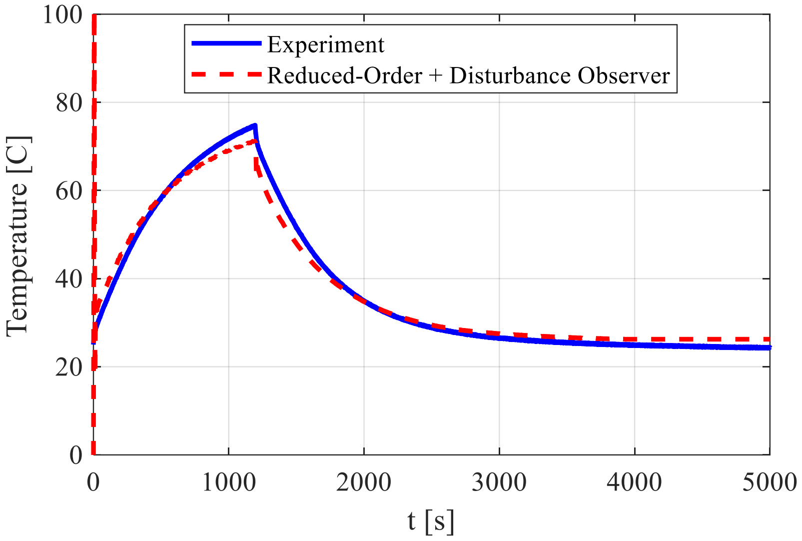

(c) 90A Peak Current

Figure 5.15. Comparison with Experimental Module

It can be seen in Figure 5.15 that the transient thermal response of the observer model with disturbance estimation can match the experimental data both on heating step and cooling step, if ambient temperature is available.

It is worth noting that despite the fact that the model placement and channel layout differ from those in the first experiment, both of the numerical models are supplied with the same set of parameters from the parameter estimation in Section 3.4 and Section 5.6. From this, it can be concluded that the parameters related to the module geometry are of substantial importance, whereas parameters pertaining to the converter layout have only a negligible effect on the model. This knowledge can be used to reduce the amount of calculation required when determining these parameters considerably.

5.8 Conclusion

In this Chapter, a reduced order observer model with disturbance estimation is presented. The parameters used in the state-space matrices are obtained from a transient CFD model and details can be seen in Chapter 3.

By considering different experimental configurations it is demonstrated that these changes have relatively little impact on the parameters if the geometry of the power module remains the same. Therefore, once the power module design is fixed, changes to the number of modules and their relative layout do not influence the parameter estimation results, reducing the calculation load.

The inclusion of a disturbance observer in this model is important as it allows the model to adjust for errors caused by errors in the power losses estimation and inaccuracy in parameters estimation and uncertainties in the environmental and operating conditions. It is also worth noting that the air temperature is a much simpler value to measure than the power dissipation, making it a more suitable input for the disturbance observer. The resulting model is shown to exhibit good accuracy and tracking capability, even under complex transient conditions, showing good correlation with the results obtained from a range of experimental tests. The method is computationally simple and therefore suitable for real-time application in industrial applications.

Chapter 6 Conclusion and Future Works

6.1 Conclusion

In this thesis, geometry-based numerical thermal models and compact thermal models are developed to address the fast thermal simulation in the electronic design process and real-time temperature monitoring of power electronics system, respectively. In analysis of thermal model, a range of design variables and operating conditions, such as inlet air temperature, velocity of the air flow, material composition of the power modules, and the geometry of the assembly, have be considered. Extensive experimental results are presented to validate the proposed concepts.

6.1.1 Geometry-Based Thermal Modelling and Parametric Model Order Reduction

The developed model order reduction techniques provide a valuable methodology for the analysis of complex and large-scale systems. The methodology illustrated in the thesis can be easily generalised to more complex and/or larger systems, confirming its application for accurate system-level integrated power electronic design. Typically, the dimension of a thermal problem discretized with finite difference can be extremely large, therefore rendering it intractable for large scale system if a fine discretization is required. Additionally, optimization of layout in power electronics modules and converters design might require many iterations using different values of parameters e.g. of materials or cooling conditions. In this case, the proposed multi-parameter MOR will provide a tool for parametric analyses to support optimised design.

With the proposed parametric MOR such applications can be greatly simplified as the reduced order model conserves dependency on parameters which can be simply modified at each iteration without requiring additional computations. The laboratory scale demonstration presented in the thesis includes all the feature and modelling complexities of typical air cooled three-phase converters systems and therefore provides an industrially relevant example of application. Compared with conventional FE tool like ANSYS

Mechanical, the numerical model based on multi-parameter order reduction has good data agreement with real-time experiment. Additionally, the obtained the numerical MOR model can be applied in transient temperature estimation with time-varying input as and boundary condition such as transient air flow rate, which is generally infeasible via conventional FE tool like ANSYS Mechanical.

6.1.2 Observer-Based Compact Thermal Model and Dynamic Disturbance Estimation

Geometry-based reduced-order numerical model can be applied in transient junction temperature estimation of power MOSFETs in the design of power module. In real-time operation, junction temperature monitoring of power MOSFETs fast computational speed and smaller compact models are needed. In this case, compact or reduced-order electro-thermal model based on RC networks may be fast and sufficiently accurate. In this work, third and first order networks are used to represent the vertical heat transfer between the power devices and the ambient, respectively. The order of the networks is a compromise between the ability to model multiple time constants (the higher the order of the network, the more time constants can be modelled) and simplicity of implementation in a real-time monitoring system.

Unfortunately, the modelling dynamic performances might be affected by both errors in the input values and uncertainties in the parameters of the state-space system. Uncertainties due to unknown coolant flow rate, parameters and power losses might also be difficult to address. The inclusion of an additional feedback mechanism in the observer, the disturbance estimation, provides a method to compensate for uncertainties in parameters and/or boundary conditions. Novel feedback mechanism of the disturbance observer provides a feedback mechanism to compensate the effects of all the errors combined instead of an accurate separation of the multiple sources of errors.

This additional feedback mechanism, implemented in a reduced-order observer, uses the temperature measurement of the inlet air and of a thermistor mounted on the power module substrate. It is also worth noting that the air temperature is a much simpler value to measure than the power dissipation, making it a more suitable input for the disturbance observer.

The reduced-order observer model with disturbance estimation techniques is also validated against real-time experiment. Due to the demanding accurate estimation of power electronic device with high switching frequency, additional validation again real-time experiment with three-phase inverter is introduced. Excellent data agreement between reduced-order observer models and real-time experiment under high switching frequency confirms the accuracy and implement in the application of power modules.

6.2 Future Work

In the thesis, geometry-based numerical thermal models and compact thermal models are developed to support optimised thermal design of power devices and real-time temperature monitoring of power electronics system, respectively. The geometry-based numerical thermal modelling, multi-parametric model order reduction, compact thermal modelling with observer and disturbance estimation are obtained in this thesis and validated against experiments with different operating conditions. Further research to improve the modelling and computational speed, as well as extend the applicability of the methods to different practical cases.

6.2.1 Improvements on the Geometry-Based Thermal Modelling

In this work the geometry definition of power modules, necessary for the definition of the system of equations based on the finite difference method, is hand-coded using MATLAB codes. The generation of the mesh requires thousands of line of MATLAB codes for each model, resulting in a tedious setup task. Nevertheless, this process could be easily automated to generate the full-order geometry. It is recommended that future work is dedicated to the development of simple and intuitive tools for inputting the geometry definition which can automatically generate the required discretized system of equations.

6.2.2 Further work on Multi-Parameter Model Order Reduction

In the proposed geometry-based thermal modelling, module power loss (on the top boundary) and properties of the air-force cooling system (on the bottom boundary) are the two sets of input considered. The bottom convective boundary condition has been modelled via the convective thermal modelling of local heat transfer coefficients, and the obtained coefficients can be fitted into reduced order mesh-based FD model as a set of deserved parameters. Similar concepts can be applied to other cooling conditions e.g. when liquid or phase-changing cooling is considered. It is recommended to further develop these model in future work.

In addition to the convective heat transfer coefficients, the proposed multi-parametric MOR technique can be applied to other parameters of interest in the design of power converters. Geometrical parameters, e.g. the length and width of baseplate and/or property parameters, e.g. the thermal conductivities of TIMs or sinter materials, can also be included in the improved multi-paramedic thermal models to address the fast thermal simulation in the electronic design process.

6.2.3 Further work on Observer and Parameter Estimation

The dynamic performances of the proposed estimators might be affected by nonlinearities in the parameters of the state-space system. In this work, the feedback mechanism of the disturbance observer provides a feedback mechanism to compensate the effects of all the errors combined instead of an accurate separation of the multiple sources of errors.

To increases the robustness of observer-based adaptive control, reconstruction of state vectors and estimation of nonlinear parameters can, in principle, be achieved via adaptive observers. If additional measurements are available, it could be possible to estimate unknown non-linear parameters using on- or off-line nonlinear optimization approaches.

6.2.4 Improvement of Power Loss Disturbance Estimation

It should be noted that even with the improved disturbance observer-based electro-thermal model, the uncertainties in module power losses is still one of the most critical factors affecting the accuracy of junction temperature estimation, especially in the monitoring of real-time operation.

In Chapter 5, inlet air temperature and measured sensor temperature are used to compensate the disturbance of power loss estimation. However, the measurement of air temperature is often not possible in some practical applications It is recommended to use data-fusion algorithms to combine the outcome of the real-time observer with more accurate models of losses based e.g. on detailed electro-thermal models of the power electronic switches.

Reference

[1] H. Wang, M. Liserre, and F. Blaabjerg, “Toward reliable power electronics: Challenges, design tools, and opportunities,” *IEEE Ind. Electron. Mag*., vol. 7, no. 2, pp. 17–26, 2013.

[2] A. Testa, S. De Caro, and S. Russo, “A Reliability Model for Power MOSFETs Working in Avalanche Mode Based on an Experimental Temperature Distribution Analysis,” *IEEE Trans. Power Electron.*, vol. 27, no. 6, pp. 3093–3100, 2012.

[3] S. Yang, A. Bryant, P. Mawby, D. Xiang, L. Ran, and P. Tavner, “An industry-based survey of reliability in power electronic converters,” IEEE Trans. Ind. Appl., vol. 47, no. 3, pp. 1441–1451, 2011.

[4] A. T. Bryant, P. A. Mawby, P. R. Palmer, E. Santi, and J. L. Hudgins, “Exploration of Power Device Reliability using Compact Device Models and Fast Electro-Thermal Simulation,” *Conf. Rec. 2006 IEEE Ind. Appl. Conf. Forty-First IAS Annu. Meet.*, vol. 3, no. c, pp. 1465–1472, 2006.

[5] H. Wang, K. Ma, and F. Blaabjerg, “Design for reliability of power electronic systems,” *IECON 2012 - 38th Annu. Conf. IEEE Ind. Electron. Soc*., pp. 33–44, 2012.

[6] M. Musallam, C. M. Johnson, C. Yin, H. Lu, and C. Bailey, “In-service life consumption estimation in power modules,” *2008 13th Int. Power Electron. Motion Control Conf. EPE-PEMC 2008*, pp. 76–83, 2008.

[7] Z. Gao, C. Cecati and S. X. Ding, "A Survey of Fault Diagnosis and Fault-Tolerant Techniques—Part I: Fault Diagnosis With Model-Based and Signal-Based Approaches," *in IEEE Transactions on Industrial Electronics*, vol. 62, no. 6, pp. 3757-3767, June 2015. doi: 10.1109/TIE.2015.2417501.

[8] H. Wang, M. Liserre, F. Blaabjerg, P. de Place Rimmen, J. B. Jacobsen, T. Kvisgaard, and J. Landkildehus, “Transitioning to physics-of-failure as a reliability driver in power electronics,” *IEEE J. Emerg. Sel. Topics Power Electron*. vol. 2, no. 1, pp. 97–114, Mar. 2014.

[9] N. Shammas, “Present problems of power module packaging technology,” *Microelectron. Rel*., vol. 43, no. 4, pp. 519–527, 2003.

[10] M. Ciappa, “Selected failure mechanisms of modern power modules,” *Microelectron. Reliab.*, vol. 42, pp. 653–667, 2002.

[11] Y. Song and B. Wang, “Survey on reliability of power electronic systems,” *IEEE Trans. Power Electron*., vol. 28, no. 1, pp. 591–604, Jan. 2013.

[12] R. Amro, J. Lutz and A. Lindemann, "Power cycling with high temperature swing of discrete components based on different technologies," in Power Electronics Specialists Conference, 2004. PESC 04. 2004 IEEE 35th Annual, pp. 2593-2598 Vol.4, 2004.

[13] A. Hamidi, S. Kaufmann, and E. Herr, “Increased lifetime of wire bonding connections for IGBT power modules,” in *Proc. APEC*, Mar. 4–8, vol. 2, pp. 1040–1044, 2001.

[14] Marz. M., "Thermal management in high-density power converters" Industrial Technology, 2003 IEEE International Conference on, vol.2, no., pp.1196,1201 Vol.2, 10-12 Dec. 2003.

[15] M. Gerber, J. A. Ferreira, N. Seliger, and I. W. Hofsajer, “Integral 3-D thermal, electrical and mechanical design of an automotive DC/DC converter,” *IEEE Trans. Power Electron*., vol. 20, no. 3, pp. 566–575, 2005.

[16] S. Yang, A. Bryant, P. Mawby, D. Xiang, L. Ran, and P. Tavner, “An industry-based survey of reliability in power electronic converters,” *IEEE Trans. Ind. Appl*., vol. 47, no. 3, pp. 1441–1451, 2011.

[17] W. Lai et al., “Experimental investigation on the effects of narrow junction temperature cycles on die-attach solder layer in an IGBT module,” *IEEE Trans. Power Electron*., vol. 32, no. 2, pp. 1431–1441, Feb. 2017.

[18] M. Held, P. Jacob, G. Nicoletti, P. Scacco, and M.-H. Poech, “Fast power cycling test of IGBT modules in traction application,” in *Proc. Int. Conf. Power Electron. Drive Syst*., 1997, vol. 1, pp. 425–430.

[19] M. Ciappa and W. Fichtner, “Lifetime prediction of IGBT modules for traction applications,” in *Proc. IEEE 38th Annu. Int. Rel. Phys. Symp*., 2000, pp. 210–216

[20] U. M. Choi, S. Jrgensen, and F. Blaabjerg, “Advanced accelerated power cycling test for reliability investigation of power device modules,” *IEEE Trans. Power Electron*., vol. 31, no. 12, pp. 8371–8386, Dec. 2016

[21] M. Thoben, “Tutorial—reliability and lifetime of power modules,” in *Proc. Eur. Conf. Power Electron. Appl*., 2016.

[22] M. Musallam, C. Buttay, M. Whitehead, C. M. Johnson, and C. Buttay, “Real-Time Compact Electronic Thermal Modelling for Health Monitoring”, *12th European Conference on Power Electronics and Applications*, 2007.

[23] J. N. Davidson, D. A. Stone, M. P. Foster and D. T. Gladwin, "Real-Time Temperature Estimation in a Multiple Device Power Electronics System Subject to Dynamic Cooling," in *IEEE Transactions on Power2 Electronics*, vol. 31, no. 4, pp. 2709-2719, April 2016. doi: 10.1109/TPEL.2015.2443034.

[24] PJ Tannous, SRT Peddada, JT Allison, T Foulkes, RCN Pilawa-Podgurski, Andrew G Alleyne, “Model-based temperature estimation of power electronics systems”, *Control Engineering Practice* 85, 206-215, April 2019.

[25] M. Iachello et al., "Lumped Parameter Modeling for Thermal Characterization of High-Power Modules," in IEEE Transactions on Components, Packaging and Manufacturing Technology, vol. 4, no. 10, pp. 1613-1623, Oct. 2014. doi: 10.1109/TCPMT.2014.2353695.

[26] V. Smet, F. Forest, J. J. Huselstein, F. Richardeau, Z. Khatir, S. Lefebvre, and M. Berkani, “Ageing and failure modes of IGBT modules in hightemperature power cycling,” *IEEE Trans. Ind. Electron*., vol. 58, no. 10, pp. 4931–4941, Oct. 2011.

[27] J. Biela et al, "Impact of Power Density Maximization on Efficiency of DC–DC Converter Systems," *IEEE Trans. Power Electron*, vol. 24, no. 1, pp. 288-300, Jan. 2009.

[28] Y. Lei et al., "A 2-kW Single-Phase Seven-Level Flying Capacitor Multilevel Inverter With an Active Energy Buffer," *IEEE Trans. Power Electron*, vol. 32, no. 11, pp. 8570-8581, Nov. 2017.

[29] M. A. Eleffendi and C. M. Johnson, “Application of Kalman Filter to Estimate Junction Temperature in IGBT Power Modules,” *IEEE Trans. Power Electron*, vol. 31, no. 2, pp. 1576–1587, 2016.

[30] T. K. Gachovska, T. Bo, J. Hudgins, Q. Wei, and J. Donlon, “A real-time thermal model for monitoring of power semiconductor devices,” in *Proc. IEEE Energy Convers. Congr. Expo, Sep*. 15–19, 2013, pp. 2208–2213.

[31] B. J. Nel and S. Perinpanayagam, “A brief overview of SiC MOSFET failure modes and design reliability,” *Procedia CIRP, vol. 59, no. TESConf*, pp. 280–285, 2017.

[32] G. Majumdar, T. Oomori, “Some key researches on SiC device technologies and their predicted advantages,” Proceedings of Power Conversion Intelligent Motion Conference, *PCIM Europe 2009*, pp. 328-333, Nuremberg, May 12-14, 2009.

[33] A. Wintrich, U. Nicolai, W. Tursky, and T. Reimann, “Application manual Power Semiconductors,” in *SEMIKRON International GmbH, Nuremberg, Germany*, 2011, pp. 127-129.

[34] A. Masson, W. Sabbah, R. Riva, C. Buttay, S. Azzopardi, H. Morel, et al., "Die attach using silver sintering. Practical implementation and analysis," *European Journal of Electrical Engineering*, vol. 16, pp. 293-305, 2013.

[35] M. Schaal, M. Klingler, und B. Wunderle, “Silver Sintering in Power Electronics: The State of the Art in Material Characterization and Reliability Testing“, gehalten auf der 7th Electronics System-Integration Technology Conference, ESTC, Dresden, Germany, 2018.

[36] E. Caroll, Power Electronics for Very High Power Applications. London, U.K.: ABB, 1998.

[37] A. B. Lostetter, F. Barlow, and E. Elshabini, “An Overview to Integrated Power Module Design for High Power Electronics Packaging”, *Microelectronics Reliability*, vol. 40, no. 3, pp. 365–379, 2000.

[38] C. Chen, F. Luo, and Y. Kang, “A review of SiC power module packaging: Layout, material system and integration,” *CPSS Trans. Power Electron. Appl.*, vol. 2, no. 3, pp. 170–186, Sep. 2017.

[39] R. Khazaka, L. Mendizabal, D. Henry, and R. Hanna, “Survey of high-temperature reliability of power electronics packaging components,” *IEEE Transactions on Power Electronics*, vol. 30, no. 5, pp. 2456-2464, 2015.

[40] Wang, H., Liserre, M., Blaabjerg, F., de Place Rimmen, P., Jacobsen, J. B., Kvisgaard, T., & Landkildehus, J. “Transitioning to Physics-of-Failure as a Reliability Driver in Power Electronics”. *IEEE Journal of Emerging and Selected Topics in Power Electronics*, 2(1), 97–114, 2014.

[41] Y. Luo, F. Xiao, B. Wang, and B. Liu, “Failure Analysis of Power Electronic Devices and Their Applications under Extreme Conditions,” Chinese J. Electr. Eng., vol. 2, no. 1, pp. 91–100, 2016.

[42] M. Ishiko, “Design concept for wire-bonding reliability improvement by optimizing position in power devices,” *Microelectron. J.* vol. 37, pp. 262-268, 2006.

[43] V. Smet, F. Forest, J. Huselstein, F. Richardeau, Z. Khatir, S. Lefebvre, and M. Berkani, “Ageing and failure modes of IGBT modules in hightemperature power cycling,” IEEE Trans. Ind. Electron., vol. 58, no. 10, pp. 4931–4941, Oct. 2011.

[44] Power, I. E. T, Reliability of Power Electronic Converter Systems. 2016.

[45] Infineon; Using the NTC inside a power electronic module; application note v1.0, Nov. 2009

[46] https://www.solidsolutions.co.uk

[47] J. P. Holman, “Heat Transfer”, 2010.

[48] K. Harding, “Heat transfer introduction”, 2018

[49] https://www.nuclear-power.net

[50] F. Casanellas, “Losses in PWM inverters using IGBTs”, *IEEE Proc. Electric Power Appl.*, vol. 141, n.5, pp. 235-239, Sep. 1994.

[51] T. Kamel, A. Griffo, J. Wang, “Modelling framework for parallel SiC power MOSFETs chips in modules developed by planar technology”, *IEEE Int. Conf. on Electrical Systems for Aircraft, Railway, Ship Propulsion and Road Vehicles & International Transportation Electrification Conference* (ESARS-ITEC), Nov. 2018.

[52] A. Wintrich, U. Nicolai, W. Tursky, and T. Reimann, Application Manual Power Semiconductors. Nuremberg, Germany: SEMIKRON International GmbH, 2011.

[53] Cannon, John Rozier, “The One–Dimensional Heat Equation, Encyclopaedia of Mathematics and Its Applications”, Cambridge University Press, pp. 483, 1984.

[54] H. Wang, M. Liserre, and F. Blaabjerg, “Toward reliable power electronics: Challenges, design tools, and opportunities,” *IEEE Ind. Electron. Mag.*, vol. 7, no. 2, pp. 17–26, 2013.

[55] Murthy, K., and Bedford, R.E.: ‘Transformation between Foster and Cauer equivalent networks’, *IEEE Trans. Circuits Syst.*, 1978, 25, (4), pp. 238–239

[56] D. A. Stone, J. N. Davidson, and M. P. Foster, “Required Cauer network order for modelling of thermal transfer impedance,” *Electron. Lett.*, vol. 50, no. 4, pp. 260–262, 2014.

[57] C.H. van der Broeck, R.D. Lorenz, and R.W. De Doncker, “Monitoring 3-D Temperature Distributions and Device Losses in Power Electronic Modules,” *IEEE Trans. Power Electron.*, (to appear) 2018.

[58] A. A. Joneidi, D. D. Ganji, and M. Babaelahi, “Differential Transformation Method to determine fin efficiency of convective straight fins with temperature dependent thermal conductivity,” *Int. Commun. Heat Mass Transf.*, vol. 36, no. 7, pp. 757–762, 2009.

[59] P. Constantin, A. J. Majda, and E. Tabak, “Formation of strong fronts in the 2-D quasigeostrophic thermal active scalar,” *Nonlinearity*, vol. 7, no. 6, pp. 1495–1533, 1994.

[60] N. Shamsundar and E. M. Sparrow, “Analysis of Multidimensional Conduction Phase Change Via the Enthalpy Model,” *J. Heat Transfer*, vol. 97, no. 3, pp. 333, 2010.

[61] H. Sen Peng and C. L. Chen, “Hybrid differential transformation and finite difference method to annular fin with temperature-dependent thermal conductivity,” *Int. J. Heat Mass Transf.*, vol. 54, no. 11–12, pp. 2427–2433, 2011.

[62] K. S. Ong, “A finite-difference method to evaluate the thermal performance of a solar water heater,” *Sol. Energy*, vol. 16, no. 3–4, pp. 137–147, 1974.

[63] https://www.machinedesign.com

[64] Tai-Ran Hsu, “Chapter 2 Finite Element Analysis in Heat Conduction Analysis of Solid Structures”.

[65] A. C. Antoulas and D. C. Sorensen, “Approximation of large-scale dynamical systems: An overview,” vol. 1892, pp. 1–22, 2001.

[66] Wang, W., & Yuan, X. (2016). "Lumped-parameter-based thermal analysis for virtual prototyping of power electronics systems". *8th IET International Conference on Power Electronics, Machines and Drives (PEMD 2016)*. doi:10.1049/cp.2016.0244.

[67] Y. J. Yang and C. C. Yu, “Extraction of heat-transfer macromodels for MEMS devices,” *J. Micromech. Microeng.*, vol. 14, no. 4, pp. 587–596, 2004.

[68] A. C. Cangellaris, S. Pasha, J. L. Prince and M. Celik, "A new discrete transmission line model for passive model order reduction and macromodeling of high-speed interconnections," in *IEEE Transactions on Advanced Packaging*, vol. 22, no. 3, pp. 356-364, doi: 10.1109/6040.784485, Aug. 1999

[69] A. Davoudi, P. L. Chapman, J. Jatskevich and H. Behjati, "Reduced-Order Dynamic Modeling of Multiple-Winding Power Electronic Magnetic Components," in *IEEE*

Transactions on Power Electronics, vol. 27, no. 5, pp. 2220-2226, doi: 10.1109/TPEL.2011.2179317, May 2012

[70] P. Benner, M. Hinze, and E. ter Maten, eds., "Model Reduction for Circuit Simulation", Lecture Notes in Electrical Engrg. 74, Springer-Verlag, Dordrecht, the Netherlands, 2011

[71] Pillage, L.T. and Rohrer, R.A. "Asymptotic waveform evaluation for timing analysis". *IEEE Trans. Computer-Aided Des*. 9, 352–366 ,1990.

[72] J. S. Fitch, A. K. Henning, E. B. Arkilic, J. M. Harris, “Pressure- based mass-flow control using thermopneumatically-actuated microvalves”, *Proc. Hilton Head*, pp. 162-165, (1998)

[73] Bechtold T, “ Model order reduction of electro-thermal MEMS”, PhD Thesis University of Freiburg, Germany, 2005

[74] Wil Schilders, “Introduction to Model Order Reduction”, NXP, Faculty of Mathematics and Computer Science,Enthovan.

[75] B. Lohmann, “Ordnungsreduktion und dominanzanalyse nichtlinearer Systeme”, Reiehe 8: Meß-, steuerungs- und Regelungstechnik Nr. 406, VDI Verlag, 1994.

[76] B. C. Moore, “Principal Component Analysis in Linear Systems: Controlability, Observability, and Model Reduction”, *IEEE Transactions on Automation and Control*, 26, pp. 17-32, 1981.

[77] G. Obinata, B. D. O. Anderson, “Model Reduction for Control System Design”, Springer, 2004.

[78] B. N. Datta, “Numerical Methods for Linear Control systems“, Elsevier Incorporation, 2004.

[79] V. Mehrmann and T. Stykel, “Balanced truncation model reduction for large-scale systems in descriptor form,” in Dimension Reduction of Large-Scale Systems, ser. Lecture Notes in Computational Science and Engineering, P. Benner, V. Mehrmann, and D. Sorensen, Eds. Berlin, Germany: Springer-Verlag, vol. 45, ch. 3, pp. 89–116, 2005.

[80] J.-R. Li, “Model Reduction of Large Linear systems via Low Rank System Gramians”, PhD. Thesis, Massachusetts Institute of Technology, 2000.

[81] J.R. Phillips, L. Daniel, and L.M. Silveira. Guaranteed passive balancing transformations for model order reduction. *Proc. 39th cConf. Design Automation*, 52-57, 2002.

[82] J.R. Phillips and L.M. Silveira. Poor Man's TBR: A simple model reduction scheme. *IEEE. Trans. Comp. Aided Design ICS*, 24(1):43-55, January 2005.

[83] A. C. Antoulas, "Approximation of linear dynamical systems", *Wiley Encyclopedia of Electrical and Electronics Engineering*, 11, pp. 403-422, (1999).

[84] A. Varga, "Model reduction software in the SLICOT library", In: *Applied and Computational Control, Signals and Circuits*, Ed. B. Datta, Kluwer Academic Publishers, (2001).

[85] G. A. Baker Jr., P. Graves-Morris, "Padé Approximants", Cambridge University Press, (1996)

[86] E. Chiproud, M. S. Nakhla, "Asymptotic Waveform Evaluation", Kluwer Academic Publishers, (1994).

[87] R. W. Freund, "Reduced-Order Modeling Techniques Based on Krylov subspaces and Their Use in Circuit Simulation", *Numerical analysis Manuscript*, 98-3-02, (1998).

[88] Z. Bai, "Krylov subspace techniques for reduced order modeling of largescale dynamical systems", *Applied Numerical Mathematics*, 43, pp. 9-44, (2002).

[89] R. W. Freund, M. H. Gutknecht, N. M. Nachtigal, "An implementation of the look-ahead Lanczos algorithm for non-Hermitian matrices", *SIAM Journal of Scientific Computing*, 15, pp. 313-337, (1994).

[90] R. W. Freund, "Krylov-subspace methods for reduced order modeling in circuit simulation", *Journal of Computational and Applied Mathematics*, 123(1-2), pp. 395-421, (2000).

[91] R. W. Freund, "Reduced-Order Modeling Techniques Based on Krylov subspaces and Their Use in Circuit Simulation", *Numerical analysis Manuscript*, 98-3-02, 1998

[92] R. W. Freund, "Krylov-subspace methods for reduced order modeling in circuit simulation", *Journal of Computational and Applied Mathematics*, 123(1-2), pp. 395-421, 2000.

[93] J. Cullum, T. Zhang, "Two-sided Arnoldi and Nonsymmetric Lanczos Algorithms", *SIAM Journal on Matrix Analysis and Applications*, 24(2), pp. 303-319, 2002.

[94] L. M. Silveira, M. Kamon, I. Elfadel, J. White,"A Coordinate-transformed Arnoldi Algorithm for Generating Guaranteed Stable Reduced-Order Models of RLC

Circuits", *Computational Methods of Applied Mechanical Engineering*, 169, pp. 377-389, 1999.

[95] R. J. Guyan, "Reduction of stiffness and mass matrices", AIAA Journal, 3(2), pp. 138, 1965).

[96] S.H. Chen, H.H. Pan, "Guyan reduction", Commun. Appl. Numer. Methods, 549–556, 1988.

[97] G. Floros, N. Evmorfopoulos and G. Stamoulis, "Efficient Hotspot Thermal Simulation Via Low-Rank Model Order Reduction," *2018 15th International Conference on Synthesis, Modeling, Analysis and Simulation Methods and Applications to Circuit Design (SMACD)*, Prague, 2018, pp. 205-208, doi: 10.1109/SMACD.2018.8434858.

[98] P. Feldmann and F. Liu, "Sparse and efficient reduced order modeling of linear subcircuits with large number of terminals", *Proc. Intl. Conference Computer-aided Design*, pp. 88–92, 2004.

[99] X. Wang, A. Castellazzi, and P. Zanchetta, "Full-order observer based IGBT temperature online estimation," *IECON Proc. Industrial Electron. Conf.*, pp. 1494–1498, 2014.

[100] X. Wang, A. Castellazzi, and P. Zanchetta, "Observer based dynamic adaptive cooling system for power modules," *Microelectron. Reliab.*, vol. 58, pp. 113–118, 2016.

[101] X. Wang, A. Castellazzi, and P. Zanchetta, "Temperature control for reduced thermal cycling of power devices," *15th Eur. Conf. Power Electron. Appl.*, pp. 1–10, 2013.

[102] M. Andresen, M. Schloh, G. Buticchi, and M. Liserre, "Computational light junction temperature estimator for active thermal control," in *Proc. IEEE Energy Convers. Congr. Expo*, pp. 1–7, 2016.

[103] Scott Moura, "Energy Systems and Control", University of California, Berkeley.

[104] Bemporad, A., State estimation and linear observers, in Lecture notes of Automatic Control I. Academic Year 2010-2011, University of Trento.

[105] S. Nazari, "A Review of the unknown input observer with examples", 2015.

[106] E. KIYAK and O.C. AYSE KAHVECIOGLU: Aircraft sensor fault detection based on unknown input observers. An Int. J. Aircraft Engineering and Aerospace Technology, 80(5), 545-548, 2008.

[107] Raff, T., Lachner, F., Allgöwer, F. “A finite time unknown input observer for linear systems”, Proc. 14th Mediterranean Conf. on Control and Automation, 28–30 June 2007.

[108] Chadli, M. and Karimi, H.R. “Robust observer design for unknown inputs Takagi-Sugeno models”. *IEEE Transactions on Fuzzy Systems*, 21(1), 158–164, 2013.

[109] D. Tan, R.J. Patton and X. Wang, “Relaxed solution to unknown input observers for state and fault estimation,” Proc. Pth IFAC Symposium on Fault Detection, Supervision and Safety of Technical Processes SAFEPROCESS 2015, Paris, France: IFACPapersOnLine vol. 48, no. 21, pp. 1048-1053, 2015.

[110] Zhang W., H. Su, H. Wang, and Z. Han. “Full-order and reduced-order observers for one-side nonlinear systems using Riccati equations”. *Commun. Nonlinear Sci. Numer. Simul.* **17**: 4968–4977, 2012.

[111] B. Friedland. “Reduced-order state observers”. In H. Unbehauen editor, *Control Systems, Robotics and Automation - Vol. VIII*, pages 26–36. Eoless Publishers Co. Ltd., Oxford, United Kingdom, 2009.

[112] Vinodh Kumar. E, Jovitha Jerome J and S. Auuappan, “Comparison of four state observer design algorithms for MIMO system”, Archives of Control Sciences Volume 23(LIX), 2013.

[113] J. Zhang, F. Zhu, “On the observer matching condition and unknown input observer design based on the system left-invertibility concept,” *Transactions of the Institute of Measurement and Control*, vol. 40, no. 9, pp. 2887-2900, Jun. 2018.

[114] J. Zhang, X. Zhao, F. Zhu, and H. Karimi, ‘‘Reduced-order observer design for switched descriptor systems with unknown inputs,’’ *IEEE Trans. Autom. Control*, to be published. doi: 10.1109/TAC.2019.2913050.

[115] U. Choi, S. Jørgensen, and F. Blaabjerg, “Impact of Cooling System Capacity on Lifetime of Power Module in Adjustable Speed Drives,” vol. 7, no. 3, pp. 1768–1776, 2019.

[116] P. Ning, G. Lei, F. Wang, and K. D. T. Ngo, “Selection of heatsink and fan for high-temperature power modules underweight constraint,” in *Proc. IEEE APEC*, Feb. 2008, pp. 192–198.

[117] C. Gammeter, F. Krismer, and J. W. Kolar, “Weight optimization of a cooling system composed of fan and extruded-fin heat sink,” *IEEE Trans. Ind. Appl.*, vol. 51, no. 1, pp. 509–520, Jan./Feb. 2015.

[118] U. Drofenik, J. W. Kolar, “Analysing the theoretical limits of forced air-cooling by employing advanced composite materials with thermal conductivities >400W/mK,” *Proc. of 4th Int. Conf. on Integrated Power Systems (CIPS'06)*, Naples (Italy), June 2006, pp. 323-328.

[119] R. J. Moffat, “Modeling air-cooled heat sinks as heat exchangers,” in *Proc. 23rd Annu. IEEE SEMI-THERM*, San Jose, CA, USA, pp. 200–207 , Mar. 18–22, 2007.

[120] Azar, K. and Tavassoli, B. “How Much Heat Can Be Extracted from a Heat Sink?” Electronics Cooling, May 2003.

[121] https://www.electronics-cooling.com/2006/02/a-simple-thermal-resistance-model-isoflux-versus-isothermal/

[122] Çengel, Yunus A. *Heat and Mass Transfer* (Second ed.). McGraw-Hill. p. 336, 2002.

[123] M. M. Denn, “Process Fluid Mechanics,” Prentice-Hall, Upper Saddle River, 1980.

[124] R. K. Shah, “A Correlation for Laminar Hydrodynamic Entry Length Solutions fir Circular and Noncircular Ducts,” J. Fluids Engng, vol. 100, no. June 1978, pp. 177–179, 2019.

[125] Shah, R. K., and London, A. L., *Laminar Flow Forced Convection in Ducts*, Academic Press, New York, NY, 1978

[126] White, F. M., Viscous Fluid Flow, McGraw-Hill, 1974.

[127] Y. S. Muzychka , and M. M. Yovanovich, “Pressure Drop in Developing Laminar Flow in Non-Circular Ducts: A Scaling and Modeling Approach”, *Journal of Fluids Engineering*, vol. 131, 9 pages, 2009

[128] M. M. Yovanovich, and Y. S. Muzychka, “Solutions of Poisson Equation within Singly and Doubly Connected Domains,” AIAA 97-3880, *1997 National Heat Transfer Conference,* August 10-12, 1997.

[129] M. M. Yovanovich and P. Teertstra, “Natural Convection Inside Vertical Isothermal Ducts of Constant Arbitrary CrossSection,” AIAA Paper 01-0368, presented at the 39th Aerospace Sciences Meeting and Exhibit, Reno, NV, January 8–11, 2001.

[130] Z. F. Dong and M. A. Ebadian, “Convective heat transfer in the entrance region of a rectangular duct with two indented sides,” *Computational mechanics*, pp. 269–278, 1991.

[131] W. Rohlfs and J. H. L. V, “Entrance length effects on Graetz number scaling in laminar duct flows with periodic obstructions : Transport number correlations for

spacer-filled membrane channel flows," *Journal of Membrane Science*, pp. 842–852, June 2016.

[132] Y. S. Muzychka and M. M. Yovanovich, "Laminar forced convection heat transfer in the combined entry region of non-circular ducts," *ASME Trans.*, vol. 126, no. 1, pp. 54–61, Feb. 2004.

[133] Y. S. Muzychka and M. M. Yovanovich, "Pressure Drop in Laminar Developing Flow in Noncircular Ducts: A Scaling and Modeling Approach," *J. Fluids Eng.*, vol. 131, no. 11, p. 111105, 2009.

[134] https://neutrium.net/fluid_flow/pressure-loss-in-pipe/

[135] Muzychka, Y. S., and Yovanovich, M. M., Laminar Flow Friction and Heat Transfer in Non-Circular Ducts and Channels - Part I Hydrodynamic Problem, in *Compact Heat Exchangers: A Festschrift on the 60th Birthday of Ramesh K. Shah*, Grenoble, France, August 24, 2002, Eds. G.P. Celata, B. Thonon, A. Bontemps, and S. Kandlikar, pp. 123–130.

[136] Shah, R. K., and Bhatti, M. S., Chapter 3: Laminar Convective Heat Transfer in Ducts, in *Handbook of Single Phase Convective Heat Transfer*, eds. S. Kakac, R.K. Shah, and W. Aung, Wiley, New York, NY, 1987.

[137] Muzychka, Y. S., and Yovanovich, M. M., Laminar Forced Convection Heat Transfer in Combined Entrance Region of Non-Circular Ducts, *Journal of Heat Transfer*, vol. 126, pp. 54–61, 2004.

[138] M. Guacci, D. Bortis, I.F. Kovacevic-Badstuner, U. Grossner, J.W. Kolar, "Analysis and Design of a 1200 V All-SiC Planar Interconnection Power Module for Next Generation More Electrical Aircraft Power Electronic Building Blocks", *CPSS Trans. On Power Electronics and Appl.* Vol. 2, n.4, pp. 320-330, Dec. 2017.

[139] K. Weidner, M. Kaspar, and N. Seliger, "Planar interconnect technology for power module system integration," in *Proc. of the 7th International Conference on Integrated Power Electronic Systems (CIPS)*, Nuremberg, Germany, 2012.

[140] www.i2mpect.eu

[141] www.opsens-solutions.com

List of Figures

List of Figures

List of Tables